

# ***Modeling of the Boiling Water Reactor Dry Cask Simulator***

**Spent Fuel and Waste Disposition**

***Prepared for  
U.S. Department of Energy  
Spent Fuel and Waste Science and  
Technology***

***SR Suffield  
DJ Richmond  
JA Fort***

***May, 2019  
PNNL-28424***

**DISCLAIMER**

This information was prepared as an account of work sponsored by an agency of the U.S. Government. Neither the U.S. Government nor any agency thereof, nor any of their employees, makes any warranty, expressed or implied, or assumes any legal liability or responsibility for the accuracy, completeness, or usefulness, of any information, apparatus, product, or process disclosed, or represents that its use would not infringe privately owned rights. References herein to any specific commercial product, process, or service by trade name, trade mark, manufacturer, or otherwise, does not necessarily constitute or imply its endorsement, recommendation, or favoring by the U.S. Government or any agency thereof. The views and opinions of authors expressed herein do not necessarily state or reflect those of the U.S. Government or any agency thereof.

## SUMMARY

Three different thermal analysis models were developed to simulate the dry cask simulator (DCS). The DCS is an experiment set up to simulate a single boiling water reactor (BWR) fuel assembly under a variety of heat loads and internal pressures. The models included a detailed STAR-CCM+ model with the fuel assembly and flow straightener geometry explicitly modeled, a porous STAR-CCM+ model with the fuel assembly and flow straightener geometry modeled as porous media regions with calculated effective properties, and a COBRA-SFS model. The models were run for a combination of low and high canister pressures (100 kPa and 800 kPa) and low and high internal heat loads (0.5 kW and 5 kW). Results from all three models were compared against experimental data taken from the DCS for the peak cladding temperature (PCT) and inlet air mass flow.

Overall the measured PCT is in good agreement between the three models, with the detailed STAR-CCM+ and COBRA-SFS models providing the best comparison with the measured data. The STAR-CCM+ porous model predicted higher PCT values than the measured data for all four pressure heat load combinations, indicating that the effective thermal conductivity ( $k_{\text{eff}}$ ) approach to modeling a fuel assembly provides conservative PCTs. Using a split  $k_{\text{eff}}$  approach for the BWR fuel assembly was also shown to produce the best agreement with the measured PCT data for the porous model. The split  $k_{\text{eff}}$  approach calculated two different  $k_{\text{eff}}$  correlations for the full and partial array sections.

The PCT is in good agreement between the detailed STAR-CCM+ and the COBRA-SFS models, except for the high pressure and high heat load case (800 kPa and 5 kW). The COBRA-SFS cladding temperature profile is flat in comparison with STAR-CCM+ models, most likely due to differences in how the partial length rods and channel box emissivity are modeled in the COBRA-SFS model. At the time of this report no profile data was available for the measured DCS data, only the PCT and the elevation at which PCT occurred. Comparing the elevation at which the PCT occurred shows that the STAR-CCM+ model elevations occur at similar locations to the measured data, especially the detailed model. The COBRA-SFS model with the flatter profile varied significantly from the measured data for the low-pressure cases (100 kPa).

The COBRA-SFS model had a higher predicted air mass flow rate in comparison with the STAR-CCM+ models for the low heat load cases (0.5 kW) and predicted a slightly lower air mass flow rate for the high heat load cases (5 kW).

All three models were able to produce reasonable PCT estimates, with the porous media model with the  $k_{\text{eff}}$  fuel assembly providing the most conservative PCT estimates. The meshing study with STAR-CCM+ porous media model showed that a larger model with a full cask/fuel assembly could be constructed at a computationally efficient element size with the porous media model.

The authors recommend making code changes to COBRA-SFS to better suit BWR modeling. Historically the code was developed before BWR assemblies routinely included part-length rods and applied primarily to PWR assemblies because they are the most thermally limiting in safety analysis. To provide an easily applicable toolset for high fidelity BWR modeling the code should be changed to include better part-length rod and fuel channel modeling tools.

This page is intentionally left blank.

## **ACKNOWLEDGEMENTS**

This work was conducted as part of the Department of Energy Spent Fuel and Waste Science and Technology campaign. The authors thank Ned Larson of the Department of Energy and Sylvia Saltzstein of Sandia National Laboratories (SNL) for the support and leadership in this research program.

The authors would like to thank Sam Durbin and Eric Lindgren of SNL for the discussions about their experiment. The visit to the test facility was also very helpful and we appreciate the information sharing and hospitality provided by all the SNL staff that were involved.

The authors would like to express their appreciation to PNNL Scientific and Technical Communications staff, Colleen Winters and Susan Tackett, for their help in producing a clear presentation of our results. We also thank Dave Rector for his careful review of this report and constructive comments.

This page is intentionally left blank.

## CONTENTS

SUMMARY .....	iii
ACKNOWLEDGEMENTS .....	v
ACRONYMS .....	xiii
1. INTRODUCTION .....	1
2. DETAILED MODELING WITH CFD .....	3
2.1 Experimental Configuration .....	3
2.1.1 Geometry and Materials .....	3
2.1.2 Test Conditions .....	8
2.1.3 Assumptions .....	8
2.2 Meshing .....	9
2.3 Results .....	14
2.3.1 100 kPa, 0.5 kW .....	14
2.3.2 100 kPa, 5 kW .....	17
2.3.3 800 kPa, 0.5 kW .....	20
2.3.4 800 kPa, 5 kW .....	23
3. POROUS MEDIA MODELING WITH CFD .....	27
3.1 Effective Thermal Conductivity .....	27
3.1.1 Axial $k_{\text{eff}}$ Model .....	27
3.1.2 Radial $k_{\text{eff}}$ Models .....	27
3.2 Porous Flow Loss Coefficients .....	34
3.3 Mesh Sensitivity .....	38
3.4 Results .....	41
3.4.1 100 kPa, 0.5 kW .....	41
3.4.2 100 kPa, 5 kW .....	43
3.4.3 800 kPa, 0.5 kW .....	45
3.4.4 800 kPa, 5 kW .....	47
3.5 Comparison with Detailed CFD .....	49
4. DETAILED MODELING WITH COBRA-SFS .....	55
4.1 Geometry Modeling .....	55
4.1.1 Treatment of Part-Length Rods and Water Rods .....	57
4.1.2 Treatment of Fuel Channel .....	58
4.2 Solid and Fluid Properties .....	58
4.2.1 Treatment of Variable Emissivity .....	58
4.3 Boundary Conditions .....	58
4.3.1 Heat Generation .....	58
4.3.2 Side and Top Boundaries .....	58
4.3.3 Air Inlet and Outlet .....	58
4.4 Results .....	59
4.5 COBRA-SFS Sensitivity Studies .....	61
4.5.1 Sensitivity to Channel Model .....	61

---

4.5.2	Sensitivity to Channel Emissivity .....	63
5.	COMPARISON OF STAR-CCM+ AND COBRA-SFS RESULTS.....	65
5.1.1	100 kPa, 0.5 kW .....	66
5.1.2	100 kPa, 5 kW .....	68
5.1.3	800 kPa, 0.5 kW .....	69
5.1.4	800 kPa, 5 kW .....	70
6.	CONCLUSIONS AND RECOMMENDATIONS .....	71
7.	REFERENCES .....	73

## LIST OF FIGURES

Figure 2-1. CAD geometry of DCS – exterior view.....	4
Figure 2-2. CAD geometry of DCS – axial cross-sectional view.....	5
Figure 2-3. CAD geometry of DCS – radial cross-sectional view at 75 inches from the top of the bottom plate.....	6
Figure 2-4. Mesh for detailed full 360 model – external view.....	9
Figure 2-5. Mesh for detailed full 360 model – radial cross-sectional view at 75 inches from the top of the bottom plate.....	10
Figure 2-6. Mesh for detailed quarter model – external view.....	11
Figure 2-7. Mesh for detailed quarter model – radial cross-sectional view at 75 inches from top of the bottom tie plate.....	12
Figure 2-8. Component temperature profiles for 800 kPa canister pressure and 0.5 kW heat load .....	13
Figure 2-9. Component temperature profiles for 800 kPa canister pressure and 5 kW heat load .....	14
Figure 2-10. Thermocouple component temperatures for 100 kPa and 0.5 kW.....	15
Figure 2-11. Axial temperature contour plot through assembly midsection for 100 kPa and 0.5 kW.....	16
Figure 2-12. Radial temperature contour plot at the PCT elevation for 100 kPa and 0.5 kW.....	17
Figure 2-13. Thermocouple component temperatures for 100 kPa and 5 kW.....	18
Figure 2-14. Axial temperature contour plot through assembly midsection for 100 kPa and 5 kW.....	19
Figure 2-15. Radial temperature contour plot at the PCT elevation for 100 kPa and 5 kW.....	20
Figure 2-16. Thermocouple component temperatures for 800 kPa and 0.5 kW.....	21
Figure 2-17. Axial temperature contour plot through assembly midsection for 800 kPa and 0.5 kW.....	22
Figure 2-18. Radial temperature contour plot at the PCT elevation for 800 kPa and 0.5 kW.....	23
Figure 2-19. Thermocouple component temperatures for 800 kPa and 5 kW.....	24
Figure 2-20. Axial temperature contour plot through assembly midsection for 800 kPa and 5 kW.....	25
Figure 2-21. Radial temperature contour plot at the PCT elevation for 800 kPa and 5 kW.....	26
Figure 3-1. Radial $k_{eff}$ for DCS fuel assembly at 0.5 kW.....	28
Figure 3-2. Radial $k_{eff}$ for DCS fuel assembly at 5 kW.....	29
Figure 3-3. Sensitivity case for radial $k_{eff}$ for DCS fuel assembly at 5 kW.....	30
Figure 3-4. Comparison of PCT at 100 kPa and 0.5 kW.....	31
Figure 3-5. Comparison of PCT at 100 kPa and 5 kW.....	32
Figure 3-6. Comparison of PCT at 800 kPa and 0.5 kW.....	33
Figure 3-7. Comparison of PCT at 800 kPa and 5 kW.....	34
Figure 3-8. Flow straightener geometry for porous flow loss model.....	35
Figure 3-9. Fuel assembly geometry for porous flow loss model.....	36

Figure 3-10. Pressure drop vs. superficial velocity for flow straightener model. .... 37

Figure 3-11. Pressure drop vs. superficial velocity for fuel assembly model. .... 37

Figure 3-12. Initial mesh configuration – radial cross-sectional view of DSC assembly. .... 38

Figure 3-13. Refined mesh configuration – radial cross-sectional view of DSC assembly. .... 39

Figure 3-14. Very refined mesh configuration – radial cross-sectional view of DSC assembly. .... 39

Figure 3-15. Thermocouple component temperatures for 100 kPa and 0.5 kW. .... 42

Figure 3-16. Axial temperature contour plot through assembly midsection for 100 kPa and 0.5 kW. .... 42

Figure 3-17. Radial temperature contour plot at the PCT elevation for 100 kPa and 0.5 kW. .... 43

Figure 3-18. Thermocouple component temperatures for 100 kPa and 5 kW. .... 44

Figure 3-19. Axial temperature contour plot through assembly midsection for 100 kPa and 5 kW. .... 44

Figure 3-20. Radial temperature contour plot at the PCT elevation for 100 kPa and 5 kW. .... 45

Figure 3-21. Thermocouple component temperatures for 800 kPa and 0.5 kW. .... 46

Figure 3-22. Axial temperature contour plot through assembly midsection for 800 kPa and 0.5 kW. .... 46

Figure 3-23. Radial temperature contour plot at the PCT elevation for 800 kPa and 0.5 kW. .... 47

Figure 3-24. Thermocouple component temperatures for 800 kPa and 5 kW. .... 48

Figure 3-25. Axial temperature contour plot through assembly midsection for 800 kPa and 5 kW. .... 48

Figure 3-26. Radial temperature contour plot at the PCT elevation for 800 kPa and 5 kW. .... 49

Figure 3-27. Component TC temperature profiles for 100 kPa @ 0.5 kW. .... 50

Figure 3-28. Component TC temperature profiles for 100 kPa @ 5 kW. .... 51

Figure 3-29. Component TC temperature profiles for 800 kPa @ 0.5 kW. .... 52

Figure 3-30. Component TC temperature profiles for 800 kPa @ 5 kW. .... 53

Figure 3-31. Air mass flowrate comparison. .... 53

Figure 4-1. Cross-section of the COBRA-SFS model representation of the DCS. (Not to scale) .... 56

Figure 4-2. Rod and subchannel array diagram for COBRA-SFS model of the 9×9 BWR fuel assembly. (Not to scale) (Yellow represents water rods. Red represents part-length rods) .... 57

Figure 4-3. Temperature plot of peak rod for each case, Note: the active length extends from 10.9” to 154.7” .... 60

Figure 4-4. Assembly flow (channel flow vs. no channel flow). .... 62

Figure 4-5. Peak clad temperature comparison (channel flow vs. no channel flow). .... 63

Figure 4-6. Sensitivity to channel emissivity. .... 64

Figure 5-1. PCT comparison plot for 100 kPa and 0.5 kW. .... 66

Figure 5-2. Air mass flow comparison plot for 100 kPa and 0.5 kW. .... 67

Figure 5-3. PCT comparison plot for 100 kPa and 5 kW. .... 68

---

Figure 5-4. Air mass flow comparison plot for 100 kPa and 5 kW. ....	68
Figure 5-5. PCT comparison plot for 800 kPa and 0.5 kW.....	69
Figure 5-6. Air mass flow comparison plot for 800 kPa and 0.5 kW. ....	69
Figure 5-7. PCT comparison plot for 800 kPa and 5 kW.....	70
Figure 5-8. Air mass flow comparison Plot for 800 kPa and 5 kW.....	70

## LIST OF TABLES

Table 2-1. Heater rod effective properties. ....	7
Table 2-2. Helium properties. ....	7
Table 2-3. Air properties. ....	8
Table 2-4. Four corner test conditions. ....	8
Table 2-5. Natural convection correlations. ....	8
Table 2-6. Mesh summary. ....	12
Table 2-7. Peak component temperatures for 100 kPa and 0.5 kW. ....	14
Table 2-8. Air mass flow for 100 kPa and 0.5 kW. ....	15
Table 2-9. Peak component temperatures for 100 kPa and 5 kW. ....	17
Table 2-10. Air mass flow for 100 kPa and 5 kW. ....	17
Table 2-11. Peak component temperatures for 800 kPa and 0.5 kW. ....	20
Table 2-12. Air mass flow for 800 kPa and 0.5 kW. ....	20
Table 2-13. Peak component temperatures for 800 kPa and 5 kW. ....	23
Table 2-14. Air mass flow for 800 kPa and 5 kW. ....	23
Table 3-1. Axial $k_{eff}$ for fuel assembly. ....	27
Table 3-2. Calculated porous loss coefficients. ....	38
Table 3-3. Mesh details for mesh sensitivity study. ....	39
Table 3-4. Mesh sensitivity results @ 800 kPa and 5 kW. ....	40
Table 3-5. Grid convergence index. ....	41
Table 3-6. Peak component temperatures for 100 kPa and 0.5 kW. ....	41
Table 3-7. Air mass flow for 100 kPa and 0.5 kW. ....	41
Table 3-8. Peak component temperatures for 100 kPa and 5 kW. ....	43
Table 3-9. Air mass flow for 100 kPa and 5 kW. ....	43
Table 3-10. Peak component temperatures for 800 kPa and 0.5 kW. ....	45
Table 3-11. Air mass flow for 800 kPa and 0.5 kW. ....	45
Table 3-12. Peak component temperatures for 800 kPa and 5 kW. ....	47
Table 3-13. Air Mass Flow for 800 kPa and 5 kW. ....	47
Table 4-1. Ambient temperatures used as boundary conditions in COBRA-SFS model. ....	59
Table 4-2. Comparison of peak clad temperature measurements with results from COBRA-SFS. ....	59
Table 4-3. Comparison of experimental averages and COBRA-SFS predictions for air mass flow. ....	61
Table 4-4. Helium mass flow through COBRA-SFS model cross-sections. ....	61
Table 5-1. PCT comparison table. ....	65
Table 5-2. Helium mass flow comparison table. ....	65

## ACRONYMS

BWR	boiling water reactor
CAD	computer aided design
CFD	computational fluid dynamic
DCS	dry cask simulator
GCI	Grid Convergence Index
$k_{\text{eff}}$	effective thermal conductivity
MgO	magnesium oxide
NIST	National Institutes of Standard and Technology
PCT	peak cladding temperature
SNL	Sandia National Laboratories
TC	thermocouple

This page is intentionally left blank.

# MODELING OF THE BOILING WATER REACTOR DRY CASK SIMULATOR

## 1. INTRODUCTION

Thermal analysis codes are used to perform thermal qualification of radioactive material storage and transportation packages to regulatory requirements. To better understand the analytical modeling of a system's thermal performance a dry cask simulator (DCS) was set up to produce data sets for model validation of cladding temperatures and flow regimes associated with vertical dry cask storage systems. The DCS was set up to simulate a single boiling water reactor (BWR) fuel assembly under a variety of heat loads and internal pressures. The resulting data sets from the DCS were produced under well-controlled inputs and boundary conditions. Two different thermal analysis codes were used to simulate the DCS, the commercially available computational fluid dynamics (CFD) software STAR-CCM+ (Siemens PLM Software, 2018) and COBRA-SFS (Michener et al., 2017). For the STAR-CCM+ model, both a detail model with the fuel assembly modeled explicitly and a porous model with the fuel assembly modeled as a single porous region were constructed. All models were compared with the DCS data sets for peak cladding temperature (PCT) and inlet air mass flow rate. The details and results for all three models are given in the following sections.

This page is intentionally left blank.

## 2. DETAILED MODELING WITH CFD

A detailed CFD model of the DCS was constructed using the commercial software STAR-CCM+ (Siemens PLM Software, 2018). The detailed CFD model explicitly modeled the parts that make up the fuel region assembly, including the heater rods, water rods, fuel spacers, and tie plates. A detailed description of the model and resulting flow rate and temperatures is given in this section.

### 2.1 Experimental Configuration

The purpose of the DCS was to produce validation-quality data that can be used to test the validity of thermal qualification models used to determine PCT in vertical dry storage casks. The DCS is constructed of an electrically heated but otherwise prototypic BWR Incoloy-clad test assembly inside a storage basket and cylindrical pressure vessel that represents a vertical canister system. The canister is surrounded in a carbon steel shell assembly to represent a convection cooled aboveground dry cask system. The air mass flow rate at the inlets was measured for the aboveground configuration. The DCS was run at various canister pressures and heat loads. The pressure vessel canister was filled with helium gas and pressurized. The geometry and material property details of the DCS are described in the DCS handbook (Lindgren and Durbin, 2017).

#### 2.1.1 Geometry and Materials

The geometry for the detailed CFD model was generated using the commercial computer aided design (CAD) software SolidWorks (Dassault Systemes SolidWorks Corp., 2017). The CAD geometry was constructed from drawings and details listed in the DCS handbook (Lindgren and Durbin, 2017). All parts, except for the heater rods, were explicitly modeled including the flow straighteners and fuel assembly. The parts in the detailed fuel assembly included the full and partial length heater rods, the tie plates, water rods, and spacers. The heater rod is made up of Incoloy cladding, MgO and Nichrome elements, and carbon steel pins. Each heater rod is modeled as a single volume in the CAD geometry and effective material properties were calculated and applied to the heater rods.

The CAD geometry is shown in Figure 2-1 through Figure 2-3.

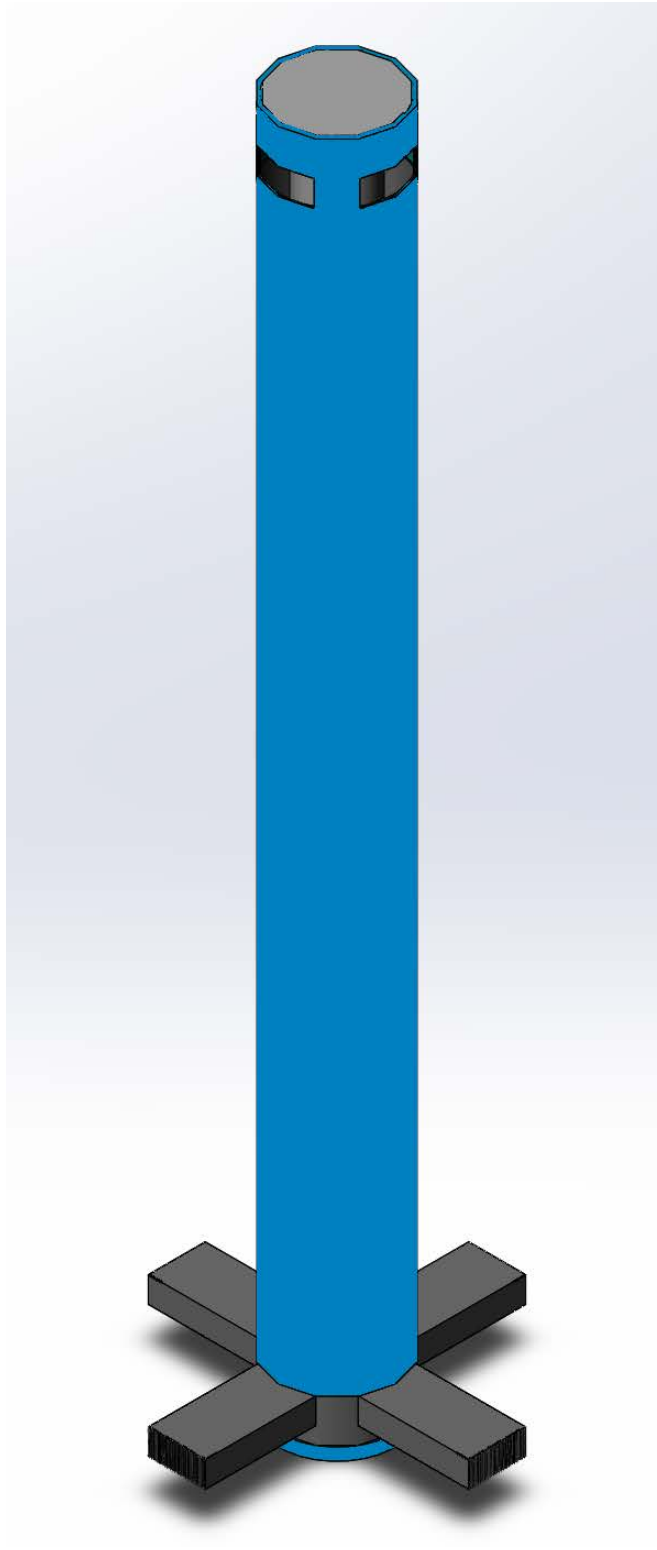
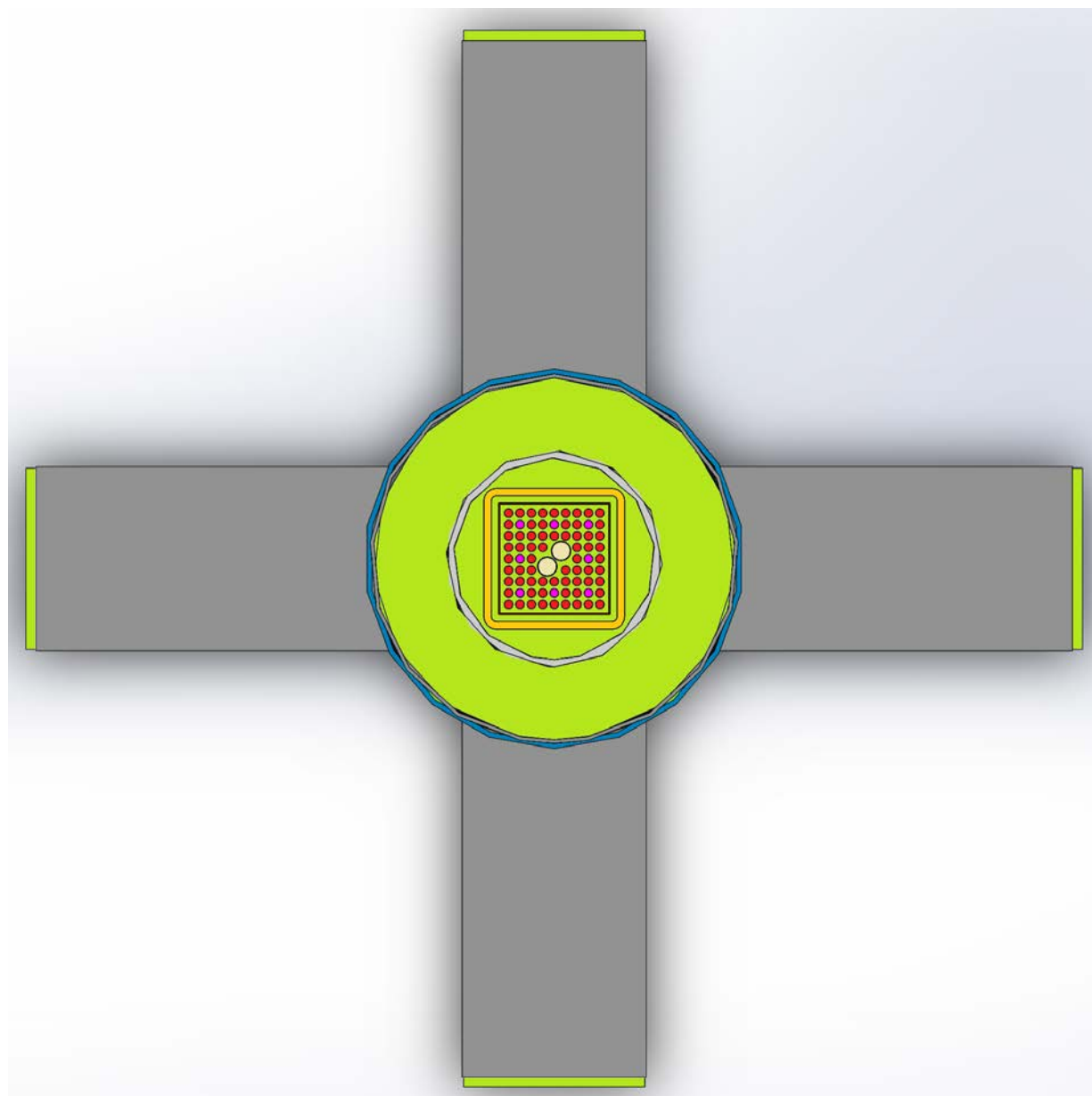


Figure 2-1. CAD geometry of DCS – exterior view.



Figure 2-2. CAD geometry of DCS – axial cross-sectional view.



**Figure 2-3. CAD geometry of DCS – radial cross-sectional view at 75 inches from the top of the bottom plate.**

The material properties for the solid parts in the model were taken from the DCS handbook (Lindgren and Durbin 2017). The effective properties for the heater rods were calculated based on volume weighted averaging of the Incoloy cladding and MgO. The Nichrome and carbon steel pins only represent a small percentage of the overall volume of the heater rod and were therefore neglected in the overall effective property calculation. The effective material properties for the heater rods are listed in Table 2-1. The properties for the air and helium gas was taken from textbook values (Incropera 2007).

Those values are listed in Table 2-2 and Table 2-3.

**Table 2-1. Heater rod effective properties.**

<b>Effective Heater Rod Properties</b>			
<b>Temperature</b>	<b>Density</b>	<b>Specific Heat</b>	<b>Thermal Conductivity</b>
<b>[K]</b>	<b>[kg/m<sup>3</sup>]</b>	<b>[J/kg-K]</b>	<b>[W/m-K]</b>
300	3926.15	754.99	4.149
450	3926.15	878.32	4.922
650	3926.15	942.37	5.771
850	3926.15	978.80	6.605
1050	3926.15	1006.14	7.402

**Table 2-2. Helium properties.**

<b>Helium</b>		
<b>Temperature</b>	<b>Thermal Conductivity</b>	<b>Viscosity</b>
<b>[K]</b>	<b>[W/m-K]</b>	<b>Pa-s</b>
100	0.0730	9.63E-06
120	0.0819	1.07E-05
140	0.0907	1.18E-05
160	0.0992	1.29E-05
180	0.1072	1.39E-05
200	0.1151	1.50E-05
220	0.1231	1.60E-05
240	0.1300	1.70E-05
260	0.1370	1.80E-05
280	0.1450	1.90E-05
300	0.1520	1.99E-05
350	0.1700	2.21E-05
400	0.1870	2.43E-05
450	0.2040	2.63E-05
500	0.2200	2.83E-05
600	0.2520	3.20E-05
650	0.2640	3.32E-05
700	0.2780	3.50E-05
750	0.2910	3.64E-05
800	0.3040	3.82E-05
900	0.3300	4.14E-05
1000	0.3540	4.46E-05

**Table 2-3. Air properties.**

Air	
Temperature	Thermal Conductivity
[K]	[W/m-K]
294.26	0.0251
310.93	0.0264
422.04	0.0339
533.15	0.0405
644.26	0.0469
755.37	0.0532

### 2.1.2 Test Conditions

The test conditions for the DCS are listed in the DCS test report (Durbin and Lindgren 2017). Numerous canister pressures and heat load combinations were run. From those runs four different test conditions were considered for the model presented in this report. The four test conditions are listed in Table 2-4 and represent the four corners of the canister pressure and heat load cases. The ambient temperature was assumed to be at 300 K for all four cases.

**Table 2-4. Four corner test conditions.**

Case	Canister Pressure [kPa]	Heat Load [kW]
1	100	0.5
2	100	5
3	800	0.5
4	800	5

### 2.1.3 Assumptions

The heat load was assumed to be uniform across the full and partial length heater rods. Internal radiation was included in the gas regions and the emissivity values applied along the inner surfaces were taken from the DCS handbook (Lindgren and Durbin 2017). External convection and radiation were applied along the vertical outer insulation and top horizontal surface of the shell assembly. The external convection coefficients were calculated based on the following natural convection coefficient correlations (Holman 1997) shown in Table 2-5:

**Table 2-5. Natural convection correlations.**

Surface	Laminar	Turbulent
	$10^4 < GrPr < 10^9$	$GrPr > 10^9$
Vertical plane or cylinder	$h = 1.42(\Delta T/L)^{1/4}$	$h = 1.31(\Delta T)^{1/3}$
Horizontal plate facing upward	$h = 1.32(\Delta T/L)^{1/4}$	$h = 1.52(\Delta T)^{1/3}$

A low Reynolds number turbulence flow model was applied to the air region where the flow is driven by natural convection. The inlets to the air region were set to stagnation inlets and a pressure outlet was applied to each outlet. Laminar flow was assumed in the helium gas region.

## 2.2 Meshing

The SolidWorks geometry was imported into STAR-CCM+. The geometry was then meshed into regions connected by interface boundaries, resulting in a single conformal polyhedral volume mesh across all regions. Along each wall/fluid interface, the mesh contains a prism cell layer to improve the accuracy of the flow solution near the walls. The prism cell layer consists of orthogonal prismatic cells adjacent to the wall boundaries. The prism cell layer in the air region was four cells thick and two cells thick in the helium region. The detailed CAD geometry was meshed into a full 360-degree model. This resulted in a very large mesh. For computational efficiency a quarter section model of the detailed geometry was also meshed. Symmetry boundaries were applied to the quarter model. Figure 2-4 through Figure 2-7 show the resulting meshes for the full 360 and quarter model.

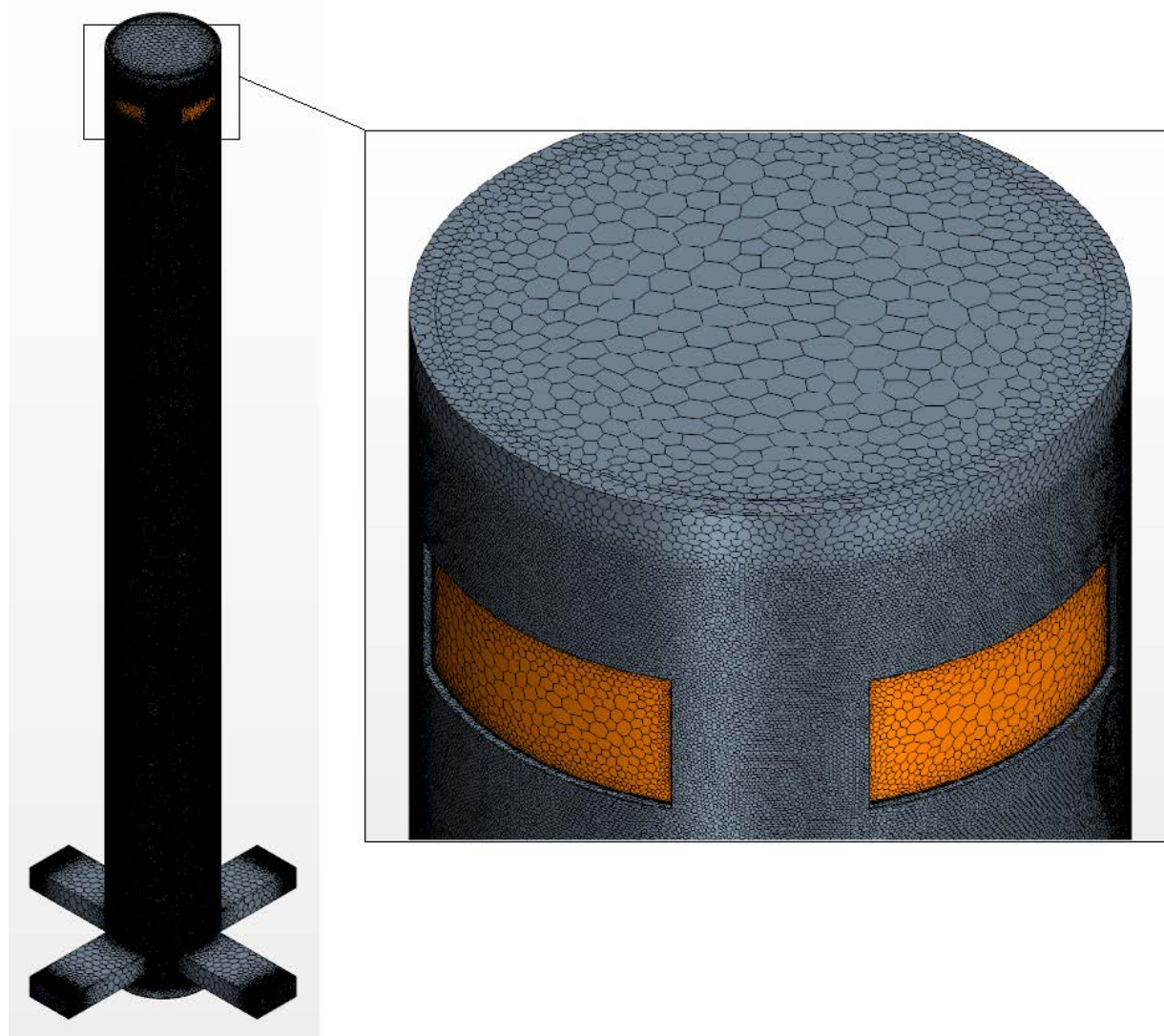
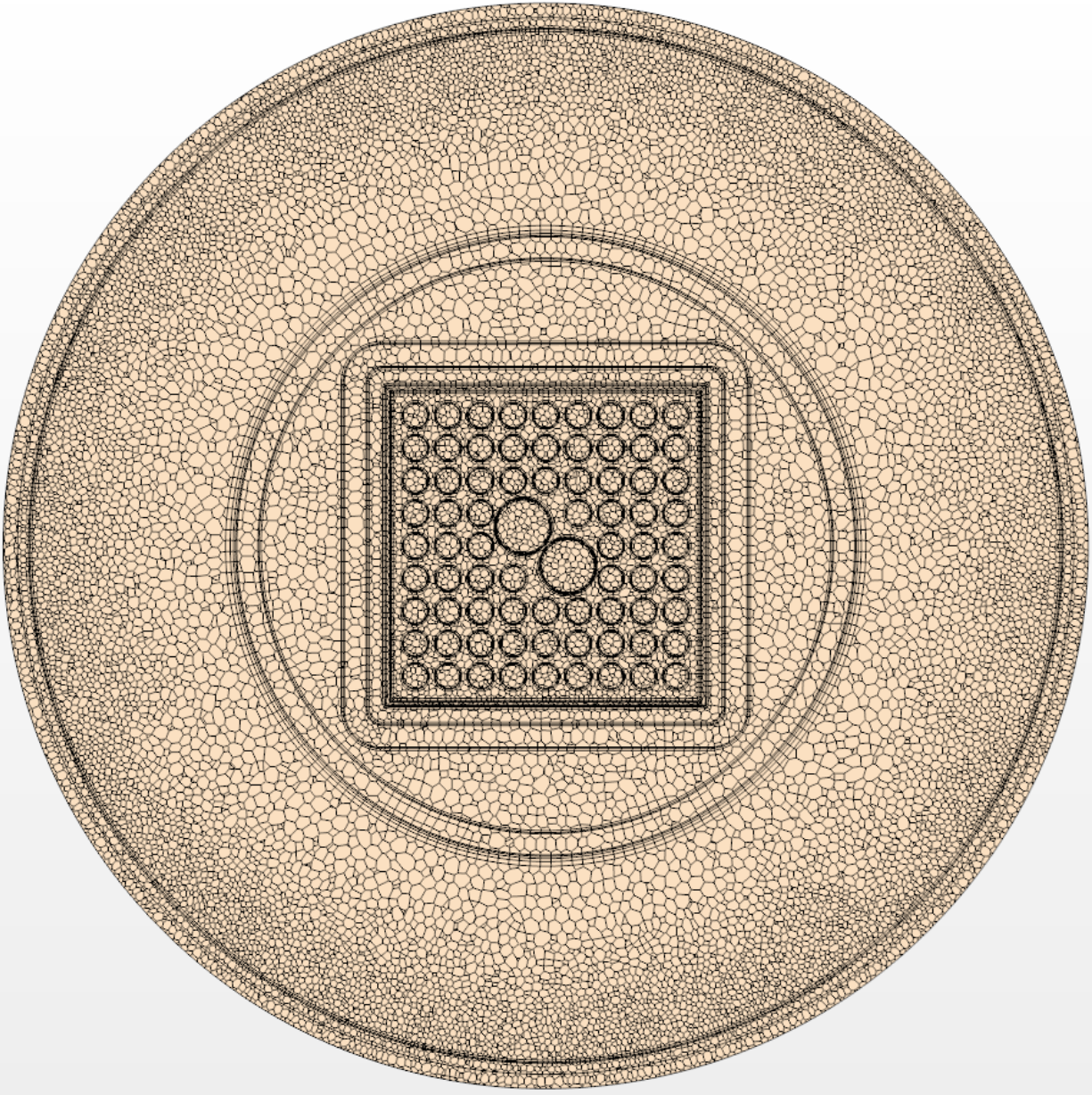


Figure 2-4. Mesh for detailed full 360 model – external view.



**Figure 2-5. Mesh for detailed full 360 model – radial cross-sectional view at 75 inches from the top of the bottom plate.**

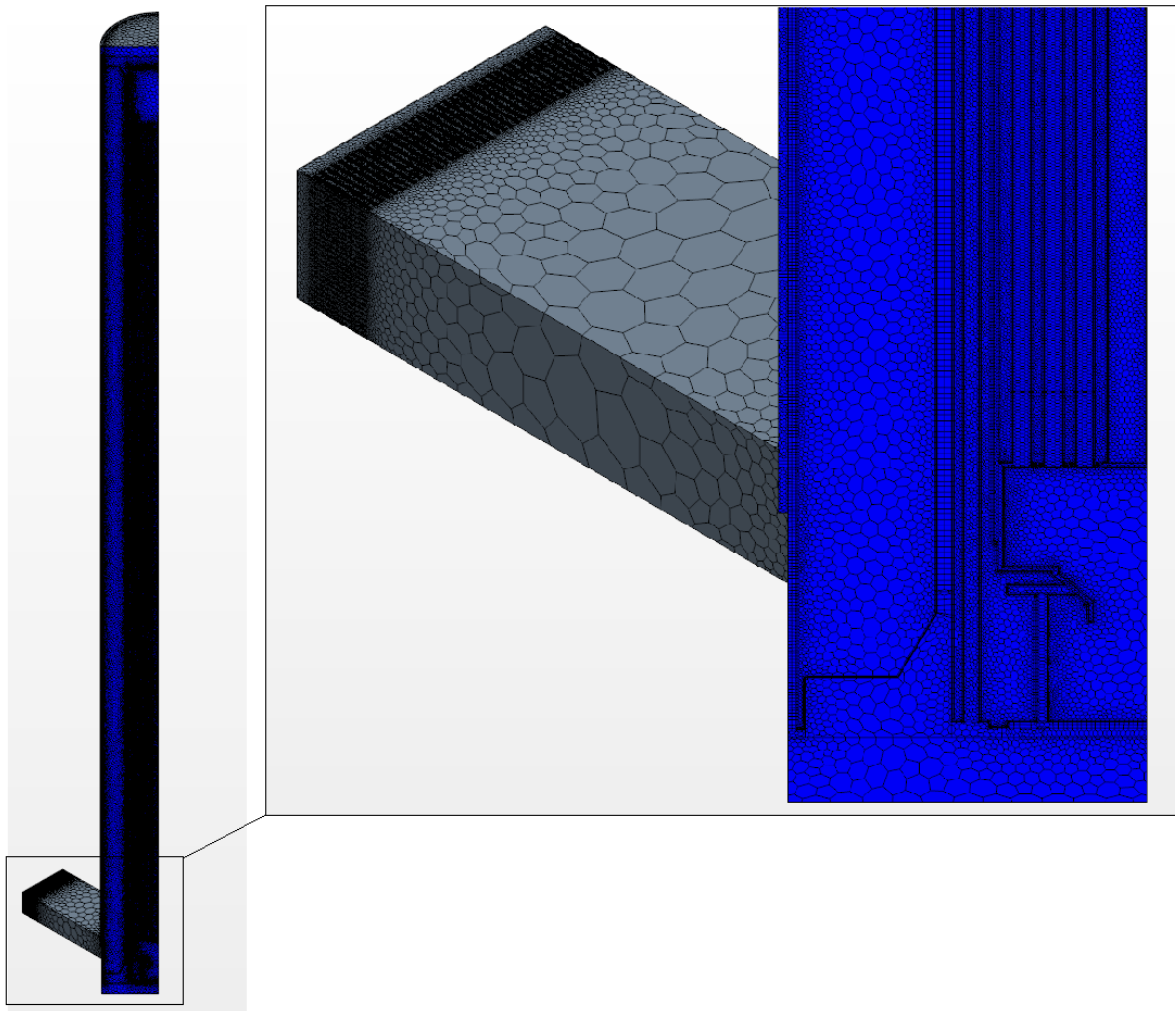
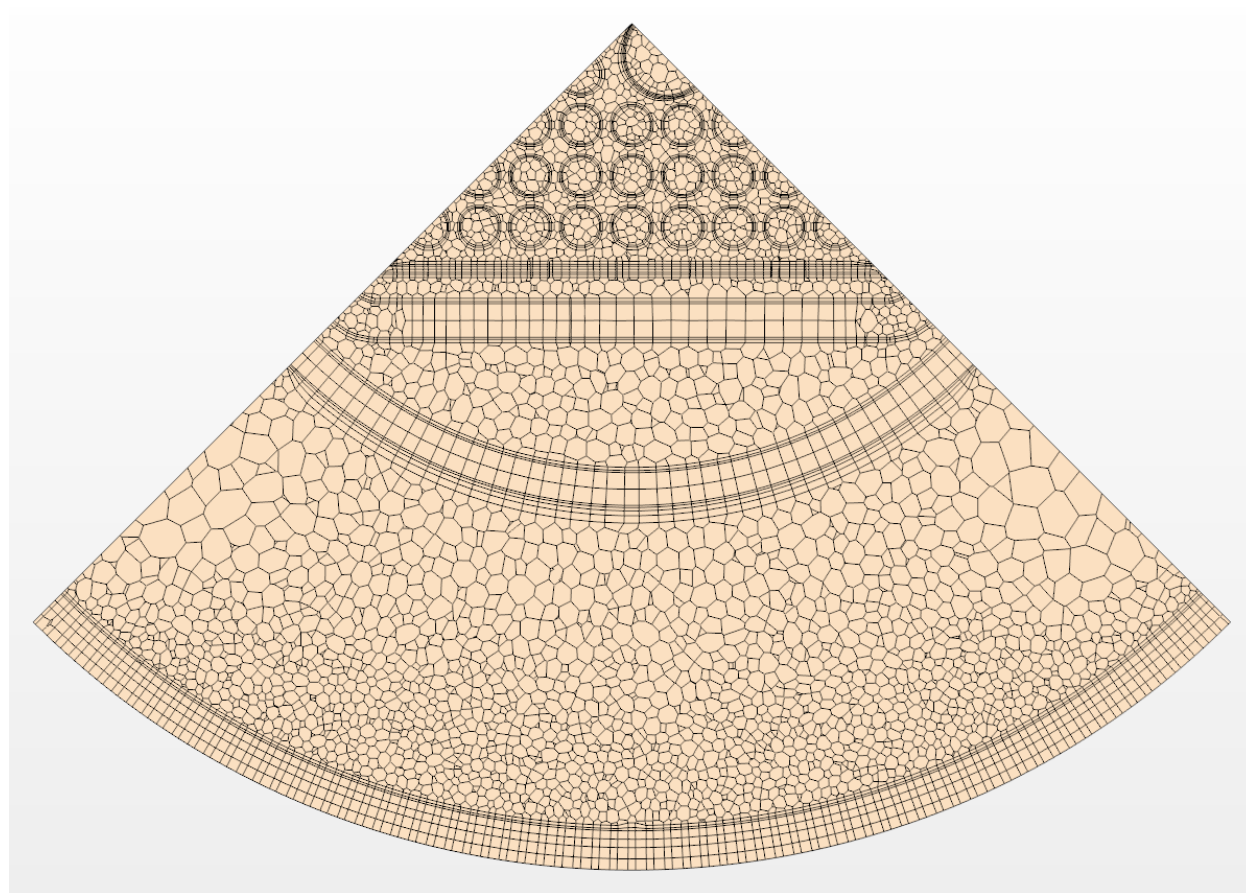


Figure 2-6. Mesh for detailed quarter model – external view.



**Figure 2-7. Mesh for detailed quarter model – radial cross-sectional view at 75 inches from top of the bottom tie plate.**

Both the full 360 and quarter model were run for the 800 kPa canister pressure cases to compare and ensure that the quarter model was comparable to the full 360 model. Table 2-6 compares the resulting mass flow of the air and PCT. The table also lists the total solver elapsed time and shows that the quarter model reduced the solver time by ~ 78%. Figure 2-8 and Figure 2-9 show component temperature profiles for the two models. Overall the quarter model behaves very similar to the full 360 model. For efficiency the quarter model was used exclusively for the rest of the study.

**Table 2-6. Mesh summary.**

Case	Cell Count	Total Solver Elapsed Time	Air Mass Flow	PCT
Full 360 Model @ 800 kPa and 0.5 kW	58481631	65.6 hrs	0.0206 kg/s	367
Quarter Model @ 800 kPa and 0.5 kW	12840684	13.6 hrs	0.0206 kg/s	367
Full 360 Model @ 800 kPa and 5 kW	58481631	63.5 hrs	0.0601 kg/s	654
Quarter Model @ 800 kPa and 5 kW	12840684	14.6 hrs	0.0601 kg/s	652

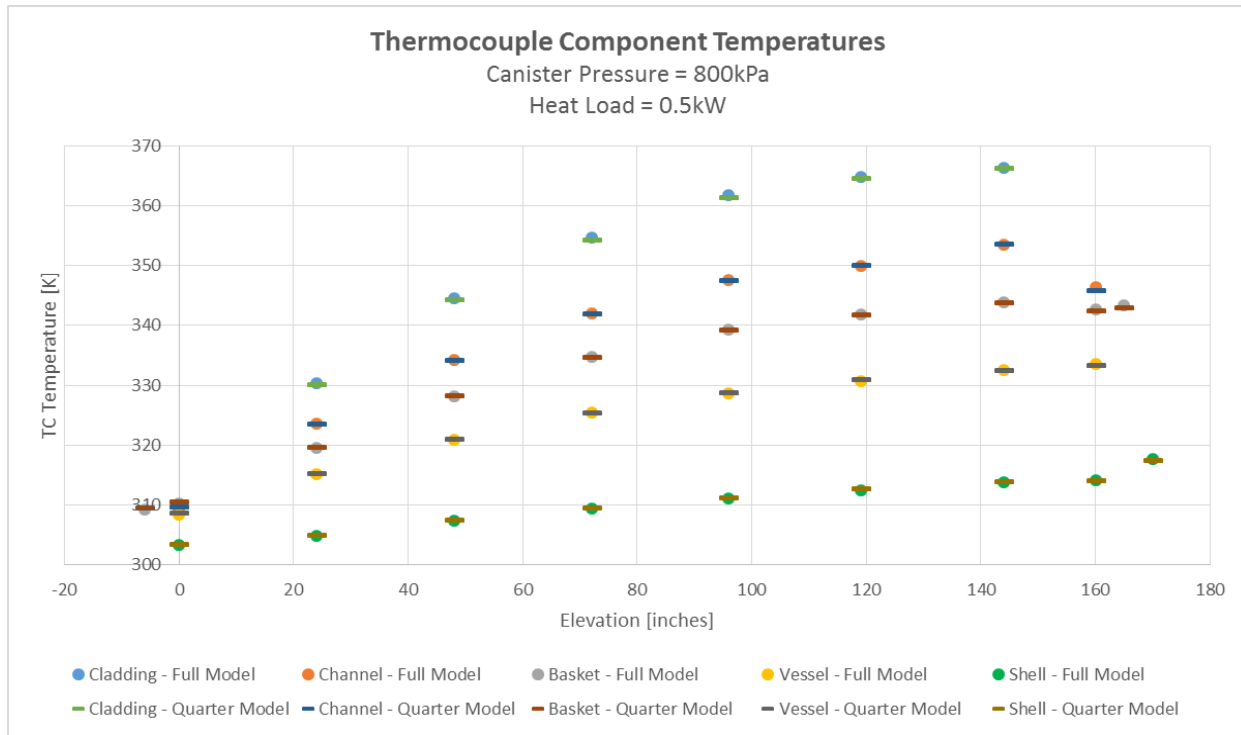


**Figure 2-8. Component temperature profiles for 800 kPa canister pressure and 0.5 kW heat load (0 elevation is located at the top of the bottom plate).**

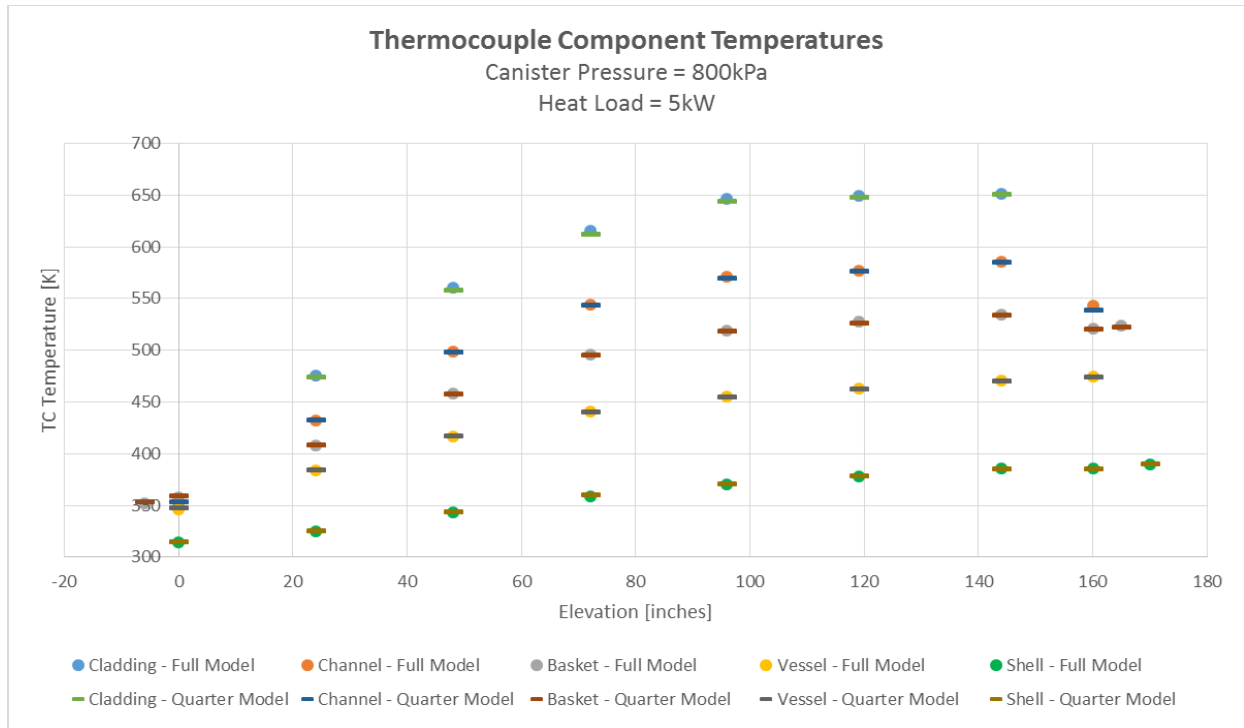


**Figure 2-9. Component temperature profiles for 800 kPa canister pressure and 5 kW heat load (0 elevation is located at the top of the bottom plate).**

### 2.3 Results

The DCS was instrumented with thermocouples (TCs) for temperature measurements, pressure transducers to monitor the internal vessel pressure, and hot wire anemometers for flow velocity (Lindgren 2017). The flow velocity measurements were taken just downstream of the flow straighteners near the inlets. Temperature measurements from the model were taken at the approximate TC locations. For the cladding temperatures the peak was taken across the entire cross-section of elevation corresponding to a TC location. The starting elevation (elevation = 0) was at the top of the bottom tie plate. Results for the four corner cases are shown in the following sections in Table 2-7 through Table 2-14 and Figure 2-10 through Figure 2-21.

#### 2.3.1 100 kPa, 0.5 kW

**Table 2-7. Peak component temperatures for 100 kPa and 0.5 kW.**

Component	Max Temperatures [K]		
	Predicted	Measured	delta
Cladding	380	376	4
Channel	362	359	3
Basket	349	344	5
Vessel	334	328	6
Shell	314	312	2

**Table 2-8. Air mass flow for 100 kPa and 0.5 kW.**

Air Mass Flow Rate[kg/s]	
Predicted	Measured
0.0241	0.0264

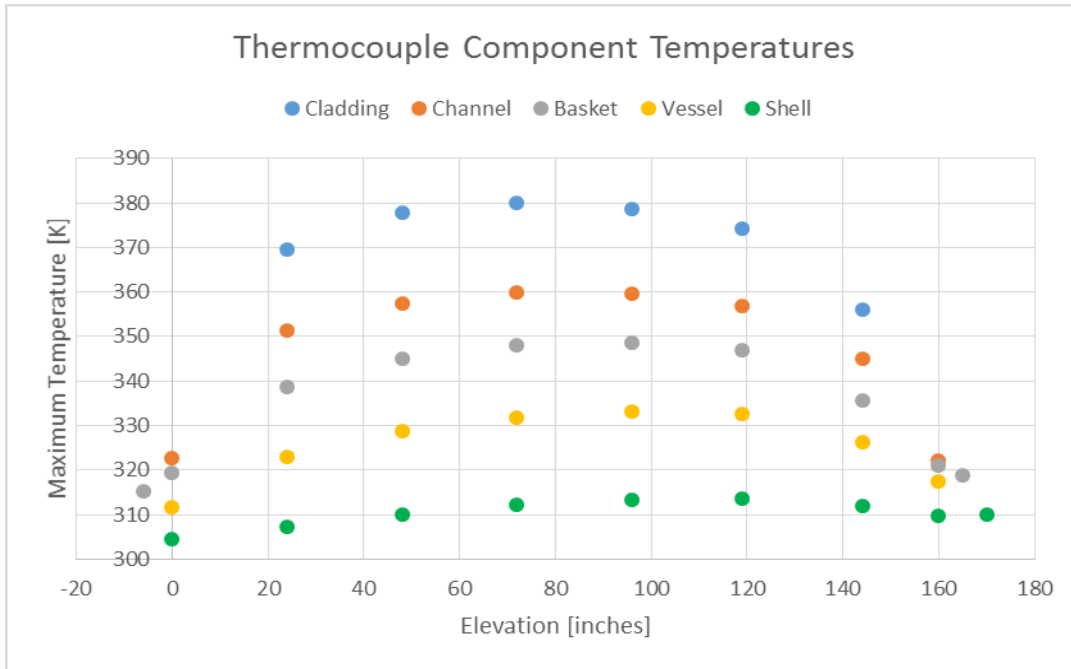


**Figure 2-10. Thermocouple component temperatures for 100 kPa and 0.5 kW.**

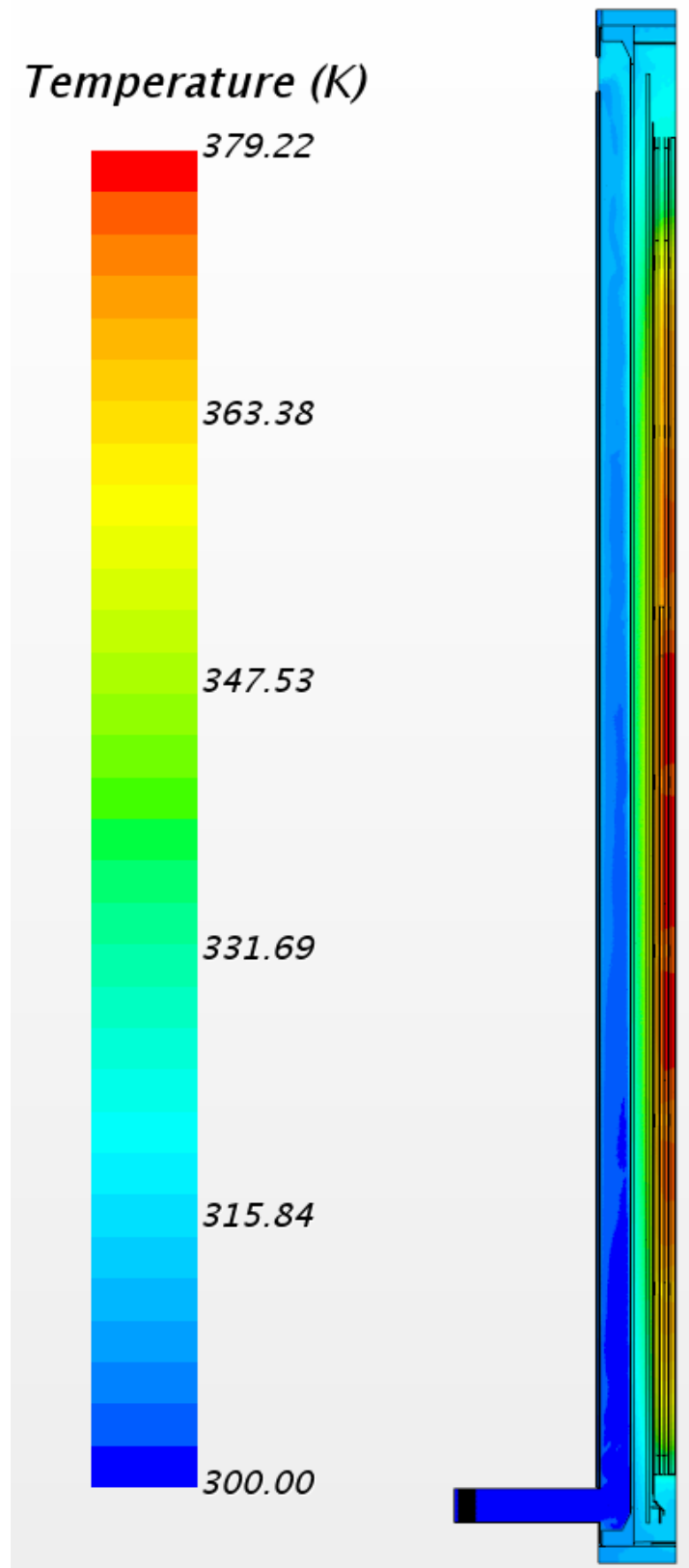


Figure 2-11. Axial temperature contour plot through assembly midsection for 100 kPa and 0.5 kW.

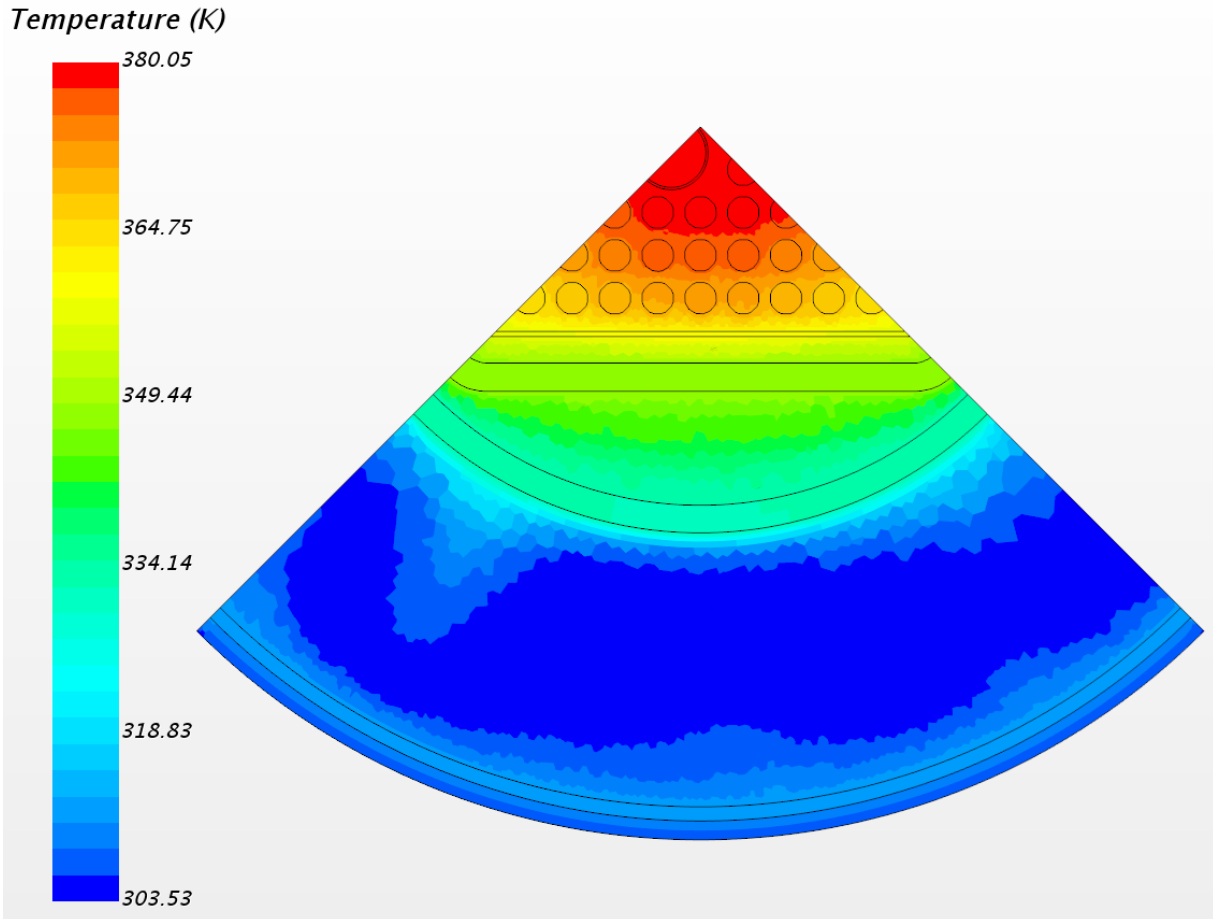


Figure 2-12. Radial temperature contour plot at the PCT elevation for 100 kPa and 0.5 kW.

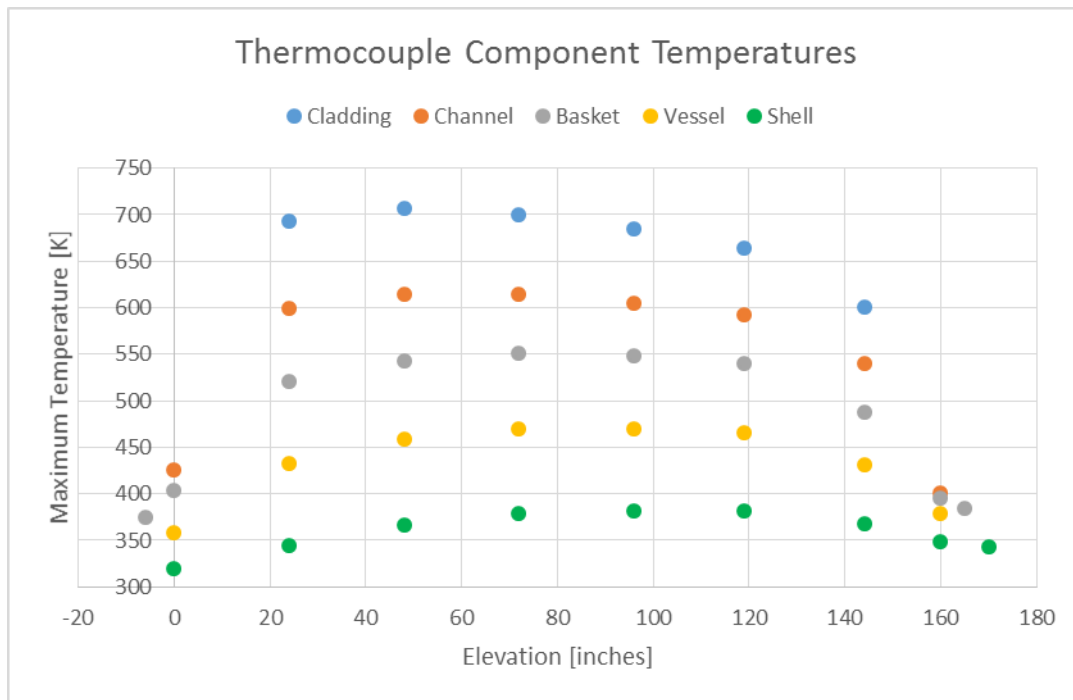
### 2.3.2 100 kPa, 5 kW

Table 2-9. Peak component temperatures for 100 kPa and 5 kW.

Component	Max Temperature[K]		
	Predicted	Measured	delta
Cladding	707	716	-9
Channel	622	631	-9
Basket	552	555	-3
Vessel	474	459	15
Shell	383	389	-6

Table 2-10. Air mass flow for 100 kPa and 5 kW.

Air Mass Flow Rate [kg/s]	
Predicted	Measured
0.0684	0.0689



**Figure 2-13. Thermocouple component temperatures for 100 kPa and 5 kW.**

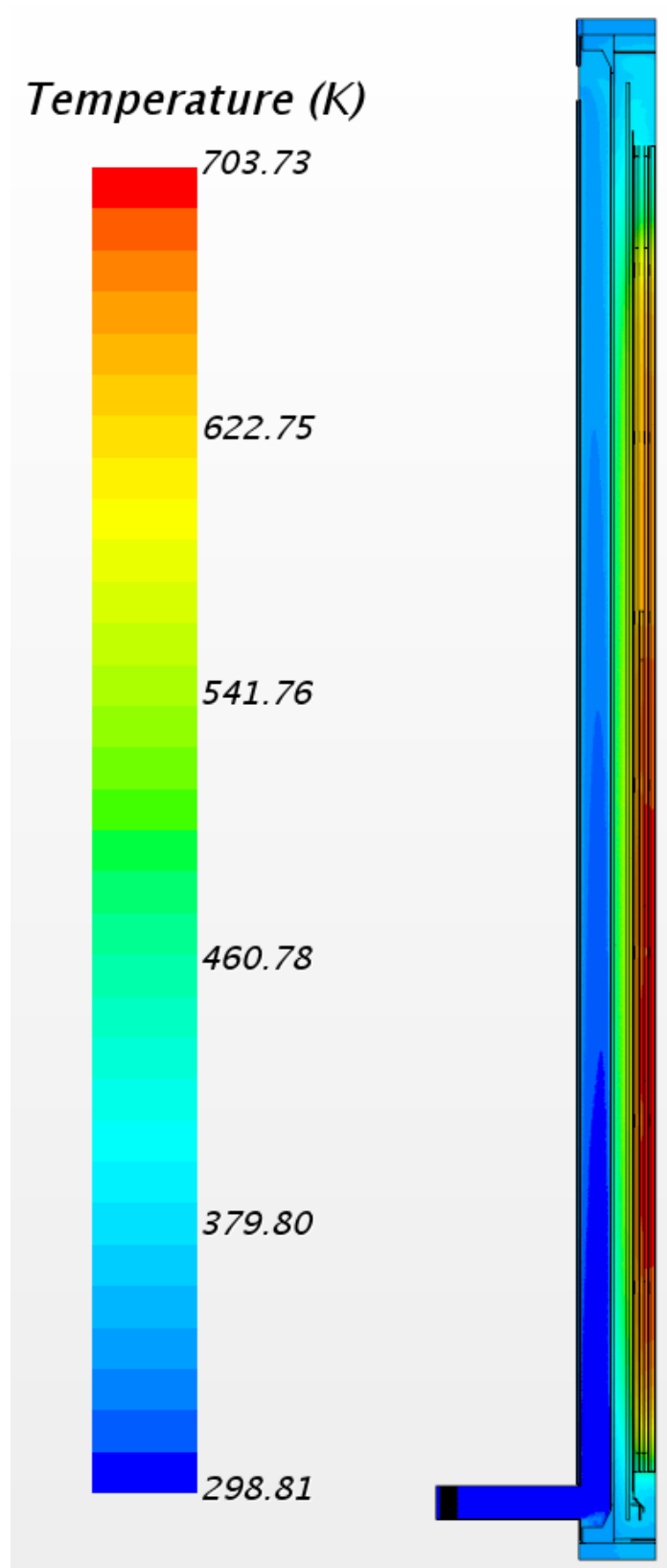


Figure 2-14. Axial temperature contour plot through assembly midsection for 100 kPa and 5 kW.

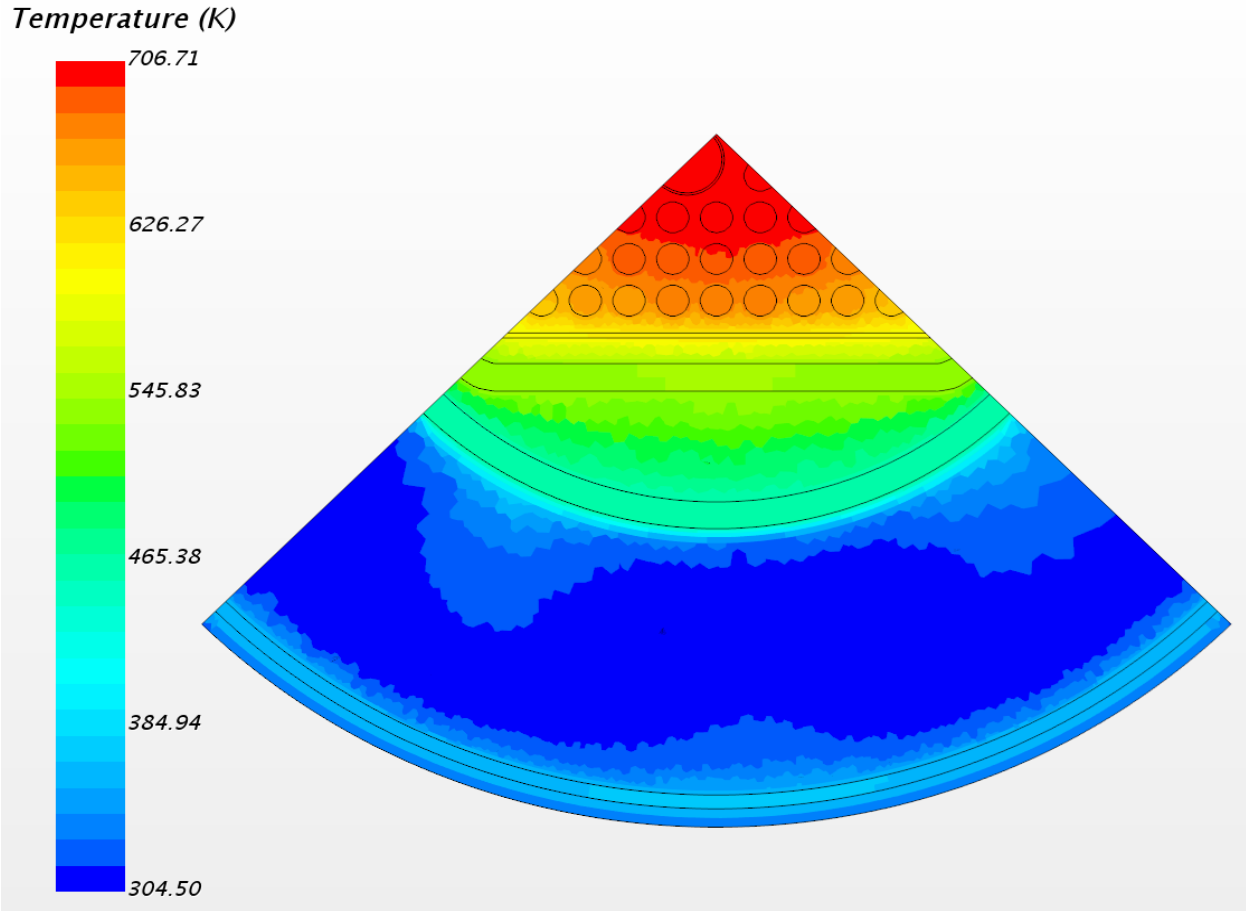


Figure 2-15. Radial temperature contour plot at the PCT elevation for 100 kPa and 5 kW.

### 2.3.3 800 kPa, 0.5 kW

Table 2-11. Peak component temperatures for 800 kPa and 0.5 kW.

Component	Max Temperatures[K]		
	Predicted	Measured	delta
Cladding	367	359	8
Channel	354	347	7
Basket	344	338	6
Vessel	333	329	4
Shell	318	312	6

Table 2-12. Air mass flow for 800 kPa and 0.5 kW.

Air Mass Flow Rate [kg/s]	
Predicted	Measured
0.0206	0.0221

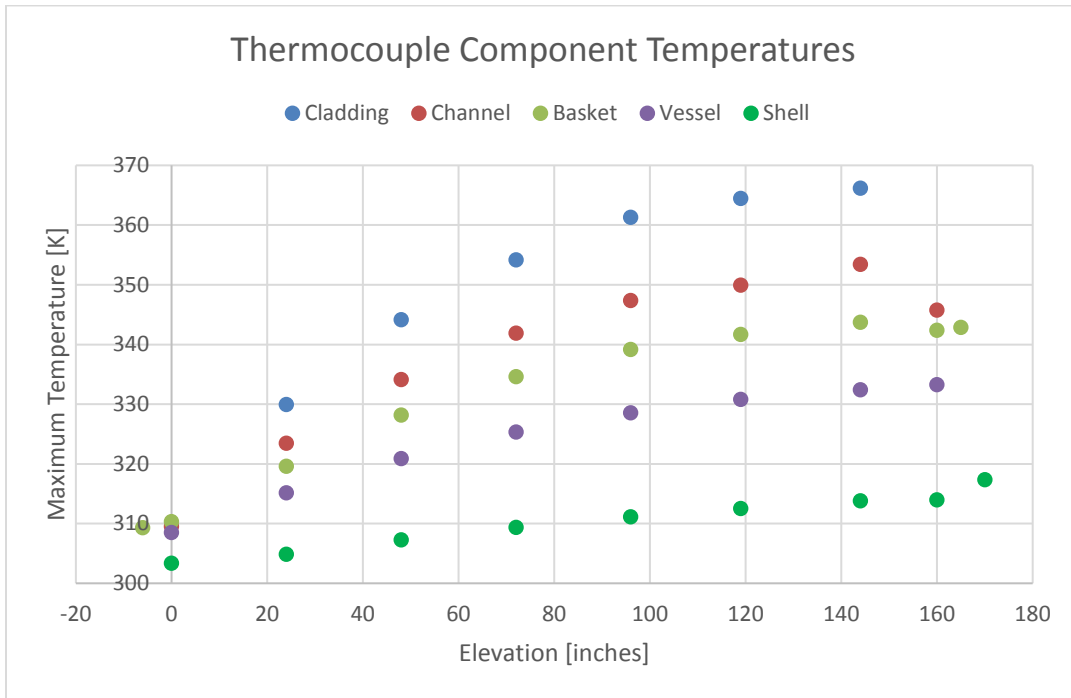


Figure 2-16. Thermocouple component temperatures for 800 kPa and 0.5 kW.

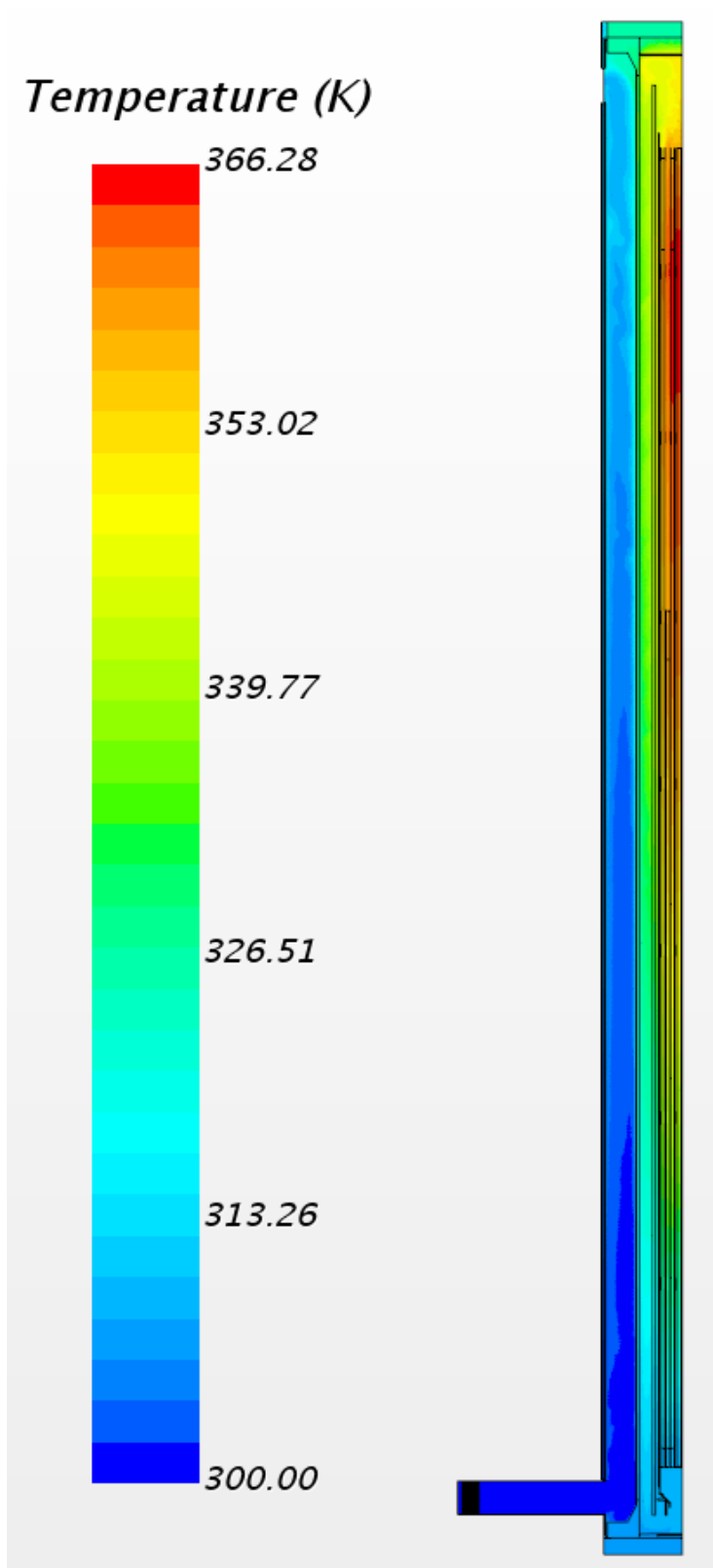


Figure 2-17. Axial temperature contour plot through assembly midsection for 800 kPa and 0.5 kW.

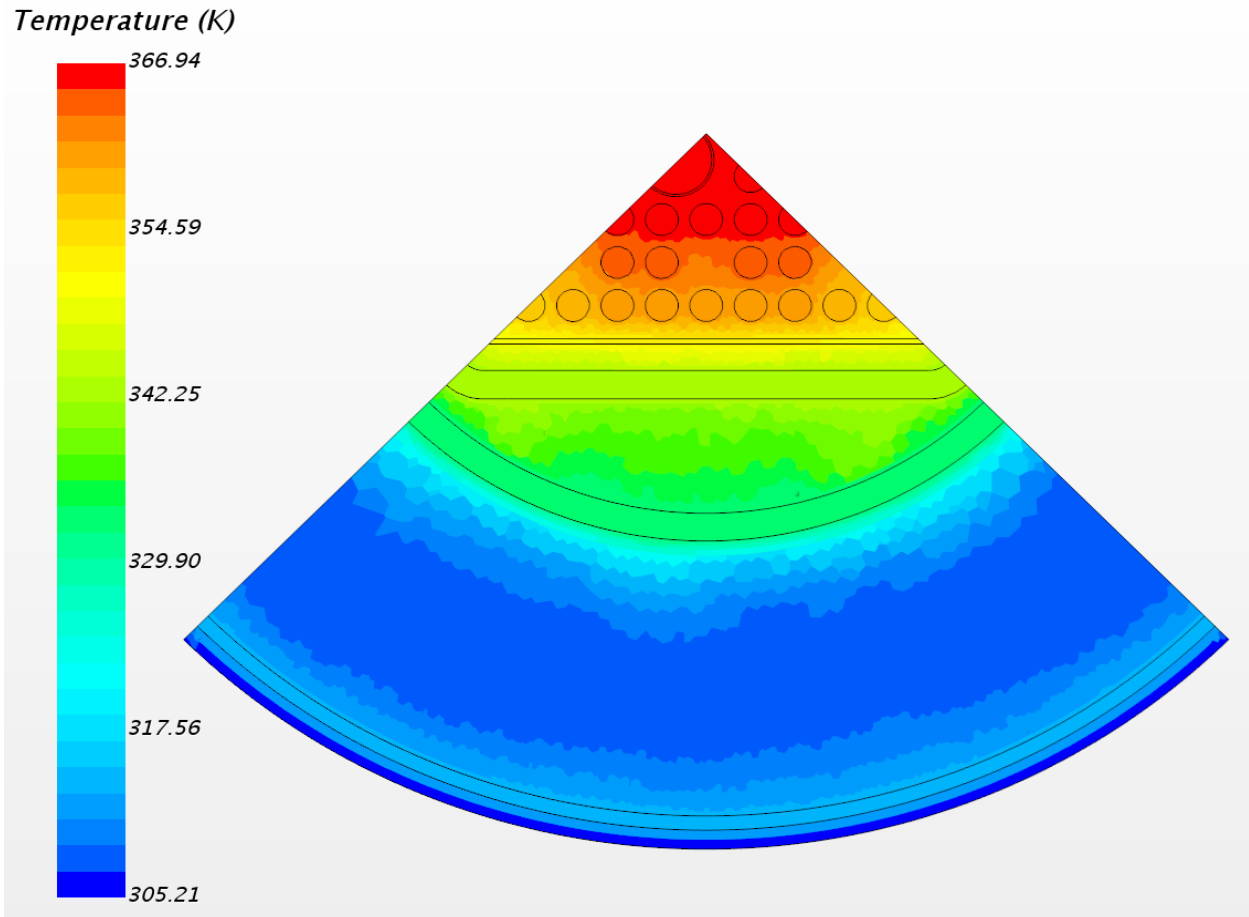


Figure 2-18. Radial temperature contour plot at the PCT elevation for 800 kPa and 0.5 kW.

### 2.3.4 800 kPa, 5 kW

Table 2-13. Peak component temperatures for 800 kPa and 5 kW.

Component	Max Temperature [K]		
	Predicted	Measured	delta
Cladding	652	659	-7
Channel	586	590	-4
Basket	534	533	1
Vessel	474	467	7
Shell	391	387	4

Table 2-14. Air mass flow for 800 kPa and 5 kW.

Air Mass Flow Rate [kg/s]	
Predicted	Measured
0.0601	0.0626

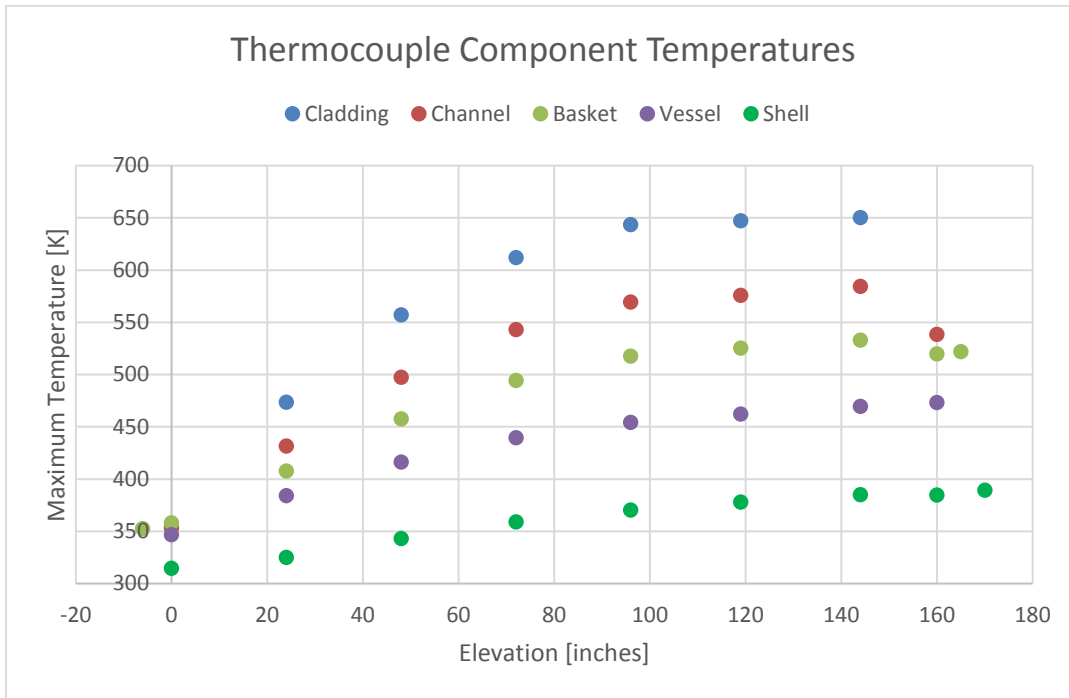


Figure 2-19. Thermocouple component temperatures for 800 kPa and 5 kW.

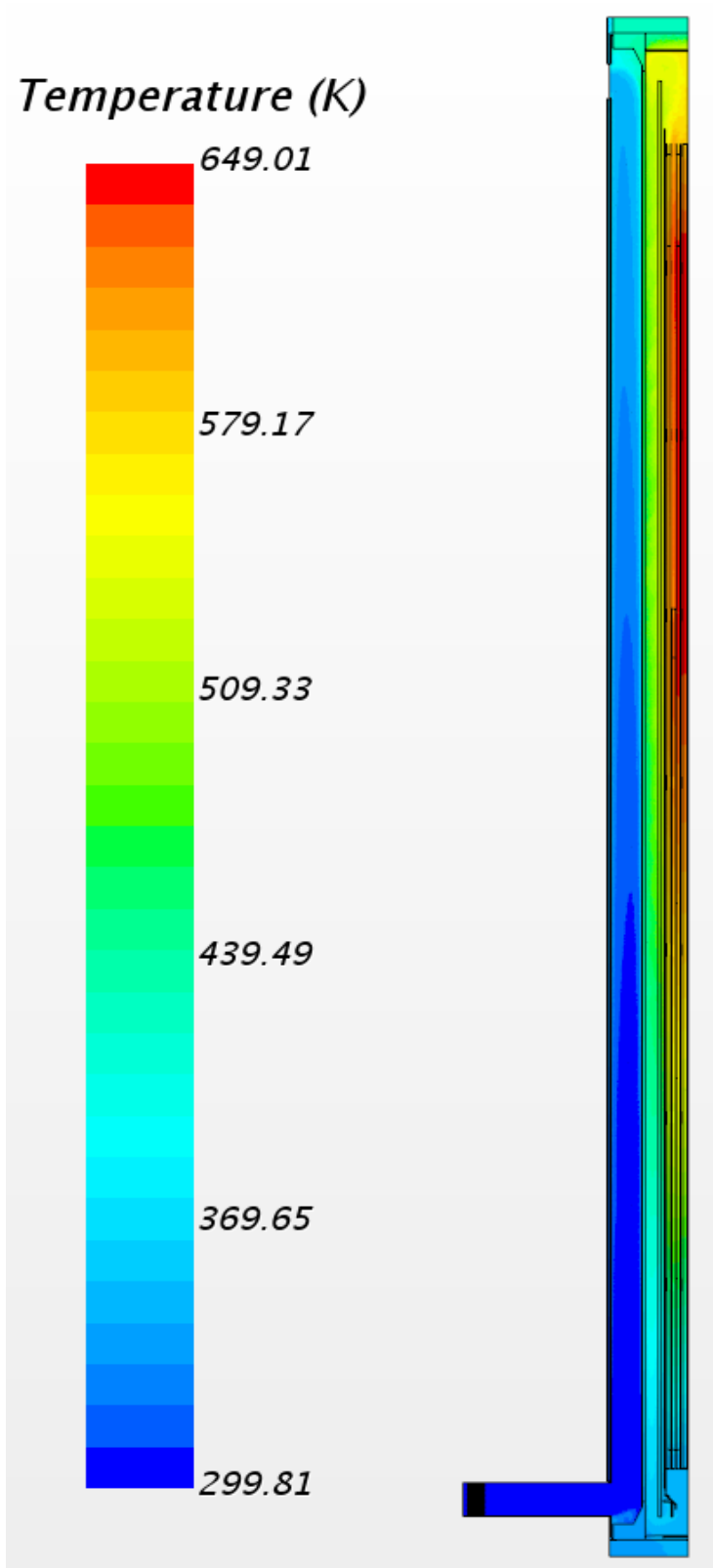


Figure 2-20. Axial temperature contour plot through assembly midsection for 800 kPa and 5 kW.

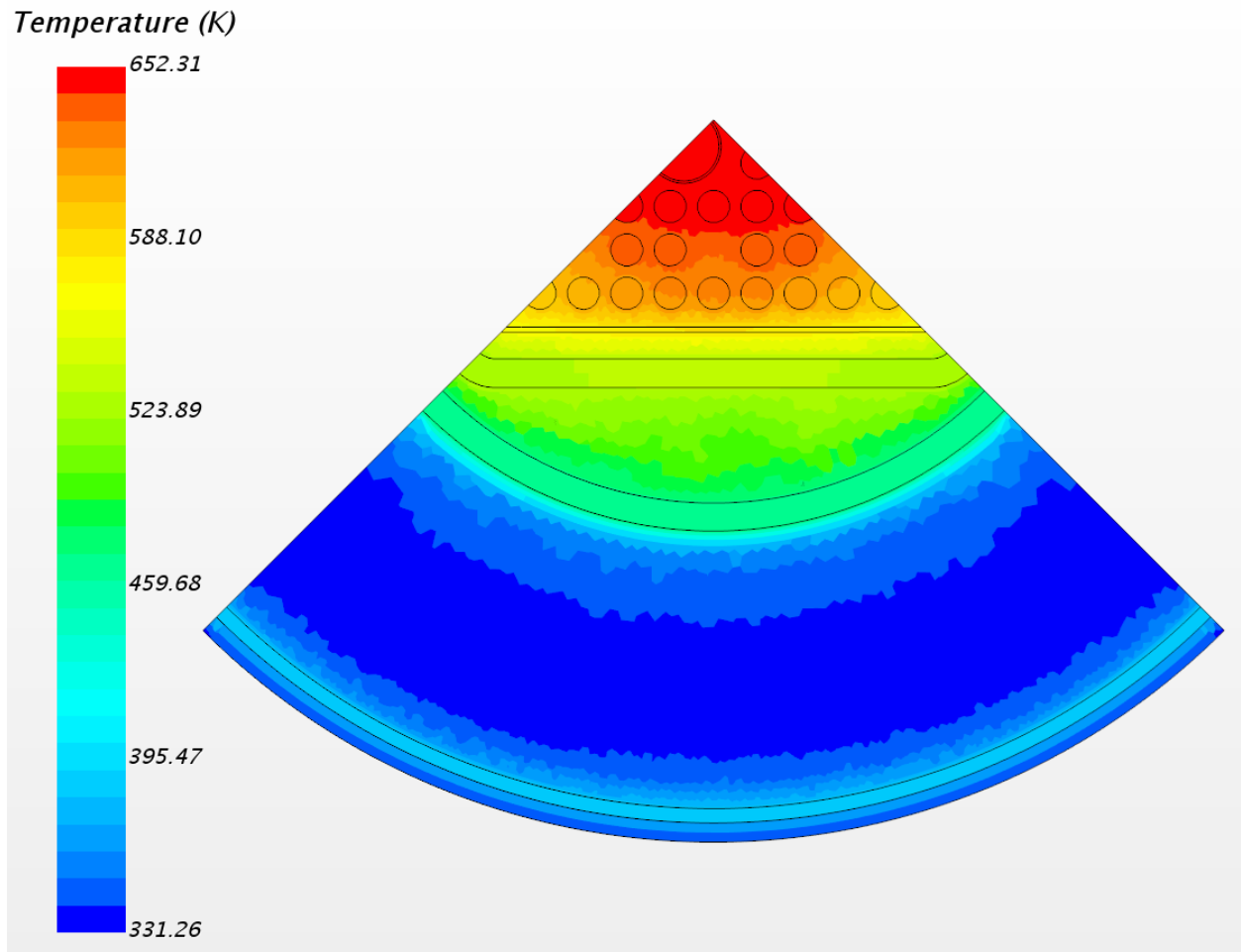


Figure 2-21. Radial temperature contour plot at the PCT elevation for 800 kPa and 5 kW.

### 3. POROUS MEDIA MODELING WITH CFD

The STAR-CCM+ model was simplified by replacing the flow straightener and fuel assembly regions with a porous region. This simplified the fuel assembly to a single region within the channel box. Removing the flow straighteners simplified the mesh near the flow inlets. The details of the porous regions and model results are presented in the following sections.

#### 3.1 Effective Thermal Conductivity

Effective thermal conductivities ( $k_{eff}$ ) were calculated separately for radial and axial heat transfer in the homogeneous region representing the fuel assembly. The radial effective thermal conductivity includes both conduction and thermal radiation. The axial effective thermal conductivity includes conduction only, neglecting any contribution from thermal radiation. These effective thermal conductivities are used for the solid fraction of the fuel region. Convective heat transfer within the rod array is represented using the flow through the porous fraction of the fuel region using loss coefficients described in Section 3.2.

##### 3.1.1 Axial $k_{eff}$ Model

The axial  $k_{eff}$  value for the fuel region was calculated assuming a volume averaging scheme. The Incoloy, MgO, and helium volumes were considered when calculating effective axial thermal conductivity. Table 3-1 lists the resulting axial  $k_{eff}$  for the fuel assembly.

**Table 3-1. Axial  $k_{eff}$  for fuel assembly.**

Axial $k_{eff}$ Fuel Assembly	
Temperature	Thermal Conductivity
[K]	[W/m-K]
300	1.5590
450	1.8632
650	2.1989
850	2.5254
1050	2.8294

##### 3.1.2 Radial $k_{eff}$ Models

For a uniform boundary temperature at the wall and a uniform heat generation rate, the radial effective thermal conductivity can be expressed as (TRW 1996):

$$k_{eff} = 0.2957 \frac{Q}{4L_a(T_c - T_{wall})} \tag{3.1}$$

where  $Q$  = total decay heat in the assembly  
 $L_a$  = active fuel length for the assembly  
 $T_c$  = peak (center) temperature of the homogeneous cross-section  
 $T_{wall}$  = uniform wall temperature

The equation gives the radial effective thermal conductivity of an assembly as a function of assembly decay heat, assembly peak temperature, and the enclosing wall temperature. The assembly decay heat is a known quantity, but the assembly wall and peak temperatures are not. To develop an appropriate radial effective thermal conductivity for the DSC fuel assembly, a detailed model of the fuel assembly was created and the peak assembly temperature was solved for various heat loads and wall temperature boundaries.

A 2-D model of the fuel assembly was set up in both COBRA-SFS and STAR-CCM+ to determine the radial effective fuel thermal conductivity. The COBRA-SFS model included both the full length and partial length rods (full array). Two different STAR-CCM+ 2-D models were set up, one that included the full array of rods (full length and partial length rods) and one that did not include the partial length rods (partial array). The emissivity of the zircaloy channel box, which is the outer temperature boundary for the fuel assembly model, was measured and found to vary with axial position (Durbin 2017). This axial distribution in emissivity of the channel box is not typical of BWR spent fuel assemblies, rather it is a result of previous test history. For the 2-D models an average emissivity value was used. The emissivity was averaged over the length of the full array and partial array length for the respective STAR-CCM+ models.

A 3-D model of the fuel assembly was also set up in STAR-CCM+ to determine the fuel  $k_{\text{eff}}$ . The 3-D model included components that the 2-D models did not, including the spacers and TC lance. It also included both the full and partial array regions in the 3-D model. The 3-D model was also able to define the surface emissivity of the zircaloy channel box as a function of elevation. The resulting calculated  $k_{\text{eff}}$  for each model is shown in Figure 3-1 and Figure 3-2.

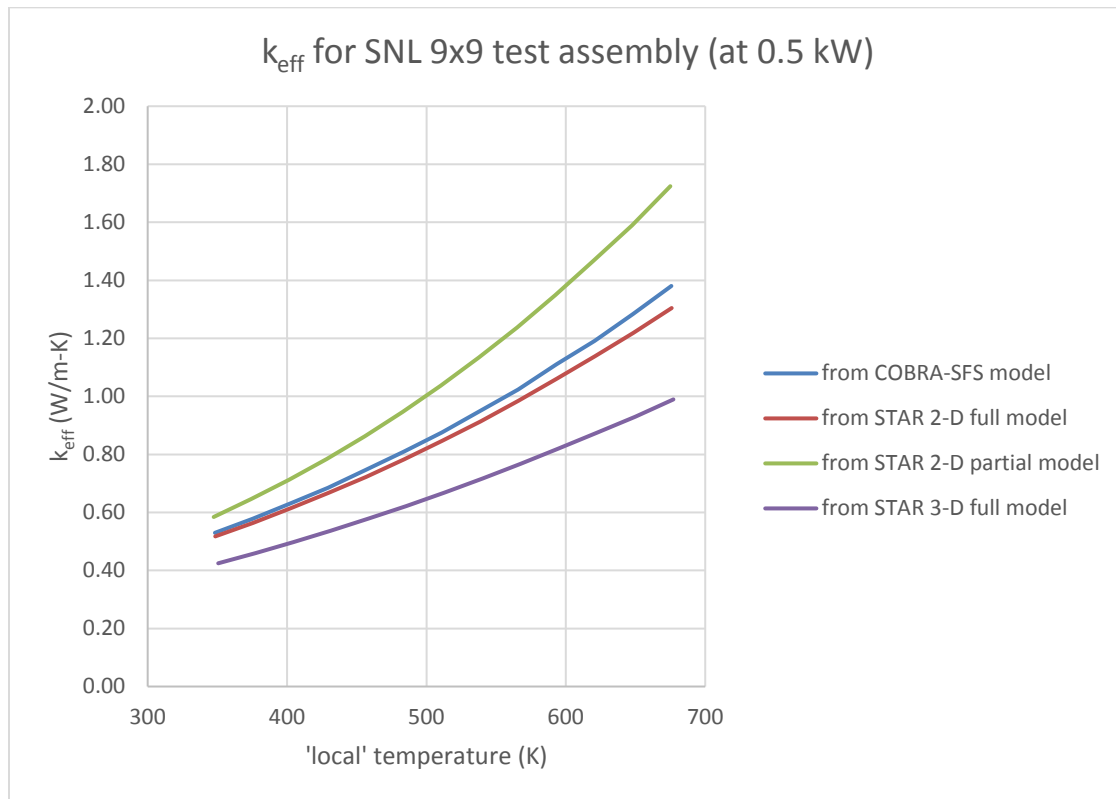


**Figure 3-1. Radial  $k_{\text{eff}}$  for DCS fuel assembly at 0.5 kW.**

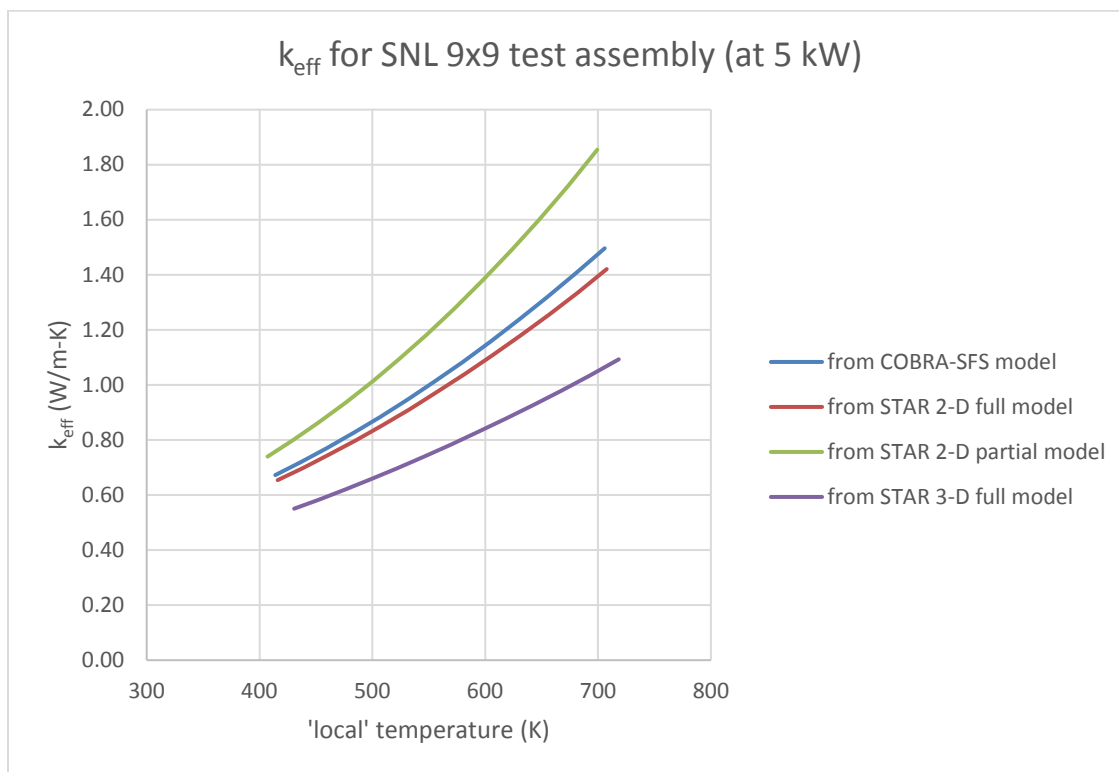


**Figure 3-2. Radial  $k_{eff}$  for DCS fuel assembly at 5 kW.**

The 2-D COBRA-SFS and STAR-CCM+ 2-D full array model gave similar results, which makes sense given they should have had similar geometry and assumptions. The 2-D STAR-CCM+ partial array model gave a significantly higher thermal conductivity than the 2-D full array models. This is most likely due to de-rating the heat load for the partial array model since it is missing eight rods. The 3-D STAR-CCM+ model provided the most conservative  $k_{eff}$ . The biggest difference between the 2-D full array models and the 3-D model was the zircaloy emissivity values. The 2-D models cannot account for the variable emissivity. A sensitivity case was run with the 3-D model in which the variable zircaloy emissivity was replaced with an average value. The resulting  $k_{eff}$  matched very closely with STAR-CCM+ 2-D full array results. Figure 3-3 shows the sensitivity case for the 5kW heat load.

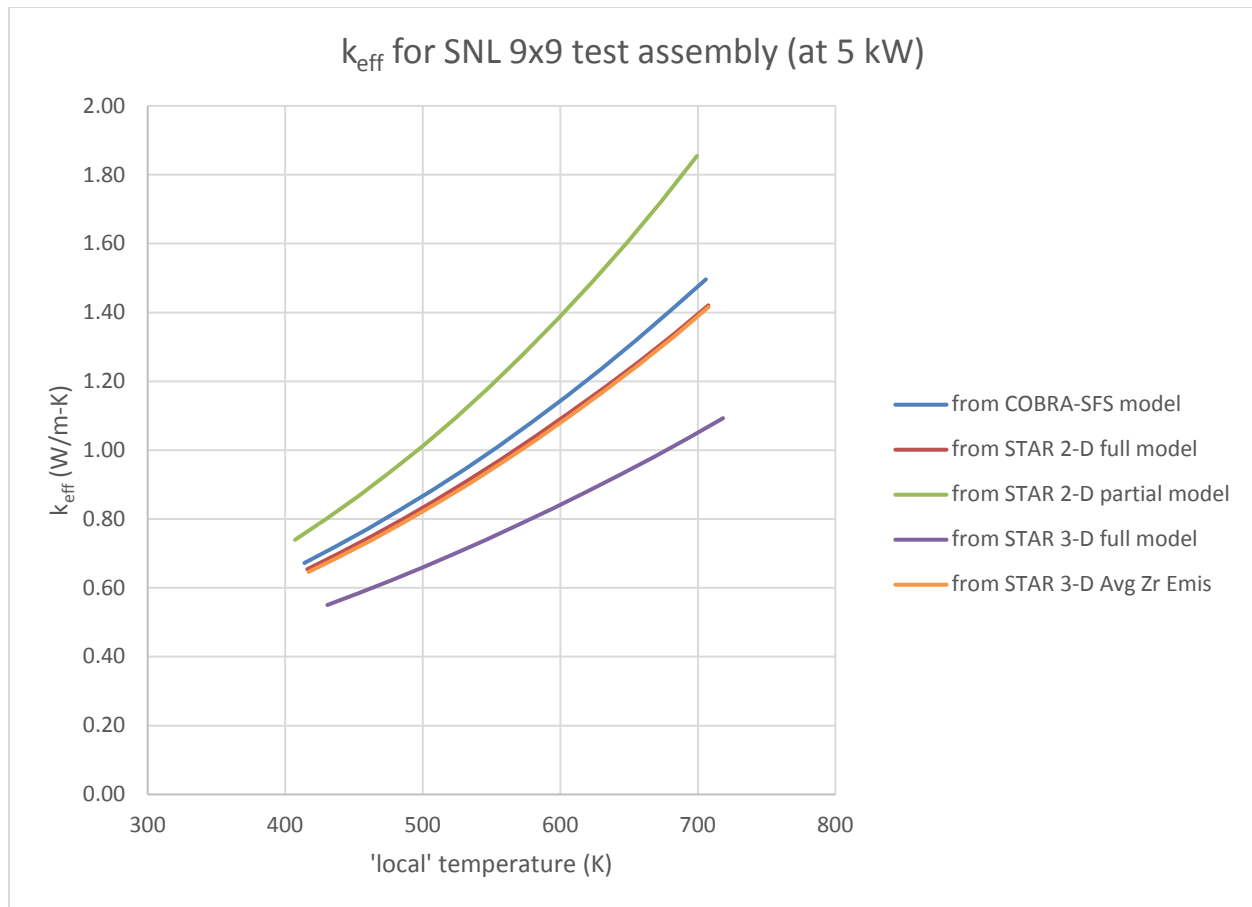


**Figure 3-3. Sensitivity case for radial  $k_{\text{eff}}$  for DCS fuel assembly at 5 kW.**

A sensitivity study was run using the porous media model of the DCS assembly to compare using the 3-D  $k_{\text{eff}}$  model and a split  $k_{\text{eff}}$  model for the full and partial array regions. For the split model the 2-D STAR-CCM+ full model was used in the full array region and the 2-D STAR-CCM+ partial model was used for the partial array region. Figure 3-4 through Figure 3-7 compare the PCTs between the detailed model, the porous media model with the split  $k_{\text{eff}}$ , and the porous media model with the 3-D  $k_{\text{eff}}$ .

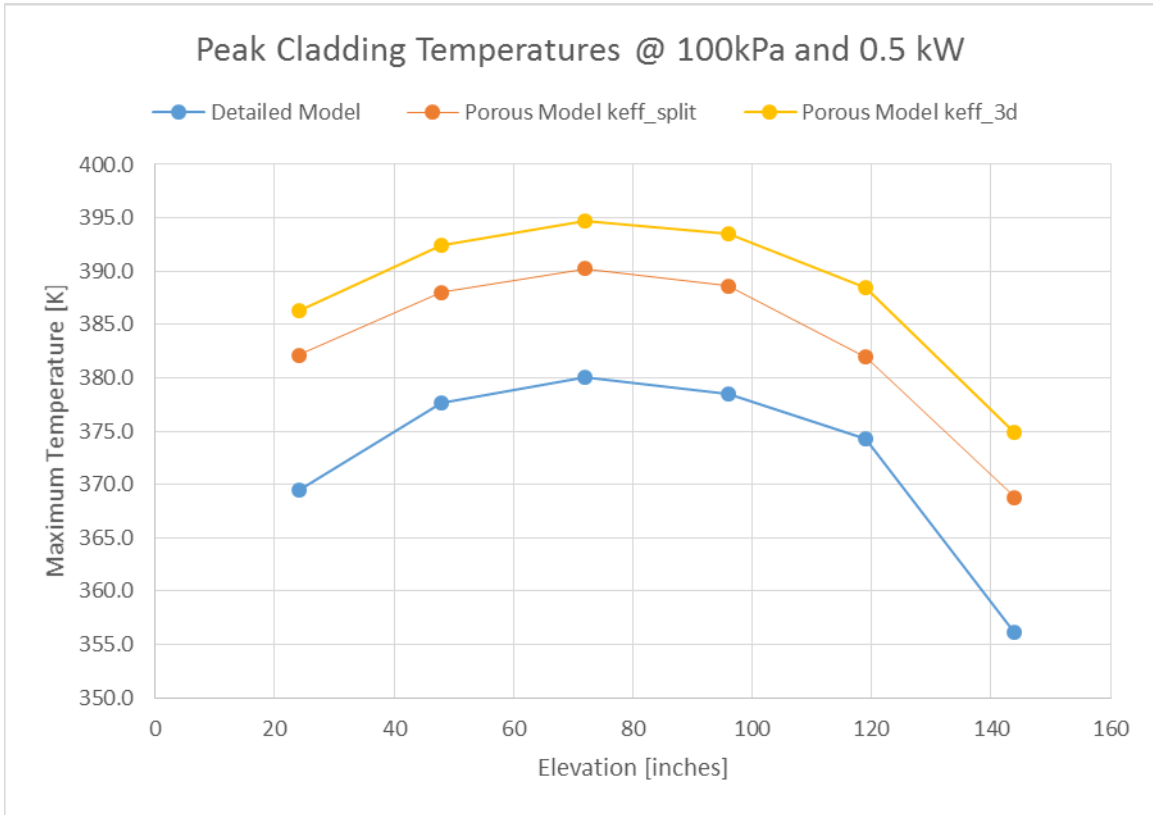


Figure 3-4. Comparison of PCT at 100 kPa and 0.5 kW.

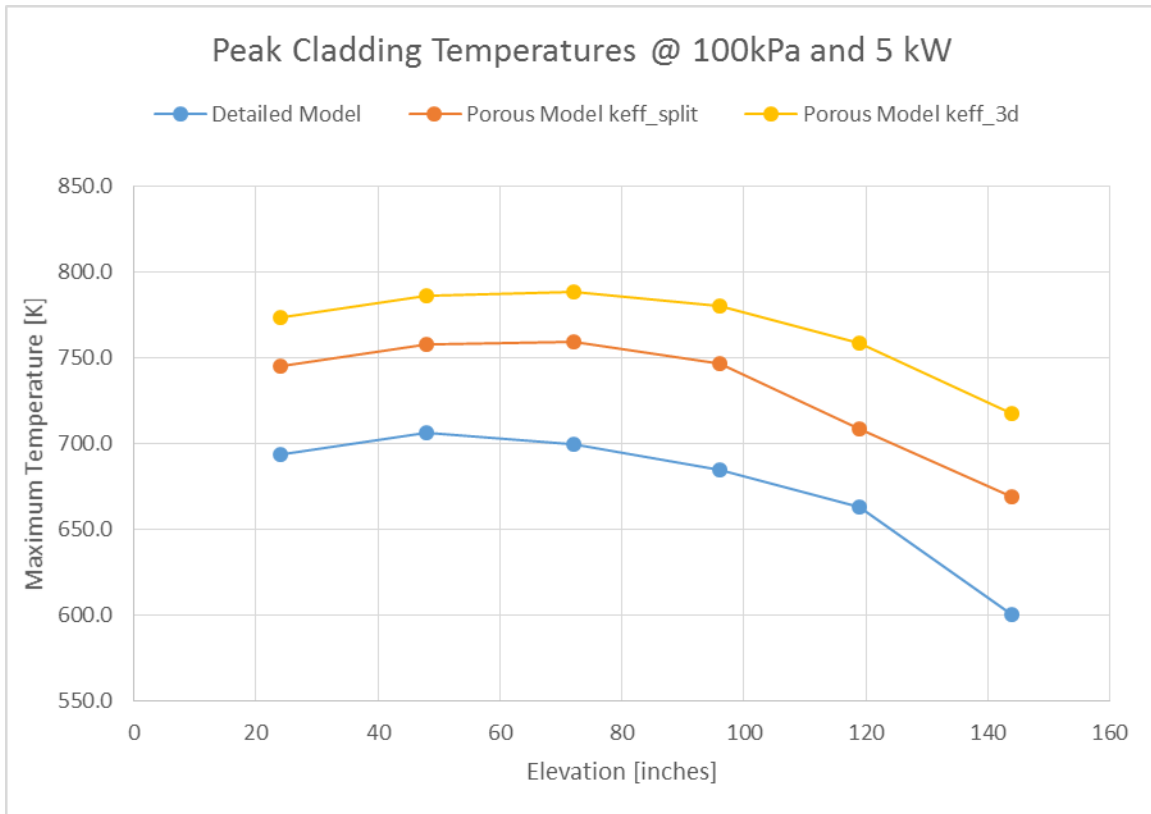


Figure 3-5. Comparison of PCT at 100 kPa and 5 kW.

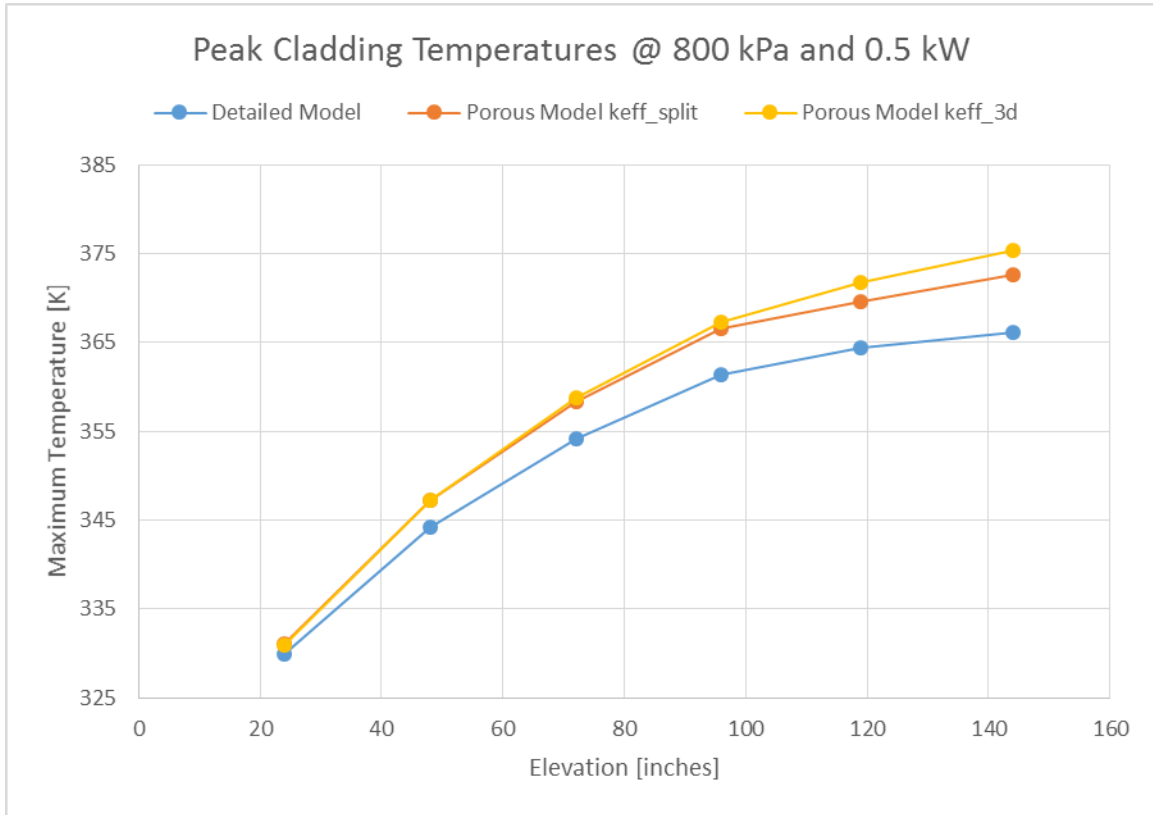
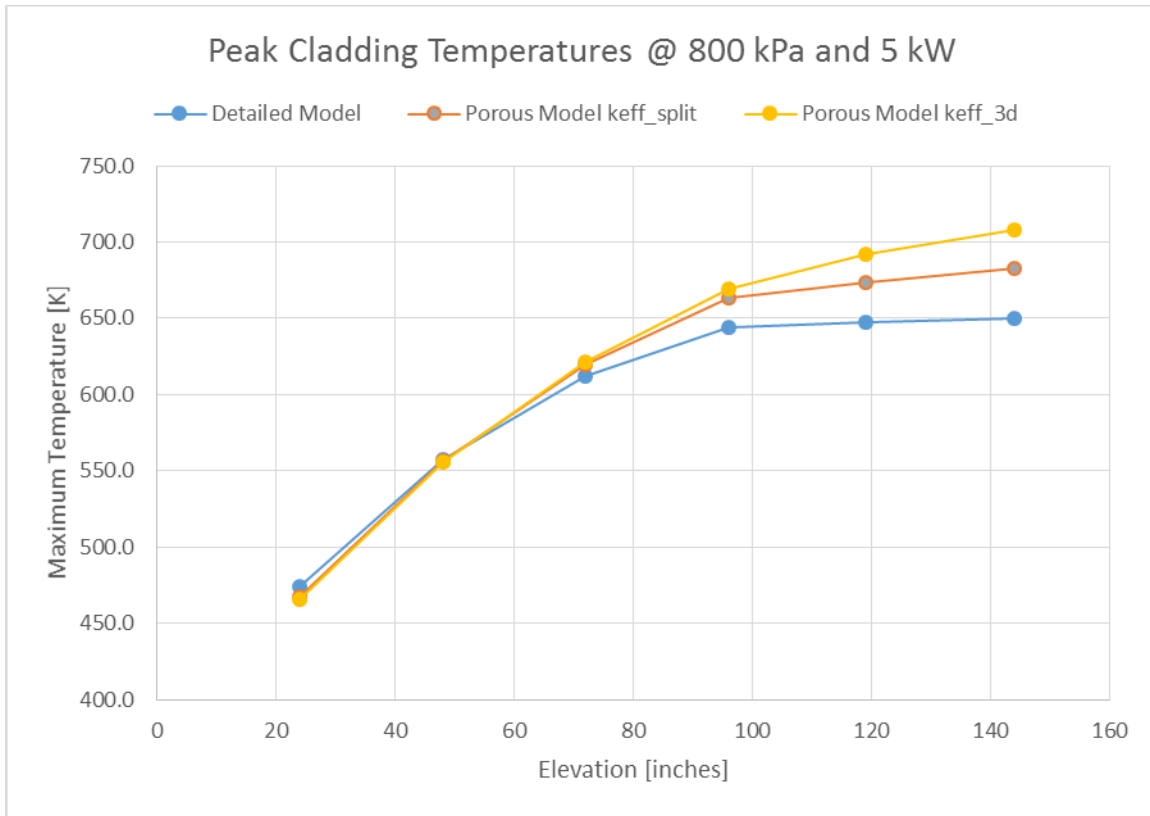


Figure 3-6. Comparison of PCT at 800 kPa and 0.5 kW.



**Figure 3-7. Comparison of PCT at 800 kPa and 5 kW.**

The plots show that both the 3-D  $k_{eff}$  model and split  $k_{eff}$  model produced conservative temperatures compared to the full detailed model. While the 3-D  $k_{eff}$  provided the most conservative temperatures, the split  $k_{eff}$  model temperatures were closer to the PCTs in the detailed model. The split  $k_{eff}$  model was used in the porous media model presented in the rest of this study.

### 3.2 Porous Flow Loss Coefficients

Porous flow loss coefficients are required for the porous flow straightener and fuel assembly regions. The loss coefficients were calculated based on detailed CFD models of each region. Pressure drops have been measured for this assembly in previous experiments (Lindgren and Durbin 2007). But, typically measured pressure drop data is not available and calculated loss coefficients are used in the construction of a cask model. Therefore, the measured pressure drop data was not included in the DSC model and instead the pressure drop was calculated for the porous regions.

Submodels for the fluid region of the flow straightener and fuel assembly were constructed. These submodels were used to determine the pressure drop across each porous region. Figure 3-8 and Figure 3-9 show the geometry for the respective flow models.

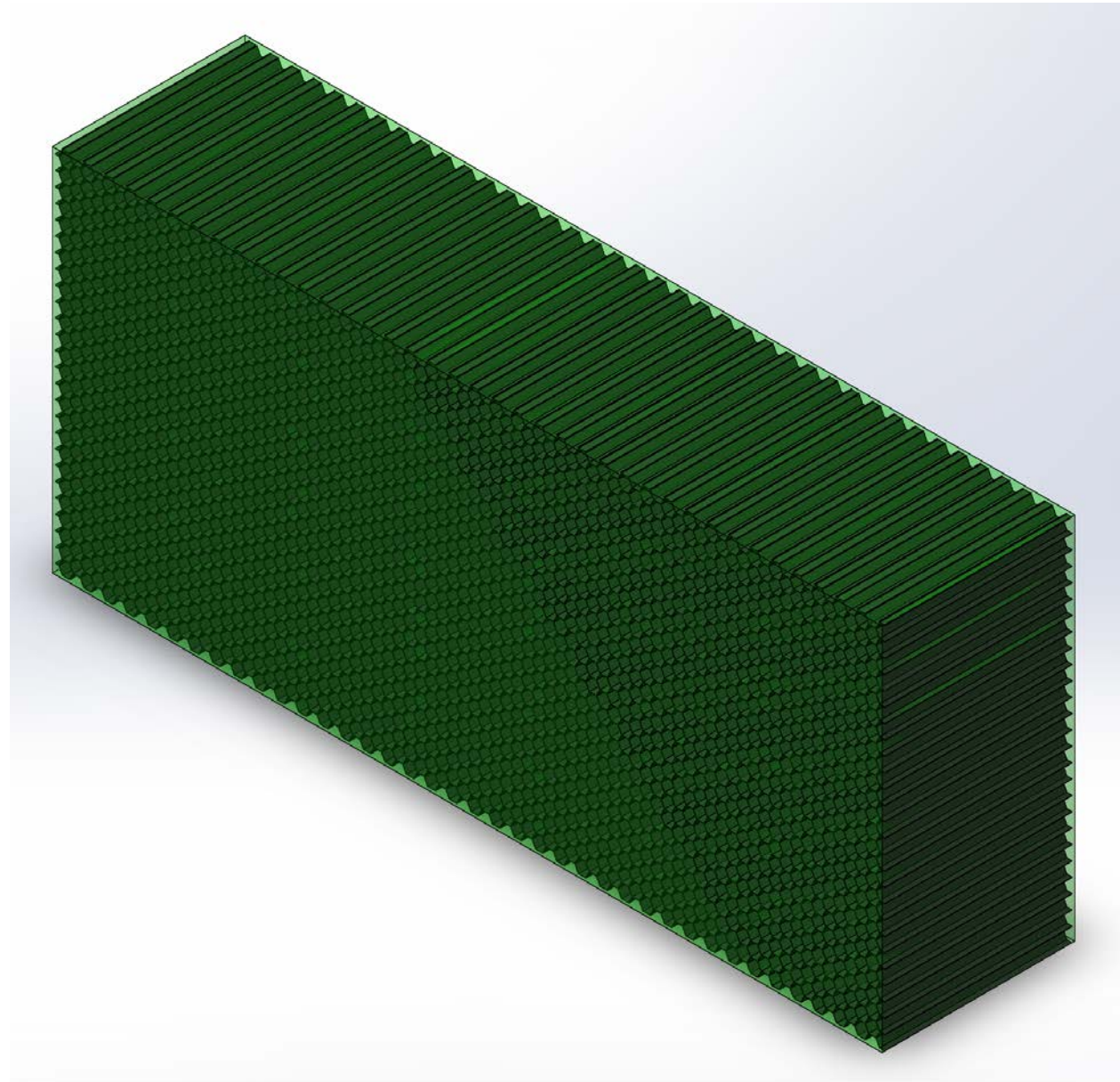
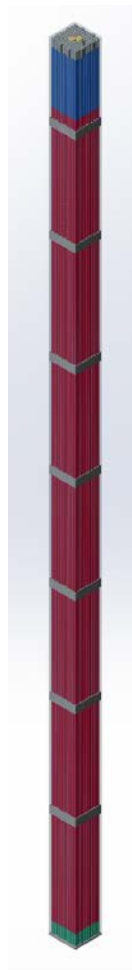


Figure 3-8. Flow straightener geometry for porous flow loss model.



**Figure 3-9. Fuel assembly geometry for porous flow loss model.**

The STAR-CCM+ user guide (Siemens PLM Software 2018) defines the inertial and viscous coefficients in the following equation:

$$\frac{\Delta P}{L} = -(\alpha v + \beta)v$$

where;

$\Delta P$  = pressure drop (Pa)

$L$  = critical length (m)

$\alpha$  = inertial coefficient ( $\text{kg}/\text{m}^4$ )

$v$  = superficial velocity (m/s)

$\beta$  = viscous coefficient ( $\text{kg}/\text{m}^3\text{-s}$ )

Each model was run with various inlet velocities and the resulting pressure drop per length was plotted. Figure 3-10 and Figure 3-11 show the resulting plots and give an equation for the pressure drop per length with respect to superficial velocity. The coefficients for the equation on the plots correspond to the inertial and viscous coefficients. These coefficients are listed in Table 3-2.

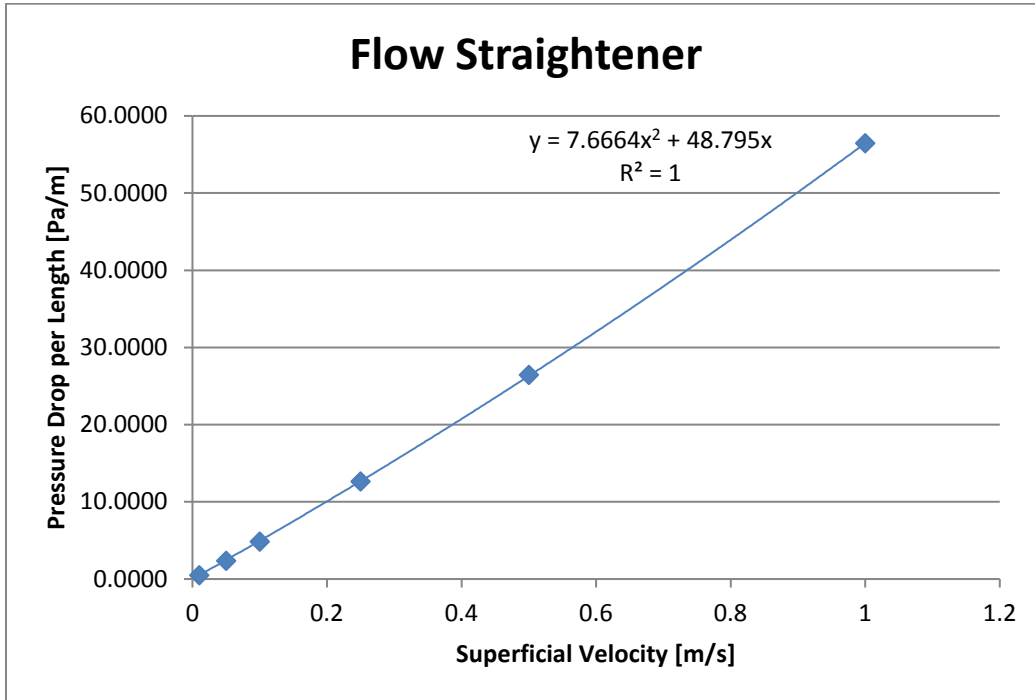


Figure 3-10. Pressure drop vs. superficial velocity for flow straightener model.

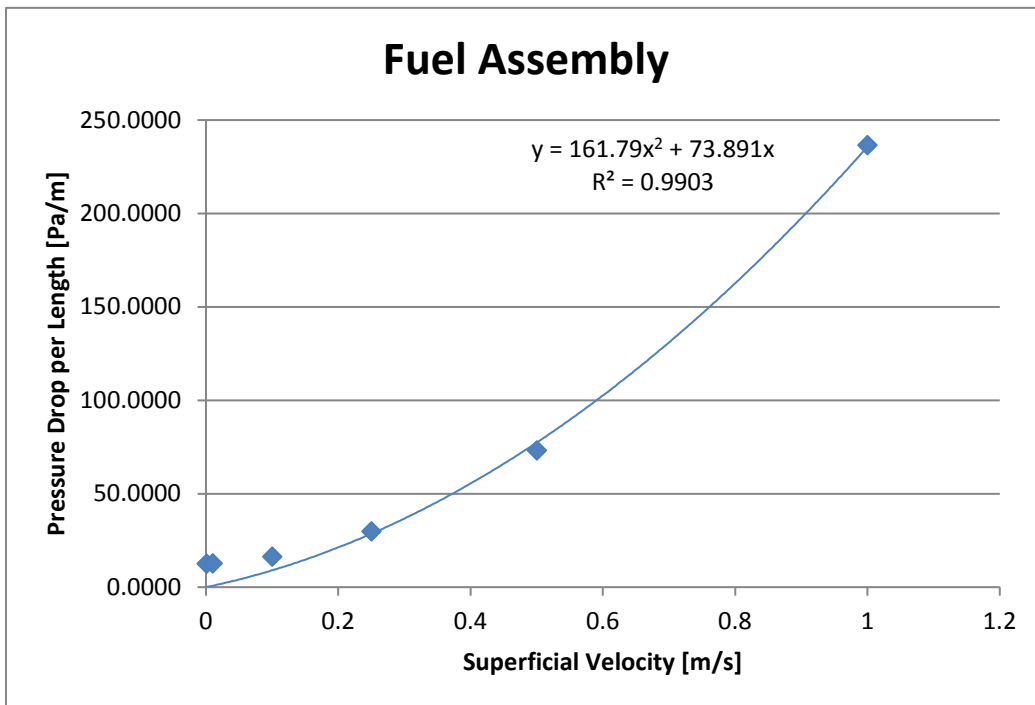


Figure 3-11. Pressure drop vs. superficial velocity for fuel assembly model.

**Table 3-2. Calculated porous loss coefficients.**

Component	Axial Inertial Coefficient $\alpha$ [kg/ m <sup>4</sup> ]	Axial Viscous Coefficient $\beta$ [kg/m <sup>3</sup> -s]
Fuel Assembly	161.8	73.9
Flow Straightener	7.67	48.8

### 3.3 Mesh Sensitivity

A mesh sensitivity study was run with the porous media model to verify the mesh was sufficiently resolved. A mesh sensitivity study was not run for the detailed model since a very refined mesh was required in order to explicitly model all parts. The initial mesh for the porous media model was refined such that the cell count was doubled across the air annulus. The refined case was also further refined to increase the cell count across the air annulus. Figure 3-12 through Figure 3-14 show a radial cross-section of the three different meshes. Table 3-3 gives the cell, face, and vertices count for the three meshes. All three meshes were run for the 800 kPa and 5 kW case. The resulting PCT and airflow for the three mesh cases are shown in Table 3-4. The results show that the refined and very refined mesh produced similar results with a PCT of 684K for each case. The default/coarse mesh also showed good agreement with the refined and very refined meshes with a resulting PCT within 1 degree of the other meshes. Airflow was slightly under predicted for the default/coarse mesh when compared with the refined and very refined cases.

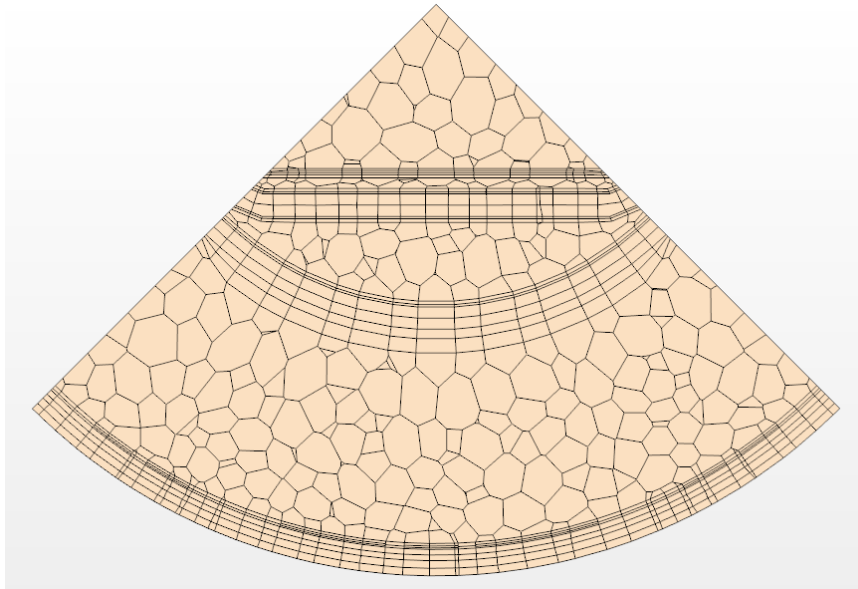


**Figure 3-12. Initial mesh configuration – radial cross-sectional view of DSC assembly.**

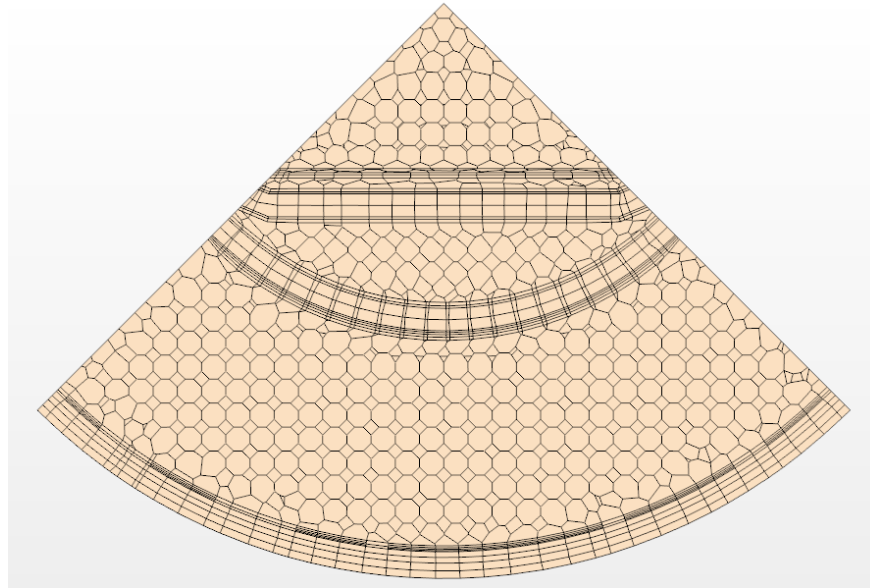


Figure 3-13. Refined mesh configuration – radial cross-sectional view of DSC assembly.

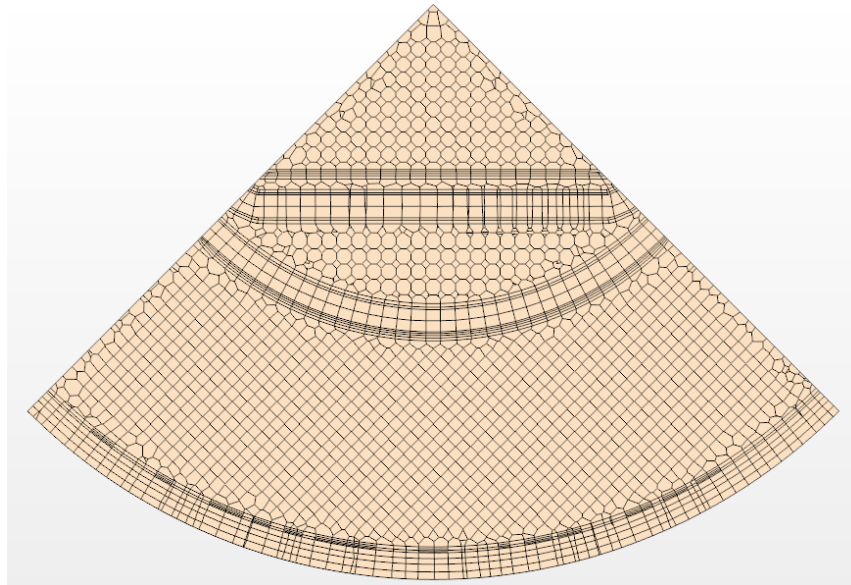


Figure 3-14. Very refined mesh configuration – radial cross-sectional view of DSC assembly.

Table 3-3. Mesh details for mesh sensitivity study.

Mesh	# Cells	Solver Time	# Faces	# Vertices
Default	308697	0.44 hrs	1370752	1090114
Refined	700002	0.93 hrs	3615718	2926131
Very Refined	2164639	1.96 hrs	12214134	10070256

**Table 3-4. Mesh sensitivity results @ 800 kPa and 5 kW.**

Mesh	PCT [K]	Air Mass Flow Rate [kg/s]
Default	683.25	0.0536
Refined	683.90	0.0595
Very Refined	683.69	0.0594

Using these results, an estimate of discretization error can be obtained by determining the Grid Convergence Index (GCI). This parameter is calculated following the approach outlined in Roach (2009).

The estimated fractional error,  $E_1$ , for the fine grid solution  $f_1$ , is calculated as

$$E_1[\text{fine grid}] = \frac{\varepsilon}{r^p - 1}$$

$$\varepsilon = \frac{f_2 - f_1}{f_1}$$

In this approach,  $\varepsilon$  is the relative change in the solution for two meshes, with  $f_1$  designating the fine mesh solution and  $f_2$  the solution for the coarse mesh. The  $r$  term is the refinement ratio of the two meshes  $f_1$  and  $f_2$ . The exponent  $p$  on the refinement ratio is the order of the solution method, which in this case is second order, so  $p = 2$ . Ideally, the mesh is refined by a ratio of two in each dimension, so  $r^p = 2^2 = 4$ . This is often impractical, and the refinement ratio need not be identically two.

For an unstructured mesh, an effective refinement ratio is

$$\text{effective } r = \left( \frac{N_1}{N_2} \right)^{1/D}$$

where  $N_1$  and  $N_2$  are the total cell count for the fine and course meshes, respectively and  $D$  is the dimensionality of the system. The GCI is obtained by multiplying the absolute value of the estimated fractional error,  $E_1$ , by a scale factor. The calculation here uses the recommended value of 3.

$$GCI[\text{fine grid}] = 3 \frac{|\varepsilon|}{r^p - 1}$$

Applying this for the cell counts of the different mesh resolutions shown in Table 3-3 and the model results for PCT in Table 3-4 yields the two estimates of GCI shown in Table 3-5. In the first case, the comparison is between the fine mesh and the coarse mesh, which corresponds to a refinement ratio of nearly two. The second case compares the fine mesh and medium mesh solutions. For these two cases, it is prudent to use the larger of the two estimates. So, for a PCT on the order of 684 K, an estimate of the relative numerical error for the medium mesh solution is  $0.000837 \times 6834$  K, which is 0.6 K. Note that the GCI is not a bounding error estimate, rather an indication of the relative error.

**Table 3-5. Grid convergence index.**

$N_1$	$N_2$	$f_1$	$f_2$	$r$	$\epsilon$	$E_1$	GCI [fine grid]
2164639	308697	683.69	683.25	1.91	0.000644	0.000242	0.000725
2164639	700002	683.69	683.90	1.46	0.000313	0.000279	0.000837

In summary, the mesh sensitivity test results shown in Table 3-5 demonstrate satisfactory predictions for all three mesh cases. This is good news for modeling of a typical storage system where a coarse mesh would be desirable. In light of the improved results and consistency with the very refined mesh, the refined mesh was used for the porous media model presented in the rest of this study. The quarter porous media model reduced the total solver time by ~ 93% on average from the detailed quarter model.

### 3.4 Results

This section describes the porous media modeling results presented in Table 3-6 through Table 3-13 and in Figure 3-15 through Figure 3-26.

#### 3.4.1 100 kPa, 0.5 kW

**Table 3-6. Peak component temperatures for 100 kPa and 0.5 kW.**

Component	Max Temperatures [K]		
	Predicted	Measured	delta
Cladding	391	376	15
Channel	361	359	2
Basket	349	344	5
Vessel	333	328	5
Shell	313	312	1

**Table 3-7. Air mass flow for 100 kPa and 0.5 kW.**

Air Mass Flow Rate [kg/s]	
Predicted	Measured
0.0239	0.0264

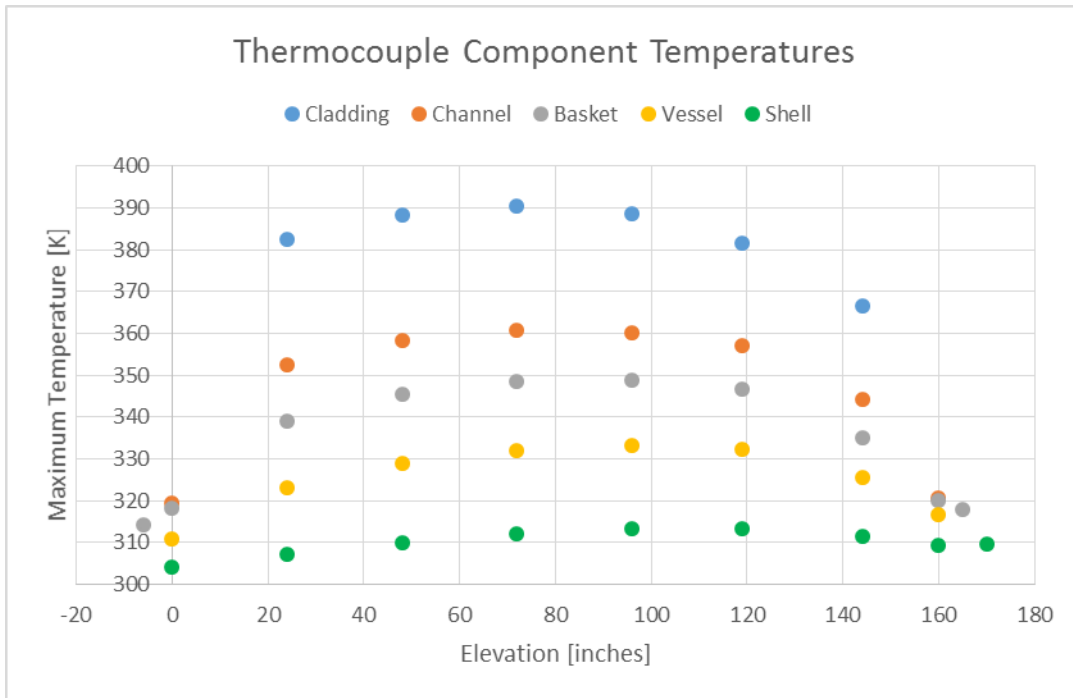


Figure 3-15. Thermocouple component temperatures for 100 kPa and 0.5 kW.

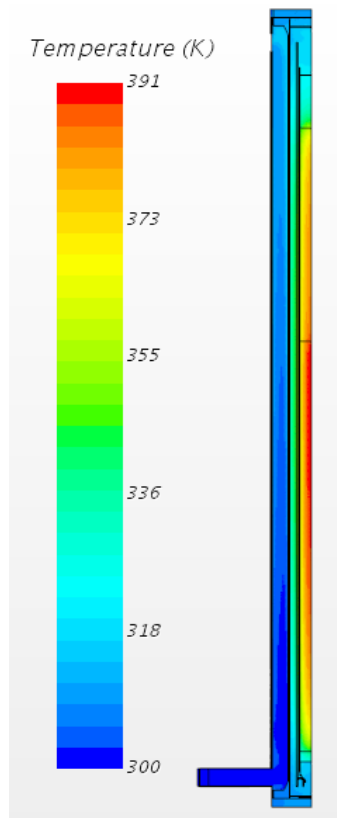


Figure 3-16. Axial temperature contour plot through assembly midsection for 100 kPa and 0.5 kW.

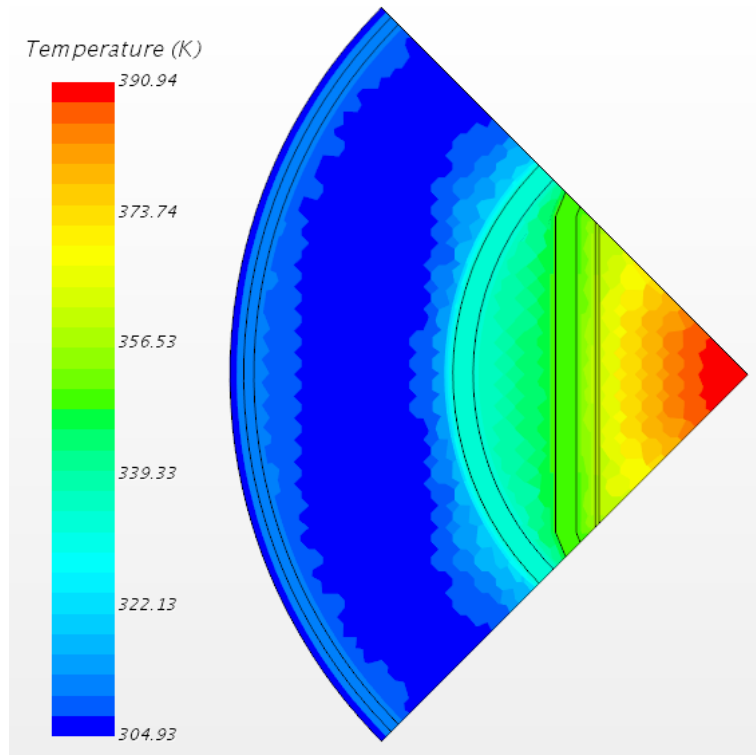


Figure 3-17. Radial temperature contour plot at the PCT elevation for 100 kPa and 0.5 kW.

### 3.4.2 100 kPa, 5 kW

Table 3-8. Peak component temperatures for 100 kPa and 5 kW.

Component	Max Temperatures [K]		
	Predicted	Measured	delta
Cladding	759	716	43
Channel	620	631	-11
Basket	552	555	-3
Vessel	472	459	13
Shell	381	389	-8

Table 3-9. Air mass flow for 100 kPa and 5 kW.

Air Mass Flow Rate [kg/s]	
Predicted	Measured
0.0682	0.0689

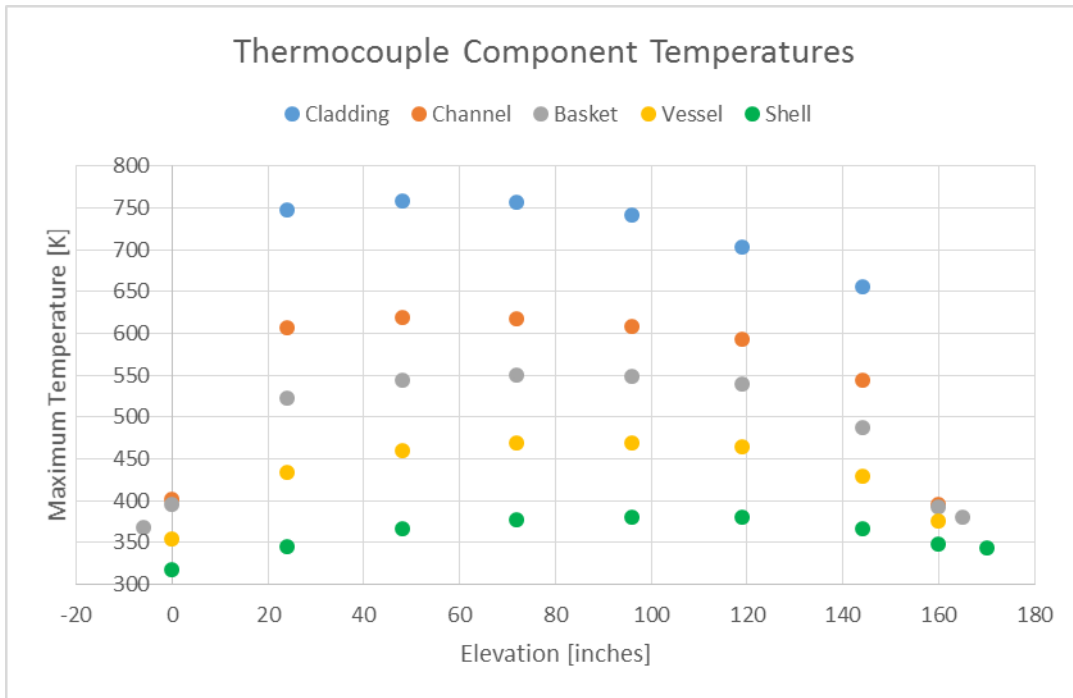


Figure 3-18. Thermocouple component temperatures for 100 kPa and 5 kW.

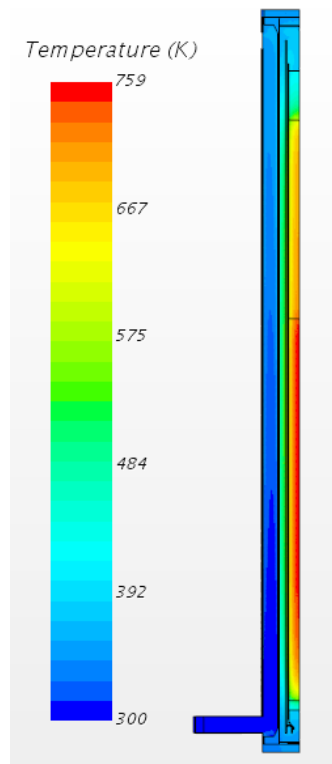


Figure 3-19. Axial temperature contour plot through assembly midsection for 100 kPa and 5 kW.

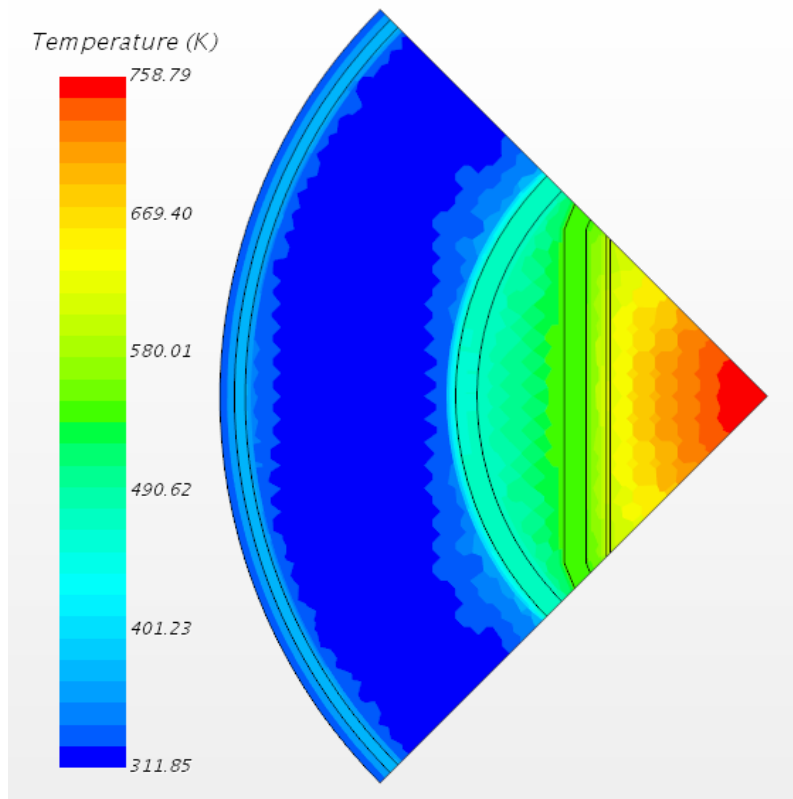


Figure 3-20. Radial temperature contour plot at the PCT elevation for 100 kPa and 5 kW.

### 3.4.3 800 kPa, 0.5 kW

Table 3-10. Peak component temperatures for 800 kPa and 0.5 kW.

Component	Max Temperatures [K]		
	Predicted	Measured	delta
Cladding	374	359	15
Channel	354	347	7
Basket	345	338	7
Vessel	334	329	5
Shell	319	312	7

Table 3-11. Air mass flow for 800 kPa and 0.5 kW.

Air Mass Flow Rate [kg/s]	
Predicted	Measured
0.0203	0.0221

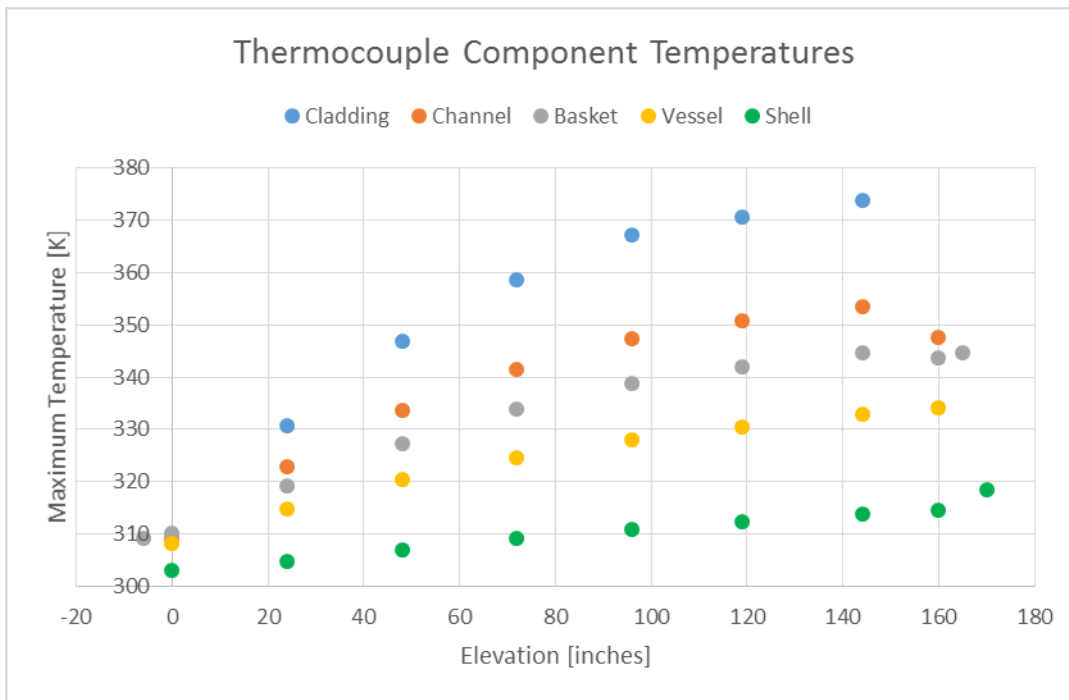


Figure 3-21. Thermocouple component temperatures for 800 kPa and 0.5 kW.

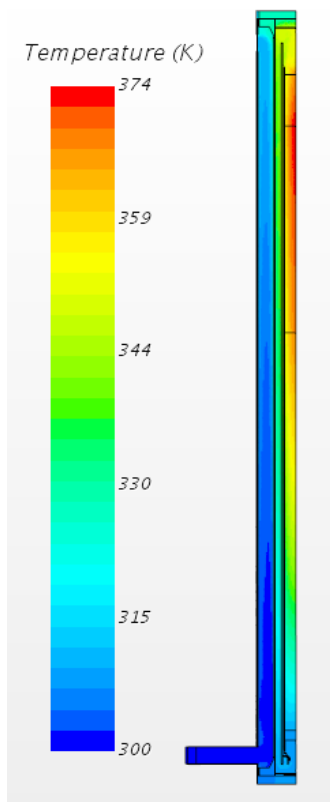


Figure 3-22. Axial temperature contour plot through assembly midsection for 800 kPa and 0.5 kW.

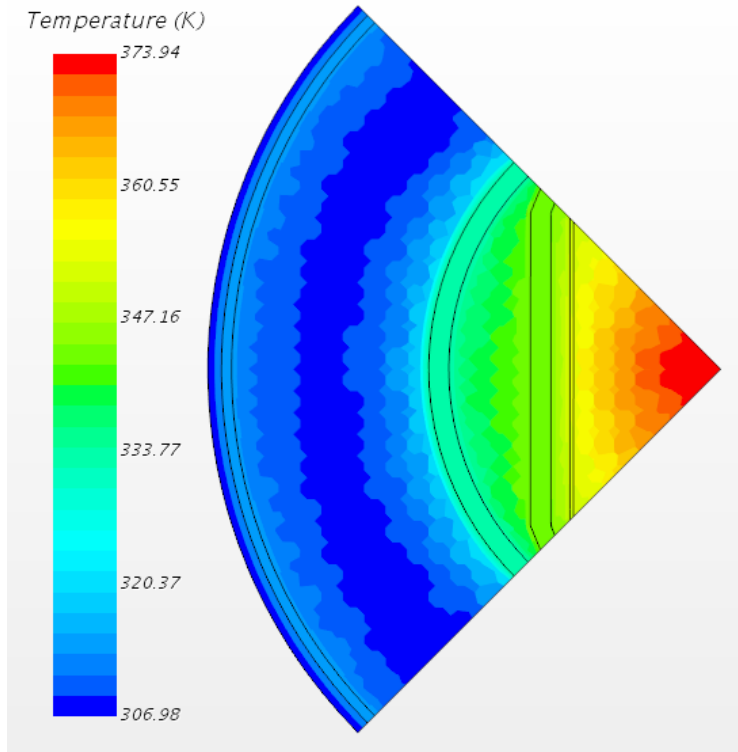


Figure 3-23. Radial temperature contour plot at the PCT elevation for 800 kPa and 0.5 kW.

### 3.4.4 800 kPa, 5 kW

Table 3-12. Peak component temperatures for 800 kPa and 5 kW.

Component	Max Temperatures [K]		
	Predicted	Measured	delta
Cladding	684	659	25
Channel	588	590	-2
Basket	540	533	7
Vessel	483	467	16
Shell	396	387	9

Table 3-13. Air Mass Flow for 800 kPa and 5 kW.

Air Mass Flow Rate [kg/s]	
Predicted	Measured
0.0595	0.0626

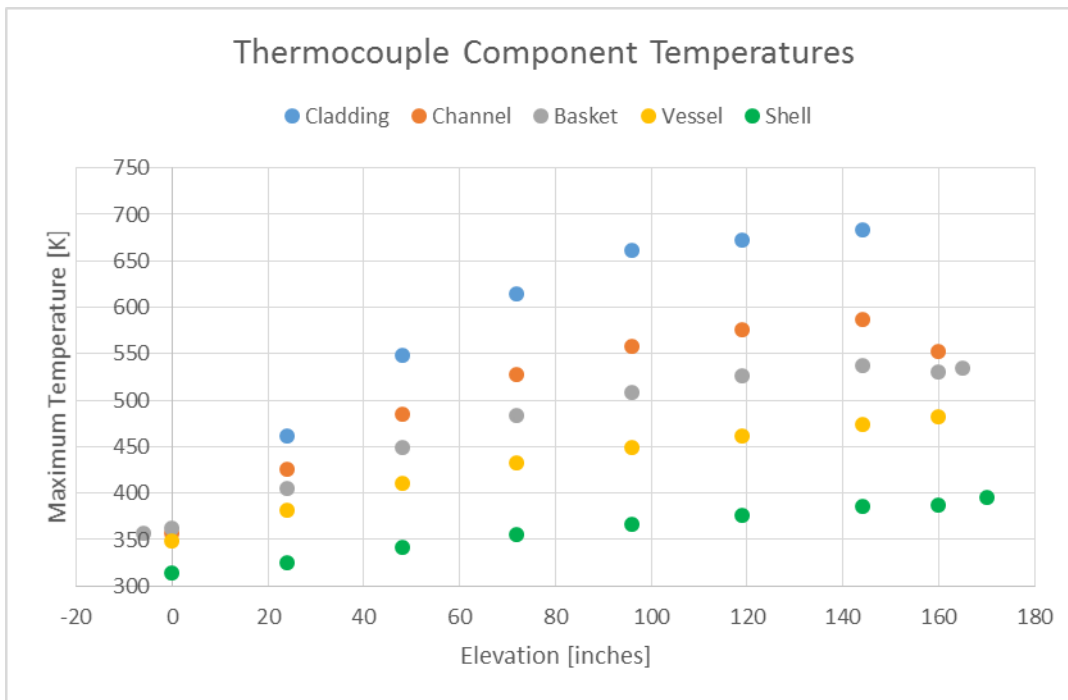


Figure 3-24. Thermocouple component temperatures for 800 kPa and 5 kW.

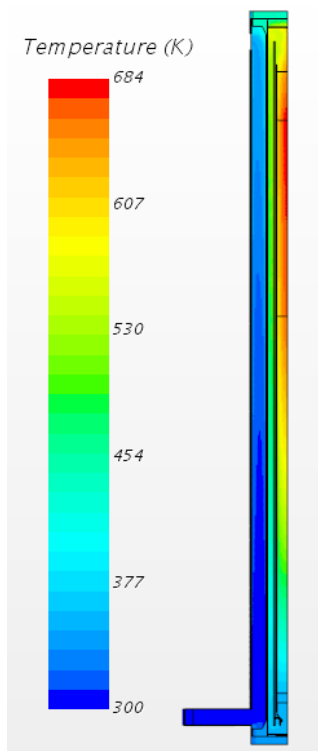


Figure 3-25. Axial temperature contour plot through assembly midsection for 800 kPa and 5 kW.

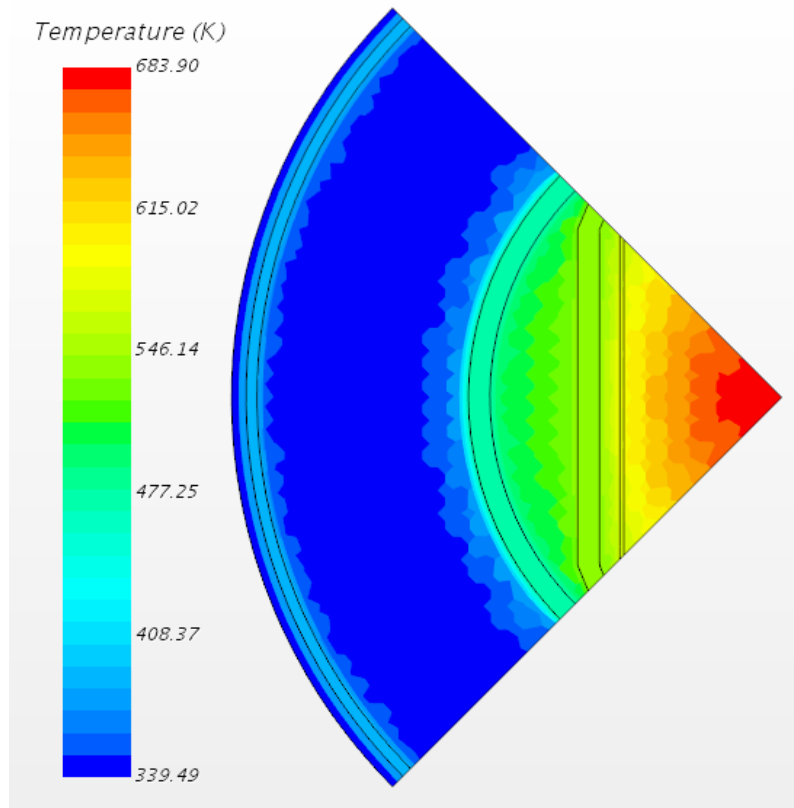


Figure 3-26. Radial temperature contour plot at the PCT elevation for 800 kPa and 5 kW.

### 3.5 Comparison with Detailed CFD

Figure 3-27 through Figure 3-30 plots the component temperature profiles for both the porous media model and the detailed model for each of the four corner cases. The resulting total air mass flow downstream of the inlets for both cases is compared against the measured data in Figure 3-31.

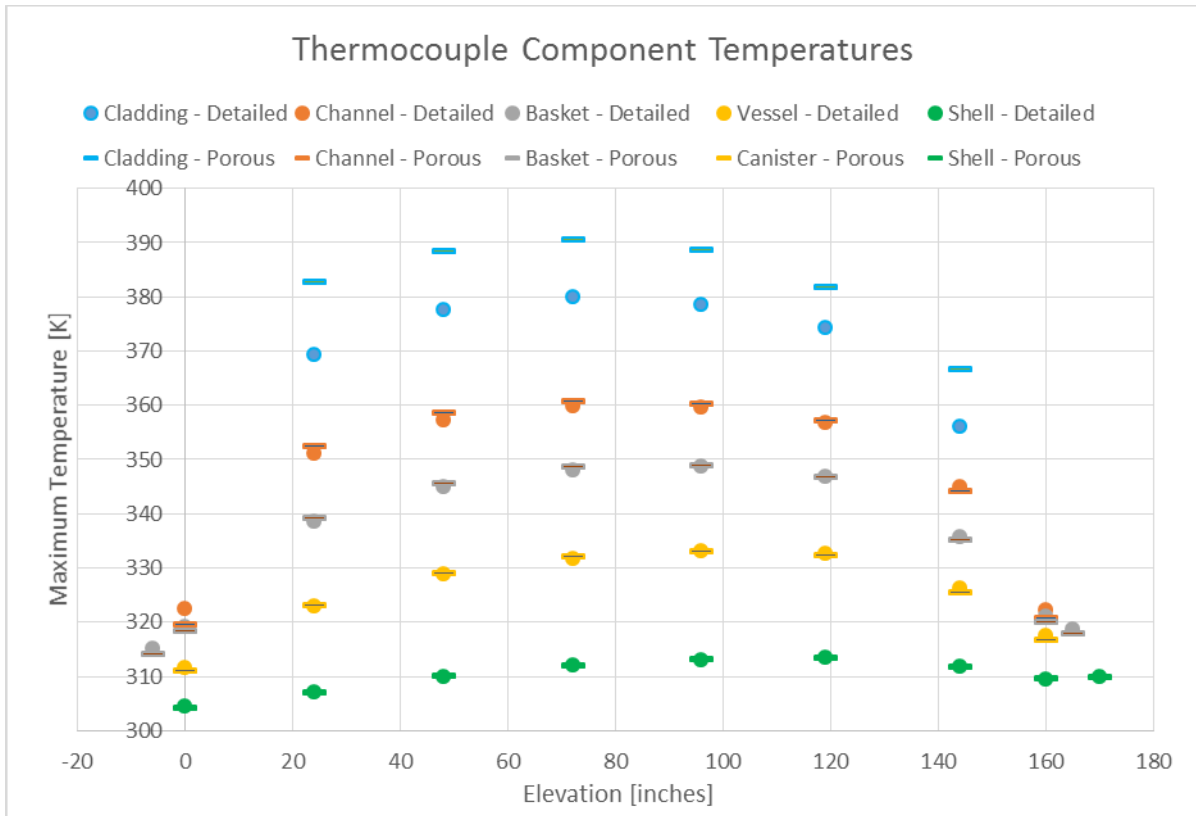


Figure 3-27. Component TC temperature profiles for 100 kPa @ 0.5 kW.

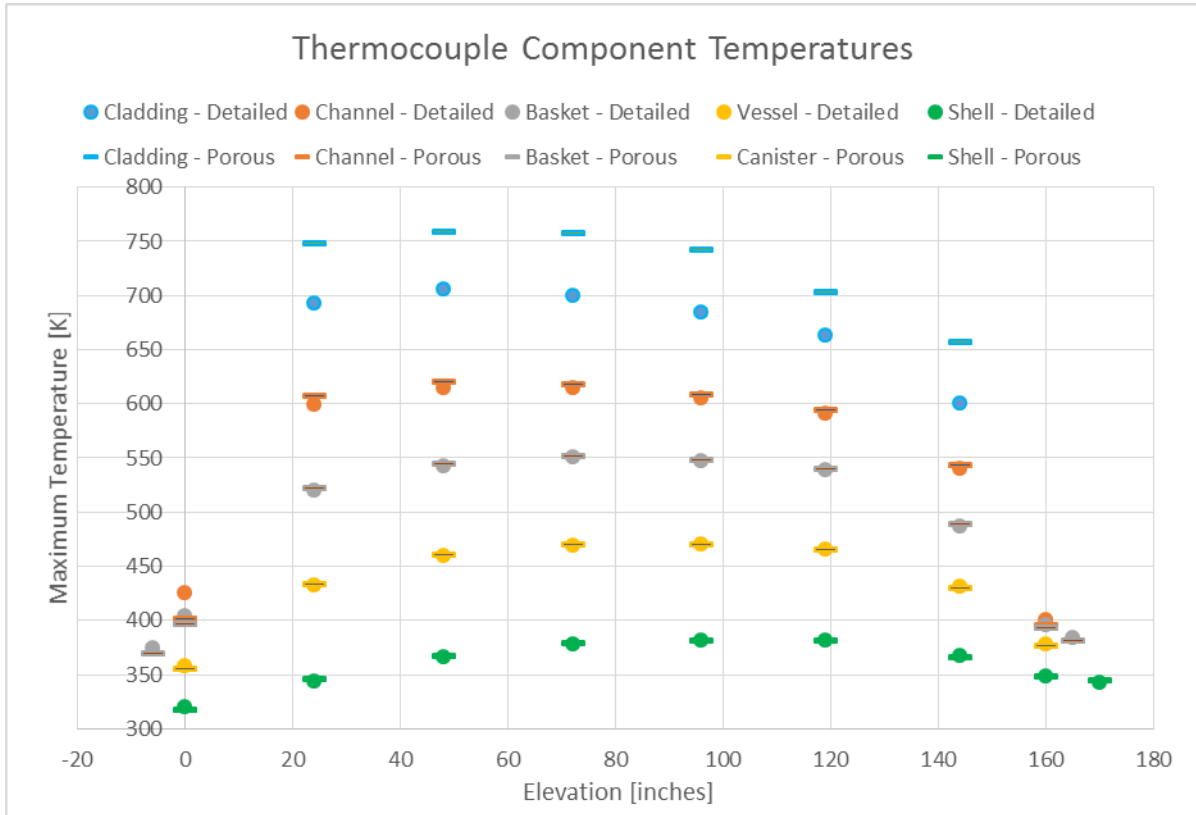


Figure 3-28. Component TC temperature profiles for 100 kPa @ 5 kW.

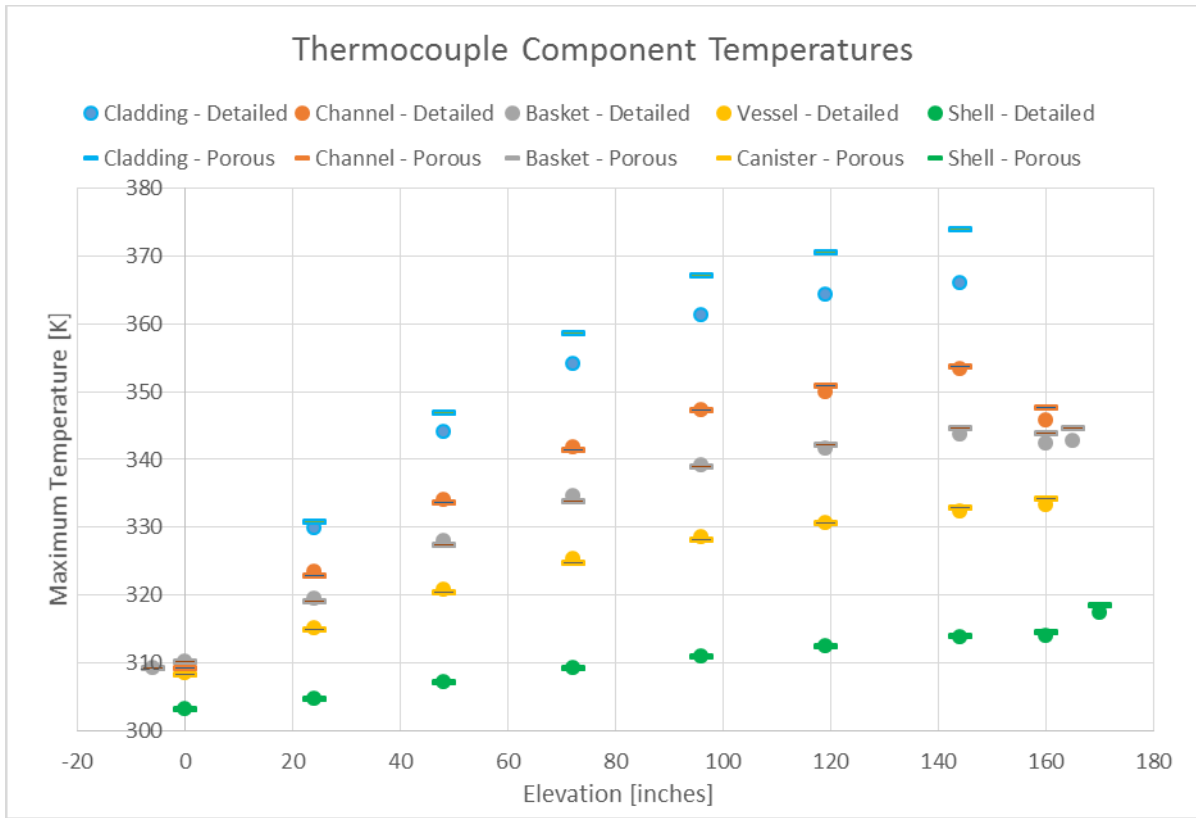


Figure 3-29. Component TC temperature profiles for 800 kPa @ 0.5 kW.

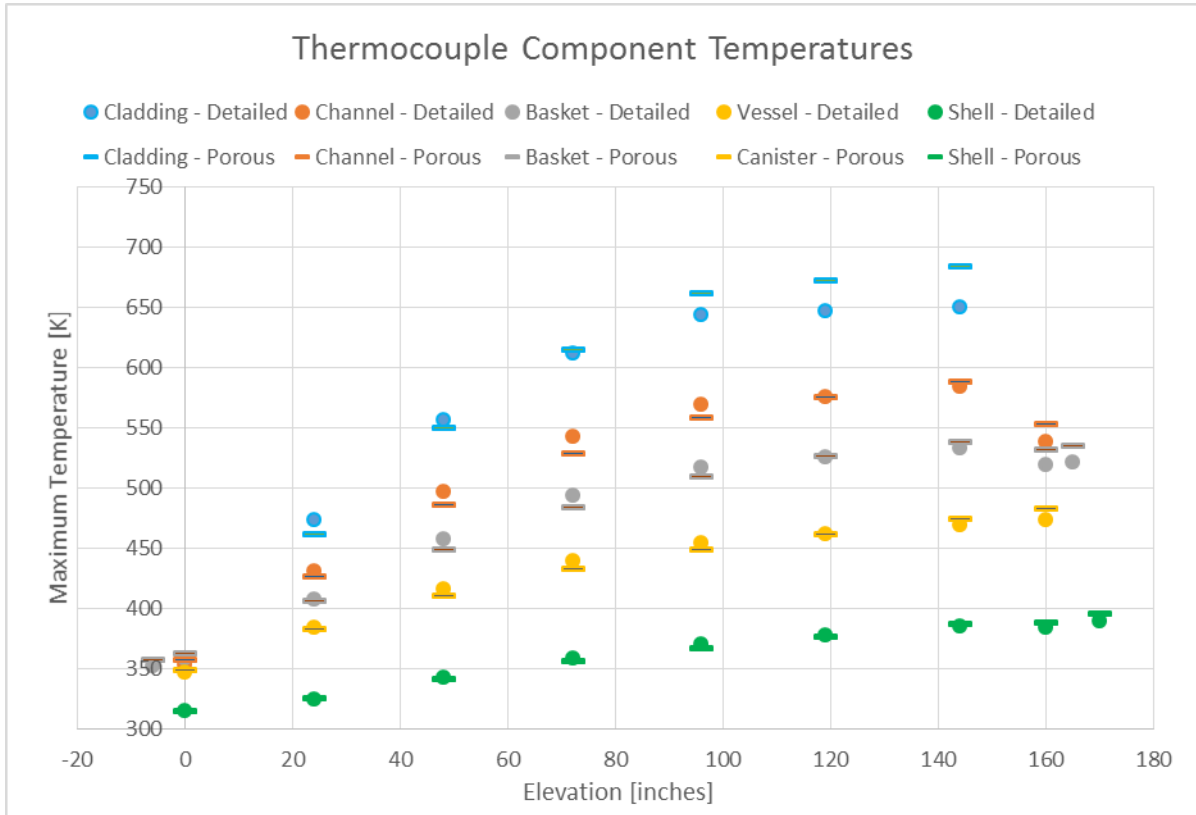


Figure 3-30. Component TC temperature profiles for 800 kPa @ 5 kW.

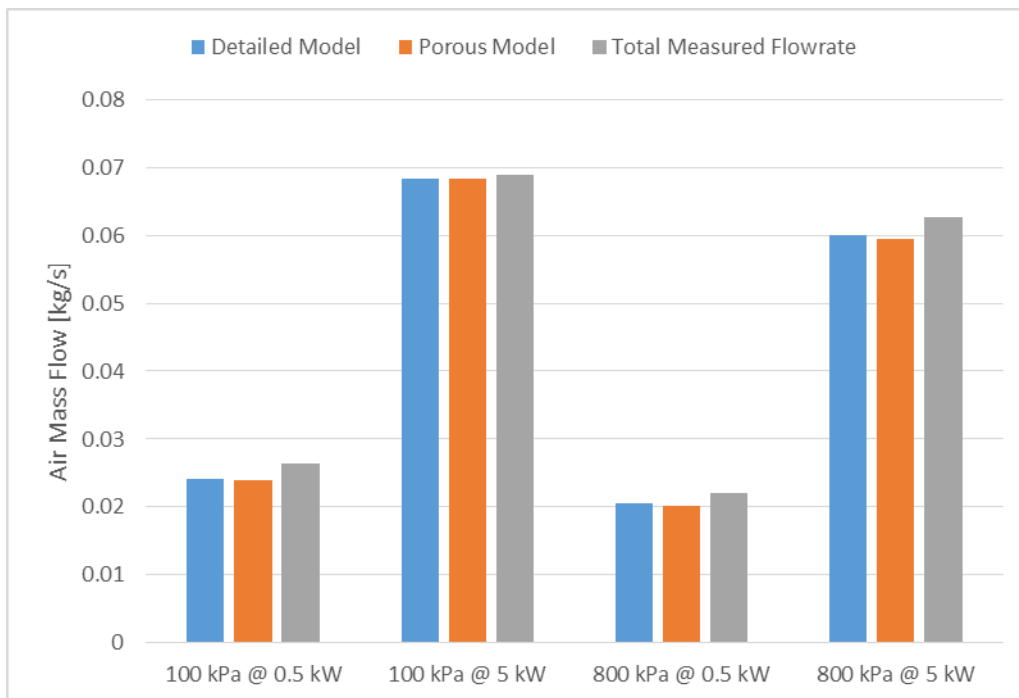


Figure 3-31. Air mass flowrate comparison.

The temperature profile plots show that overall the non-fuel component temperature profiles are similar between the porous and detailed model but the overall PCT profile is higher for the porous media model. This suggests that the  $k_{\text{eff}}$  fuel assembly provides conservative PCTs. The flowrate comparison plot shows good agreement between the detailed model, porous model, and measured data.

## 4. DETAILED MODELING WITH COBRA-SFS

This section describes the detailed modeling performed with COBRA-SFS (Michener et al. 2017). COBRA-SFS is a purpose-built thermal analysis code that has been used extensively in the modeling of spent fuel storage and transportation systems. The geometry, solid and fluid properties, and boundary conditions used in this model are described in detail below.

Overall, COBRA-SFS is still applicable to the BWR DCS, however there are several test characteristics that differ from full size casks and the previous validation tests that may challenge the code. One key aspect is that the power density in the DCS is much higher for a given measured temperature than a typical spent fuel cask. In the 5 kW case there amounts to  $\approx 70$  W/rod compared  $\approx 7$  W/rod in even very hot PWR assemblies. Additionally, the power generation profiles differ from typical spent fuel assemblies. Previous COBRA-SFS validation relied on actual fuel assemblies with typical decay heat generation profiles as opposed to the flat profile of the DCS.

### 4.1 Geometry Modeling

COBRA-SFS has a structure and solution method that takes advantage of the features of a spent fuel storage system to provide high levels of detail in the fuel region and other important features and a coarse representation of the outer regions of the cask. The code uses what is often termed a 2.5-dimensional representation of the main region of the cask. This involves dividing the cask structures into several axial levels that are represented two dimensionally. In a typical system, a sufficiently detailed model will result in approximately 1000 user defined solid nodes. Adding additional refinement has not generally been shown to be useful and becomes impractical due to the large amount of connection definitions needed.

In the case of the DCS, the small size would make it possible to refine with an extreme amount of detail and stay within practical limits for the user and the code. However, for the purposes of this modeling exercise the simulator model was represented with a similar resolution of what might be used for a full cask, resulting in only 40 solid nodes. The node map for the simulator is shown in Figure 4-1. With this approach, some conclusions can be drawn that are applicable to modeling full-scale systems. Typical run time on a PC was 1-2 minutes for this model, compared to 1-2 hours for a full-size cask. This is significantly shorter than the CFD models using much larger computing resources.

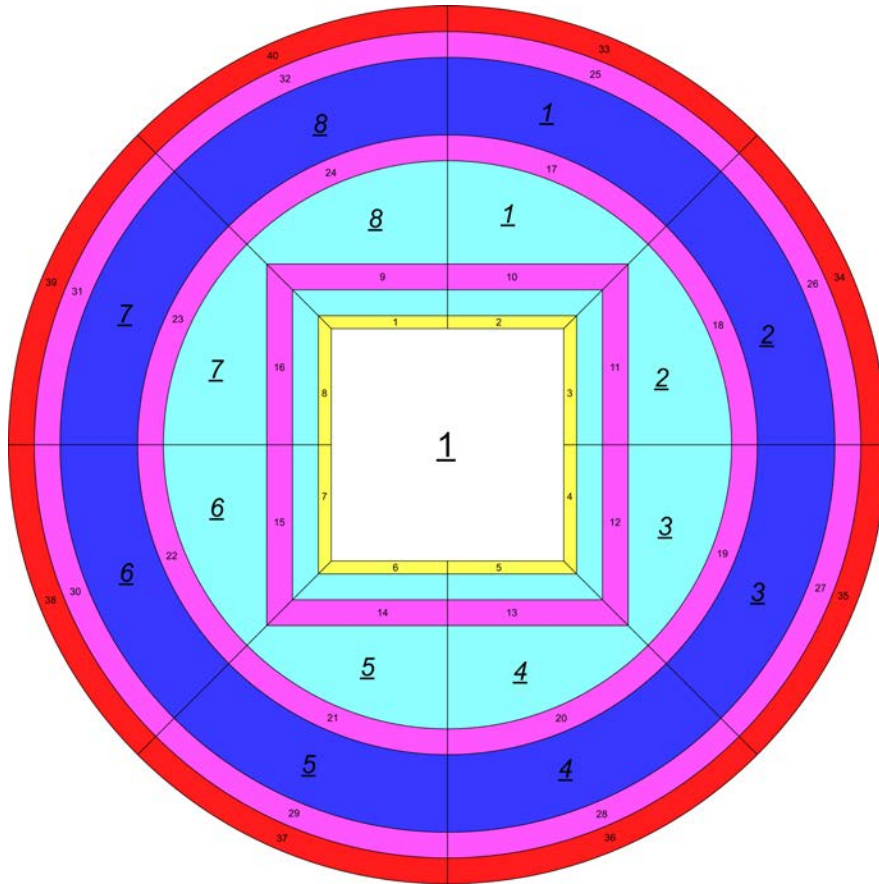
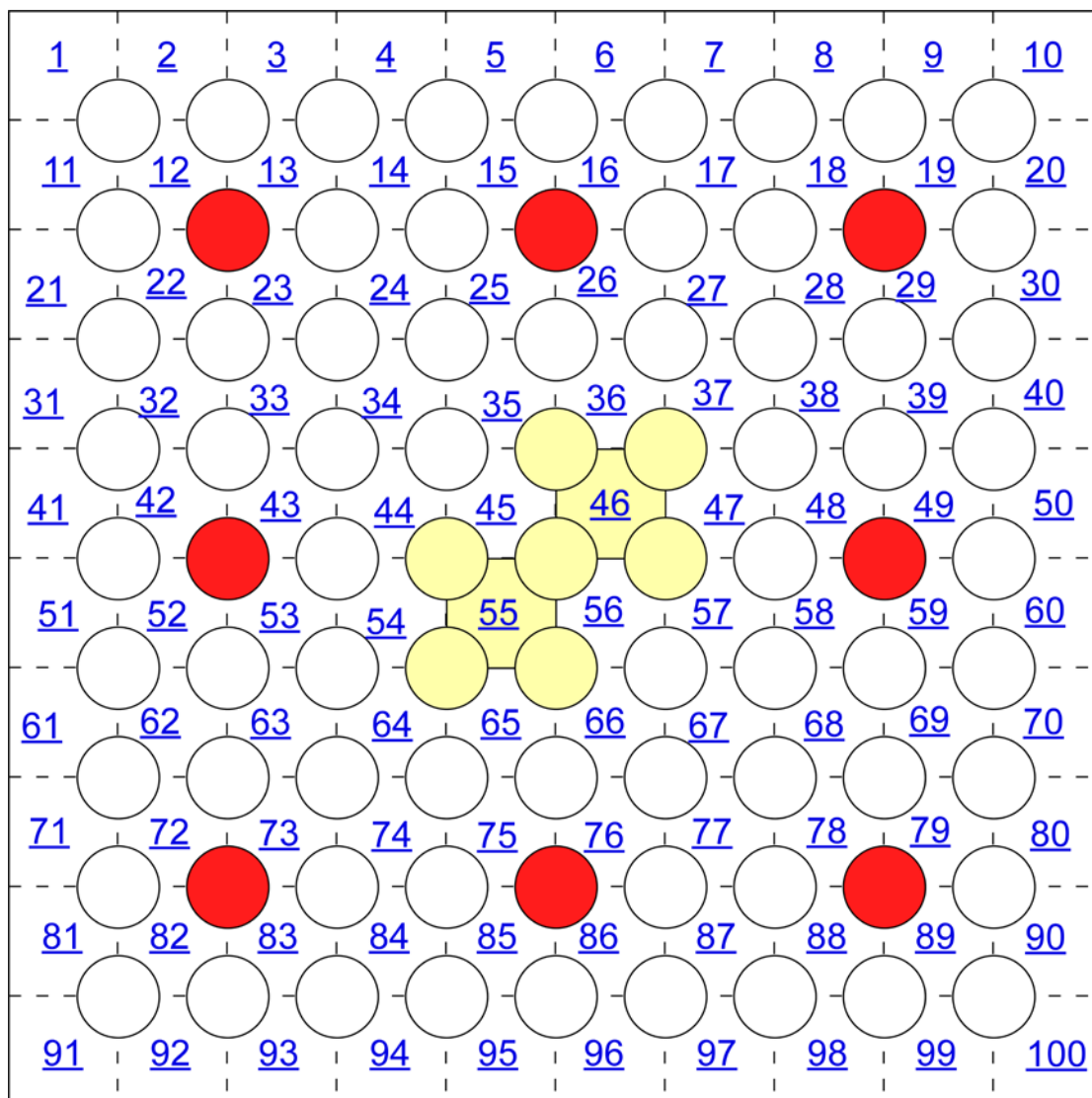


Figure 4-1. Cross-section of the COBRA-SFS model representation of the DCS. (Not to scale)



**Figure 4-2. Rod and subchannel array diagram for COBRA-SFS model of the 9x9 BWR fuel assembly. (Not to scale) (Yellow represents water rods. Red represents part-length rods) (Channels Numbered, Pin Numbers not Shown)**

#### 4.1.1 Treatment of Part-Length Rods and Water Rods

Figure 4-2 shows a representation of the 9x9 BWR fuel assembly used in the DCS. The highlighted rods and subchannels are the areas that the water rods occupy. For the COBRA-SFS model, these are modeled by blocking the channels where the water rods would be and turning off heat generation in the affected rods. This approach sufficiently represents both the true hydraulic resistance of the assembly and the heat generation distribution. There are also eight part-length rods shown in red in Figure 4-2. Hydraulically these rods are represented as full-length rods; this is considered appropriate for typical velocities in a spent fuel system and is assumed to have minimal effects on the overall flow characteristics. The total heat generation in these rods is modeled by reducing their relative power according to their length. This may result in an artificially flat axial power profile for the assembly. Unfortunately, a code change would be needed to allow varying the axial power on a rod by rod basis.

### 4.1.2 Treatment of Fuel Channel

BWR assemblies are typically placed in dry storage with the fuel channel intact. This is also the case with the DCS assembly. For COBRA-SFS modeling this presents two options for modeling the fluid region in between the fuel channel and basket. The standard practice would be to model the region as static helium along with a radiation connection. This approach neglects convection in this region and results in a conservative simplification for licensing analysis.

Alternatively, the model can be set up to solve for the fluid flow and resulting convection heat transfer along with the fluid conduction and surface to surface radiation. In a full-scale model this approach is usually considered to be too time intensive and not necessary for accuracy. In the case of the DCS model both approaches were tested, and results are presented for comparison.

## 4.2 Solid and Fluid Properties

Solid material properties were taken directly from the materials and dimensions handbook provided by Sandia. The fluid properties were taken from a National Institutes of Standard and Technology (NIST) reference as isobaric helium properties and air properties ([NIST 2019](#)). In COBRA-SFS a reference pressure is determined either by the specification, as in this case, or by an iterative process to match a density specification. Then temperature dependent fluid properties are entered at this reference pressure.

### 4.2.1 Treatment of Variable Emissivity

The fuel channel has a wide range of axial variation in emissivity with a minimum of 0.172 and a maximum of 0.655. This variation is atypical of BWR channels that have been in operation and are being placed in dry storage. In that case we would expect the profile to be much flatter and the magnitude to be close to the fuel's profile. This parameter becomes important at high temperatures because there is a strong radiation heat transfer path between the rods and the fuel channel. For best estimate modeling the average emissivity of 0.405 was used in the COBRA-SFS model. COBRA-SFS does not have a ready ability to vary the emissivity axially for this parameter, meaning there is no way to fully capture the effects of this simplification. A code change could be made to add this feature, although it is not typically a concern in spent fuel modeling. Sensitivity studies are presented below to characterize the effect of emissivity variation on the model.

## 4.3 Boundary Conditions

Boundary conditions for the BWR DCS include heat generation, side and top boundaries, and the air inlet and outlet.

### 4.3.1 Heat Generation

Heat generation of each rod was modeled individually and used a flat profile along the designated active length. Although not typical of spent fuel the overall behavior of the model is not greatly affected. In typical spent fuel the power generation across the center of the rod is relatively flat so the primary difference will be seen at the top and bottom of the rods.

### 4.3.2 Side and Top Boundaries

The side and top boundaries of the DCS were modeled using standard free convection correlations found in (Guyer and Brownell 1999). In this model, there is no external heating modeled due to solar insolation. This is appropriate because the test apparatus was placed inside a building.

### 4.3.3 Air Inlet and Outlet

COBRA-SFS uses a pressure drop boundary condition calculated from the fluid pressure drop between the top and bottom of the model. In this case the boundary temperature was changed as specified in the

(Durbin and Lindgren 2017) for each case. Specific values are shown Table 4-1. Standard loss coefficients are also applied to model the inlet and outlet air pathways.

**Table 4-1. Ambient temperatures used as boundary conditions in COBRA-SFS model.**

Boundary Temperature °F		
Internal Pressure	0.5 kW	5 kW
100 kPa	76.7	82.1
800 kPa	76.7	80.3

## 4.4 Results

Relevant COBRA-SFS results for the DCS compared to measured values are presented below. Table 4-2 shows the PCT for each case measured in Kelvin. There is good agreement for each case except the 800 kPa pressure and 5 kW heat load. Due to limited availability of measured axial temperature profiles it is difficult to analyze the nature of the difference; however, some conclusions are drawn in Section 5 by comparing against the STAR-CCM+ results.

**Table 4-2. Comparison of peak clad temperature measurements with results from COBRA-SFS.**

Peak Clad Temperature (K)						
Internal Pressure	0.5 kW			5 kW		
	<i>Predicted</i>	<i>Measured</i>	<i>Difference</i>	<i>Predicted</i>	<i>Measured</i>	<i>Difference</i>
100 kPa	384.2	376	8.2	713.8	716	-2.2
800 kPa	365.9	359	6.9	696.4	659	37.4

Figure 4-3 shows the predicted axial temperature profile of the hottest rod from each case. It is important to note that the 0 elevation of the model starts at the bottom of the basket and extends to the top of the basket. The active region is between 10.4” and 154.7”. From these plots the effect of increased helium pressurization on the temperature profile is very clear. Because the heater rods are modeled with a flat heat generation profile and the part-length rods are modeled as full length, the 100 kPa cases both show an extremely flat temperature profile across the active length. For the low-pressure cases the peak temperature is slightly above the center of the active length, but this is not particularly enlightening because the peak is not particularly high compared to anywhere else on the active length. For the high-pressure case the peak location is at the very top of the active length, which is considerably more interesting and shows an abnormally strong influence of convection heat transfer on the model compared to typical spent fuel systems.

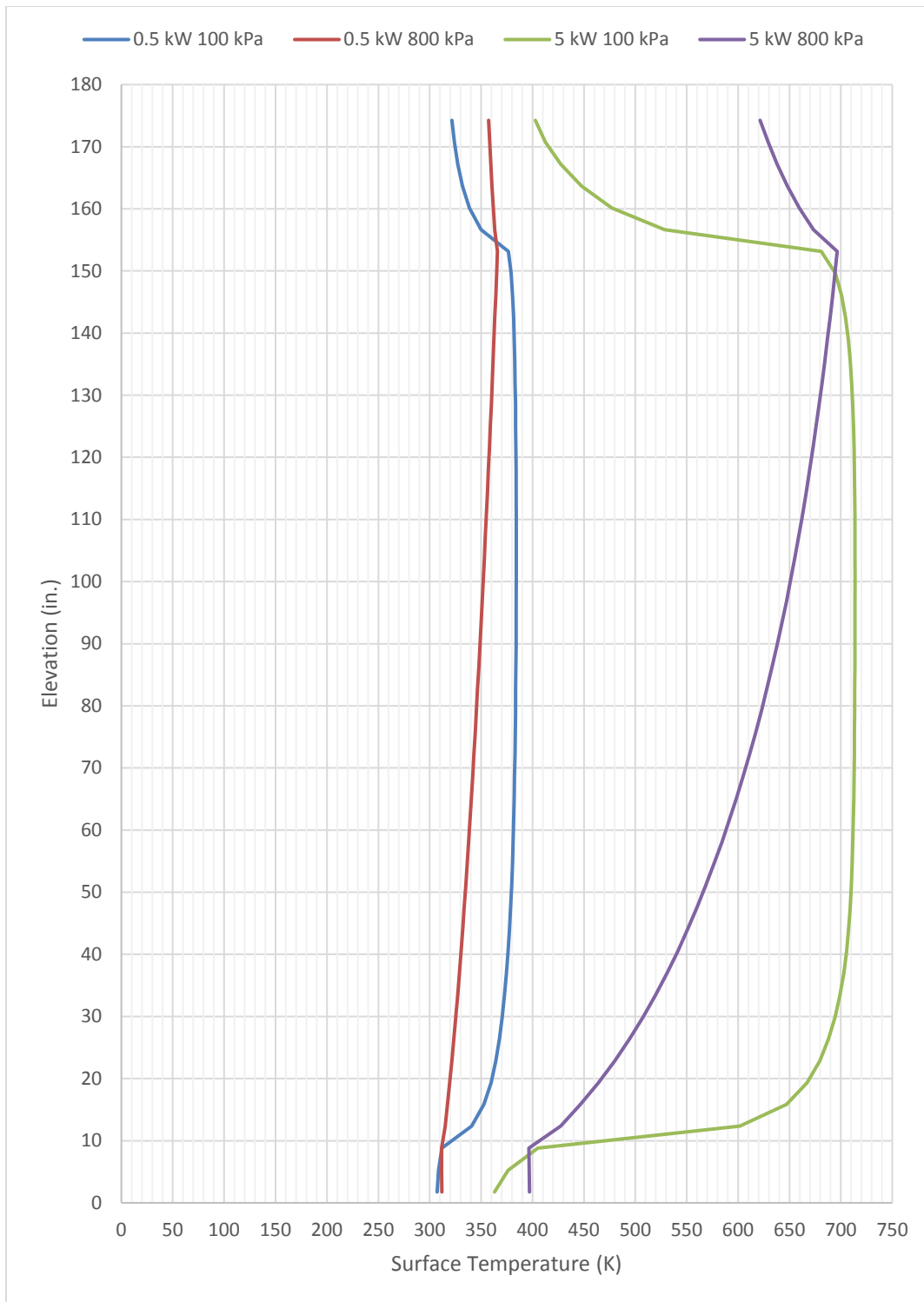


**Figure 4-3. Temperature plot of peak rod for each case,  
Note: the active length extends from 10.9" to 154.7".**

Total Air mass flow rate and helium flow rates are presented in Table 4-3 and Table 4-4. The helium flow rate was not measured during the experiment so there is no measured data to compare against, but conclusions can be drawn about the effects of helium pressurization.

**Table 4-3. Comparison of experimental averages and COBRA-SFS predictions for air mass flow.**

Total Air Mass Flow (kg/s)		
Case	COBRA-SFS	Experiment Average
0.5 kW 100 kPa	4.08E-02	2.64E-02
0.5 kW 800 kPa	3.96E-02	2.21E-02
5 kW 100 kPa	5.92E-02	6.89E-02
5 kW 800 kPa	5.62E-02	6.26E-02

For the low-pressure cases the COBRA-SFS model is over-predicting the airflow rate and for the higher pressure cases the model is under-predicting however because of the overall low flowrate for this type of system, these differences have a minor impact on PCTs.

**Table 4-4. Helium mass flow through COBRA-SFS model cross-sections.**

Helium Flow (kg/s)			
Case	Assembly	Channel-basket Gap	Downcomer
0.5 kW 100 kPa	4.56E-05	1.91E-04	-2.36E-04
0.5 kW 800 kPa	1.25E-03	3.68E-04	-1.62E-03
5 kW 100 kPa	3.33E-05	2.10E-04	-2.44E-04
5 kW 800 kPa	1.52E-03	9.29E-04	-2.45E-03

The helium flow rate in each case follows the trends that might be expected. By the higher average density that is present in the 800 kPa case, whatever helium velocity that is achieved will naturally correlate to a much higher mass flow rate. Table 4-4 shows the relative importance of helium flow in the channel-basket gap and the assembly region. There is roughly an order of magnitude difference between each pressure case. Because there are no measurements of helium flow rate, the best comparison will be with the STAR-CCM+ model in Section 5. The 100 kPa cases are the only ones with more helium flow in the gap. However, similar to the airflow, because of the extremely low mass flow rate, drawing broad conclusions from the low-pressure case is difficult.

## 4.5 COBRA-SFS Sensitivity Studies

This section describes the COBRA-SFS channel and emissivity sensitivity studies.

### 4.5.1 Sensitivity to Channel Model

As mentioned in Section 4.1.2, the gap between the fuel channel and the basket was modeled with two different methods. The comparison is shown against PCT and helium mass flow rate through the assembly. Helium mass flow rate is shown in Figure 4-4.

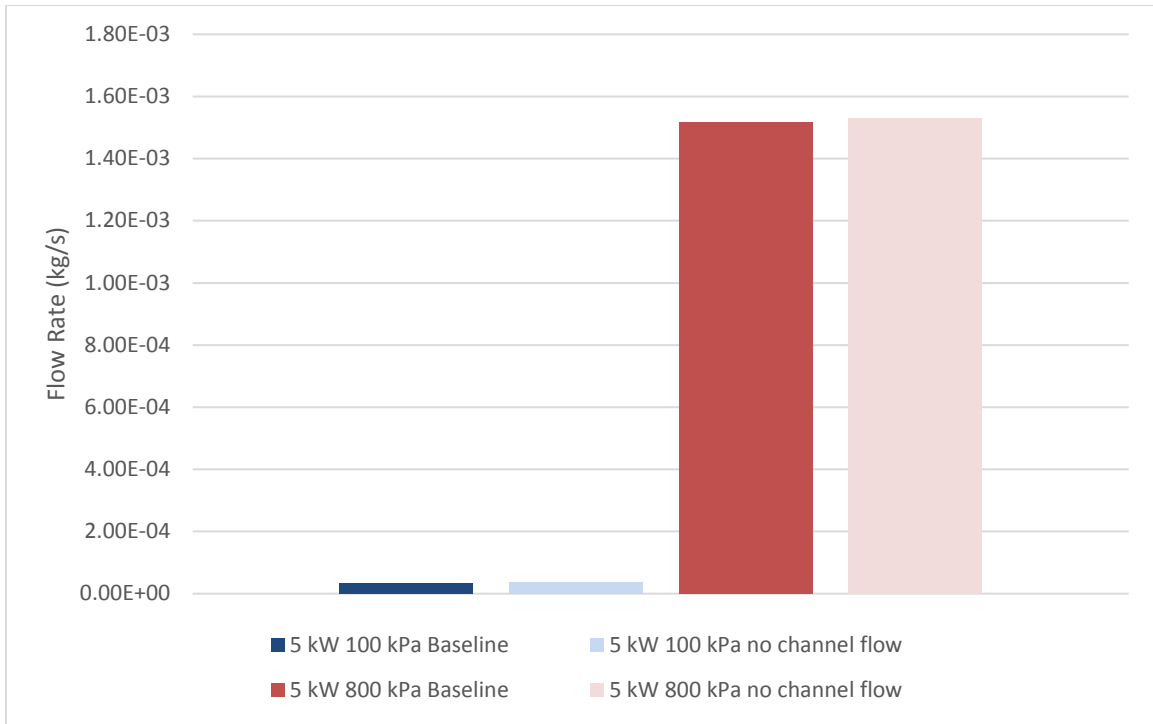


**Figure 4-4. Assembly flow (channel flow vs. no channel flow).**

The difference between helium mass flow rates in both cases is minor. This is expected because even though the available area for up-flow is significantly increased there is no increase in the amount of surface area that the fuel can transfer heat through. This limits the ability of buoyant forces to accelerate the flow.

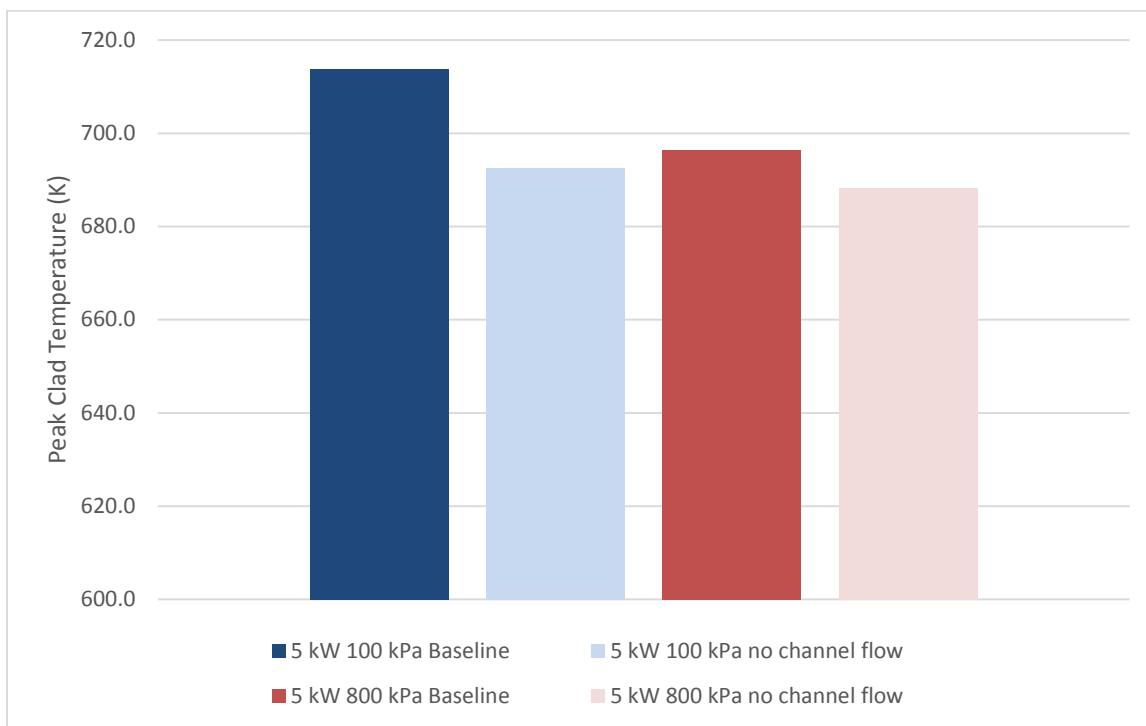


**Figure 4-5. Peak clad temperature comparison (channel flow vs. no channel flow).**

The PCT shown in Figure 4-5 demonstrates a wide difference between the two modeling approaches, especially in the low-pressure case, indicating this difference is not driven by convection heat transfer considerations. The best explanation for this is the difference between thermal radiation modeling of the gap between the channel and the basket. For a solid-solid connection with gap resistance and radiation COBRA-SFS uses a simple flat plate radiation model. The accuracy of this simplification breaks down as gap sizes increase. In the low-pressure case radiation heat transfer is more dominant and therefore the inaccuracy of the simplification is more apparent. It is important to note that for COBRA-SFS modeling the channel-basket connection explicitly is more conservative than the simplified methodology.

For future BWR cask modeling the author’s recommendation would be to carefully consider the expected flow characteristics and expected gap size when choosing an approach. In a pressurized cask with small channel-basket gaps (ex. Holtec MPC-89, NAC TSC-87) simplifying the modeling will tend to have a small impact on PCT and may be appropriate. However, for a low pressure or horizontal system (ex. TN-68, NUHOMS® 61-BT) the simplification of the radiation model will likely produce unacceptably non-conservative results at high heat loads. In that type of case the channel-basket gap will be relatively large on one side due to the horizontal orientation and there is a negligible amount of convection heat transfer.

#### 4.5.2 Sensitivity to Channel Emissivity

Due to the inability of COBRA-SFS to model axially varying channel emissivity it is important to characterize the sensitivity for this parameter. A comparison of both a high and low emissivity to the baseline is shown in Figure 4-6.

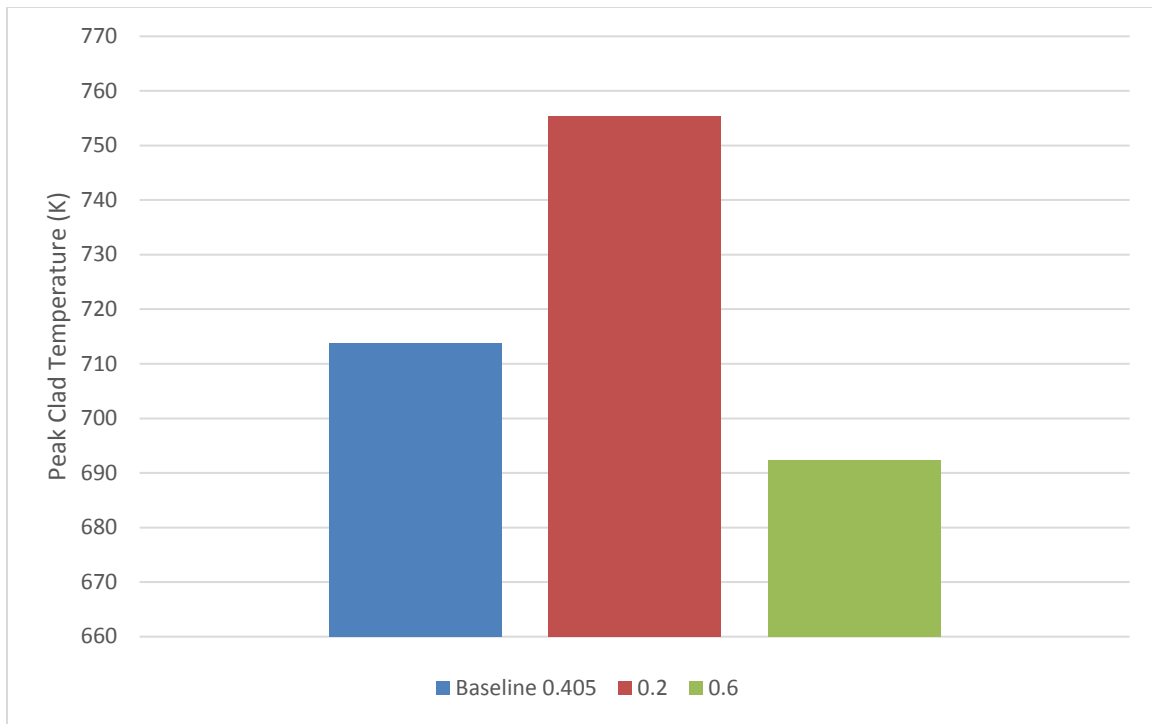


**Figure 4-6. Sensitivity to channel emissivity.**

The results show a large sensitivity to the channel emissivity at high power and low pressure. This is expected because at low pressure the only significant mechanisms for heat transfer from the rods are thermal radiation and fluid conduction. The decision to use the average emissivity is a best estimate methodology for predicting the overall temperature behavior of the system. Because heat transfer is primarily radial, if a specific axial temperature prediction is desired it may be appropriate to bias the modeled emissivity towards the measured emissivity at that axial level.

## 5. COMPARISON OF STAR-CCM+ AND COBRA-SFS RESULTS

Results comparing the STAR-CCM+ and COBRA-SFS models are presented in this section. Table 5-1 lists the PCT and the elevation of the PCT for measured data and each of the three models. Table 5-2 compares the helium mass flow rates at a center radial plane. Comparison plots for the cladding temperature and air mass flow rates are shown for all four corner cases in Figure 5-1 through Figure 5-8.

**Table 5-1. PCT comparison table.**

Model	100kPa @ 0.5kW		100kPa @ 5kW		800kPa @ 0.5kW		800kPa @ 5kW	
	PCT [K]	Elevation [in]	PCT [K]	Elevation [in]	PCT [K]	Elevation [in]	PCT [K]	Elevation [in]
Measured Data	376	72.0	716	48.0	359	144.0	659	144.0
STAR-CCM+ - Detailed	380	73.4	707	49.4	367	141.4	652	141.8
STAR-CCM+ - Porous	391	83.4	759	56.4	374	145.8	684	145.8
COBRA-SFS	384	105	714	99.75	366	152.25	696	152.25

\*Elevation origin starts at the top of the bottom tie plate.

**Table 5-2. Helium mass flow comparison table.**

Case	Helium Mass Flow [kg/s]								
	COBRA-SFS			STAR-CCM+ Detailed			STAR-CCM+ Porous		
	Fuel Assembly	Channel-Basket Gap	Downcomer	Fuel Assembly	Channel-Basket Gap	Downcomer	Fuel Assembly	Channel-Basket Gap	Downcomer
0.5 kW 100 kPa	4.56E-05	1.91E-04	-2.36E-04	5.63E-06	3.14E-06	-8.78E-06	4.11E-06	3.17E-06	-7.18E-06
0.5 kW 800 kPa	1.25E-03	3.68E-04	-1.62E-03	1.57E-04	9.55E-05	-2.51E-04	1.55E-04	1.02E-04	-2.58E-04
5 kW 100 kPa	3.33E-05	2.10E-04	-2.44E-04	8.73E-06	5.64E-06	-1.44E-05	8.31E-06	5.60E-06	-1.39E-05
5 kW 800 kPa	1.52E-03	9.29E-04	-2.45E-03	2.76E-04	1.79E-04	-4.48E-04	3.31E-04	1.74E-04	-5.04E-04

5.1.1 100 kPa, 0.5 kW

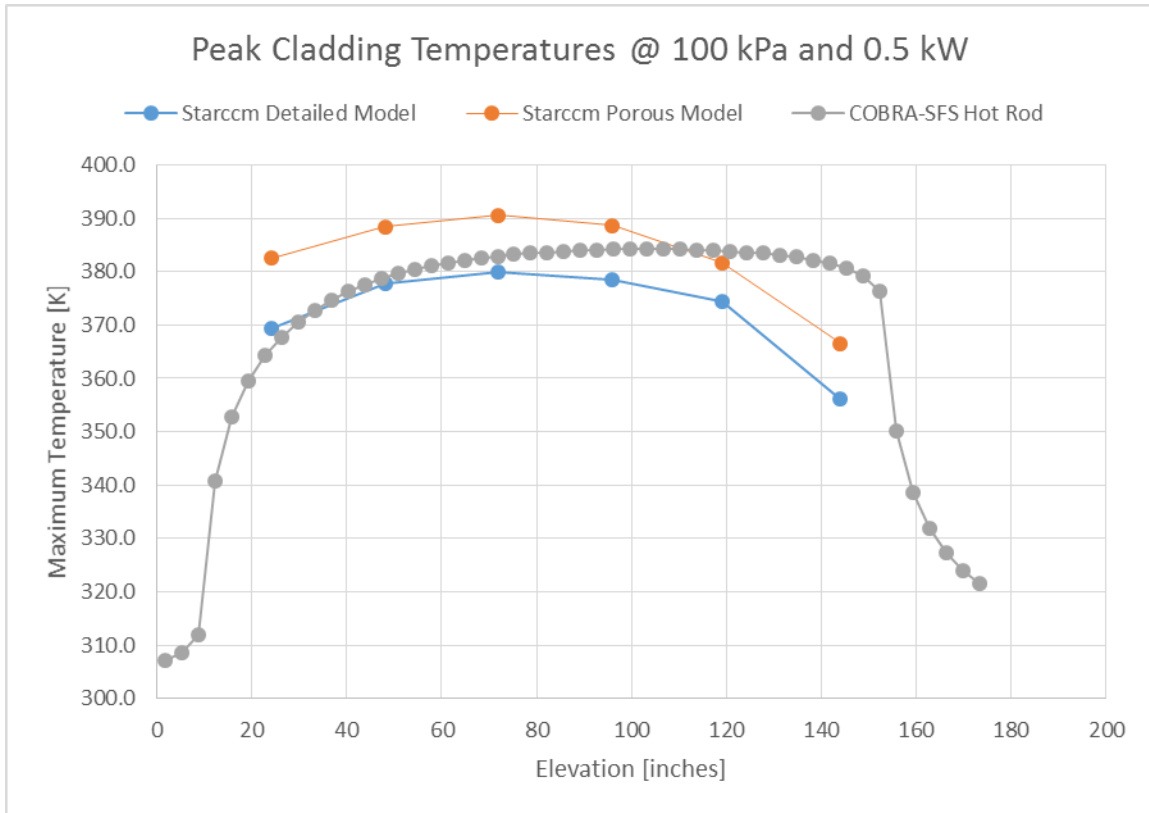
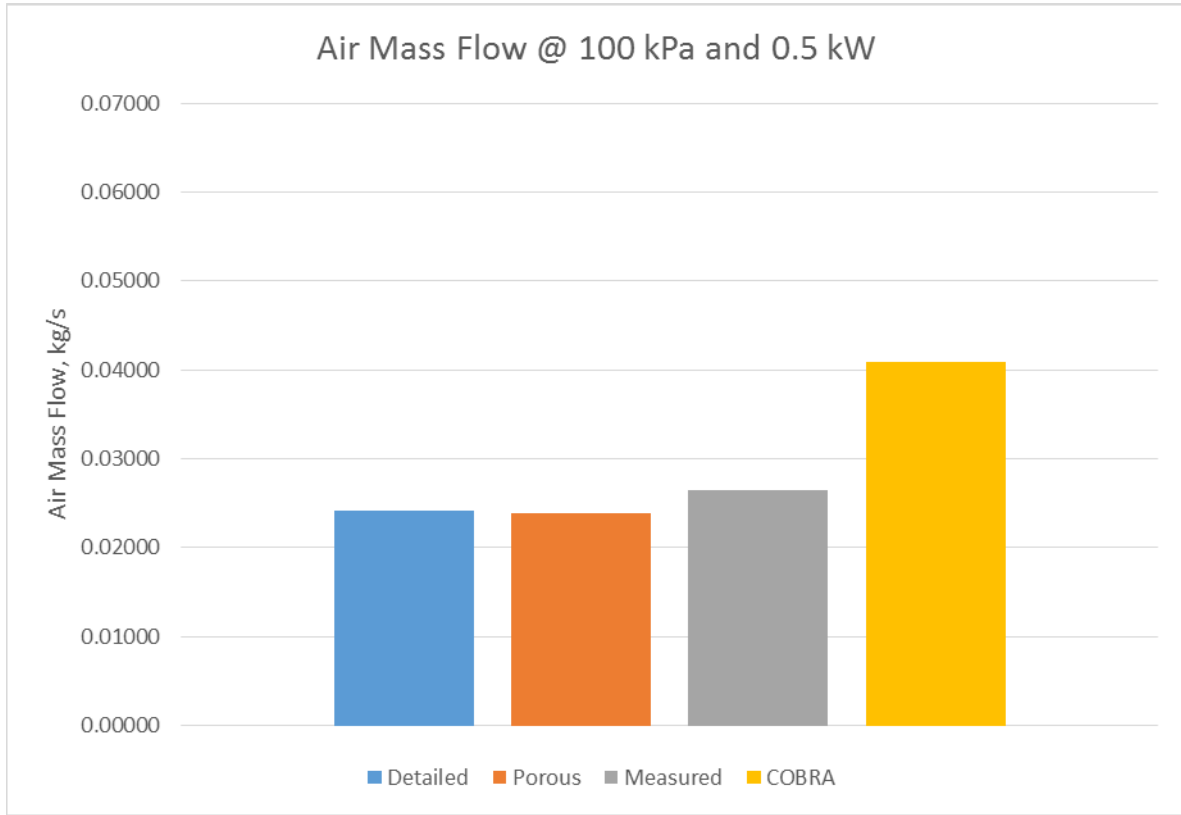


Figure 5-1. PCT comparison plot for 100 kPa and 0.5 kW.



**Figure 5-2. Air mass flow comparison plot for 100 kPa and 0.5 kW.**

## 5.1.2 100 kPa, 5 kW

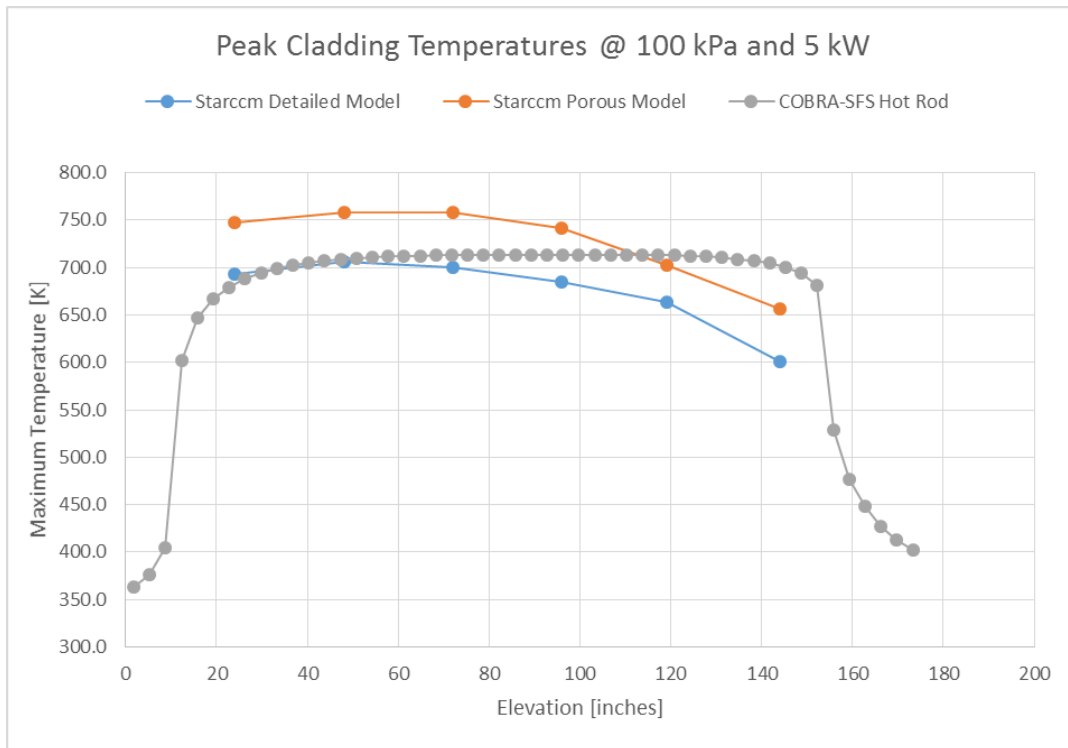


Figure 5-3. PCT comparison plot for 100 kPa and 5 kW.

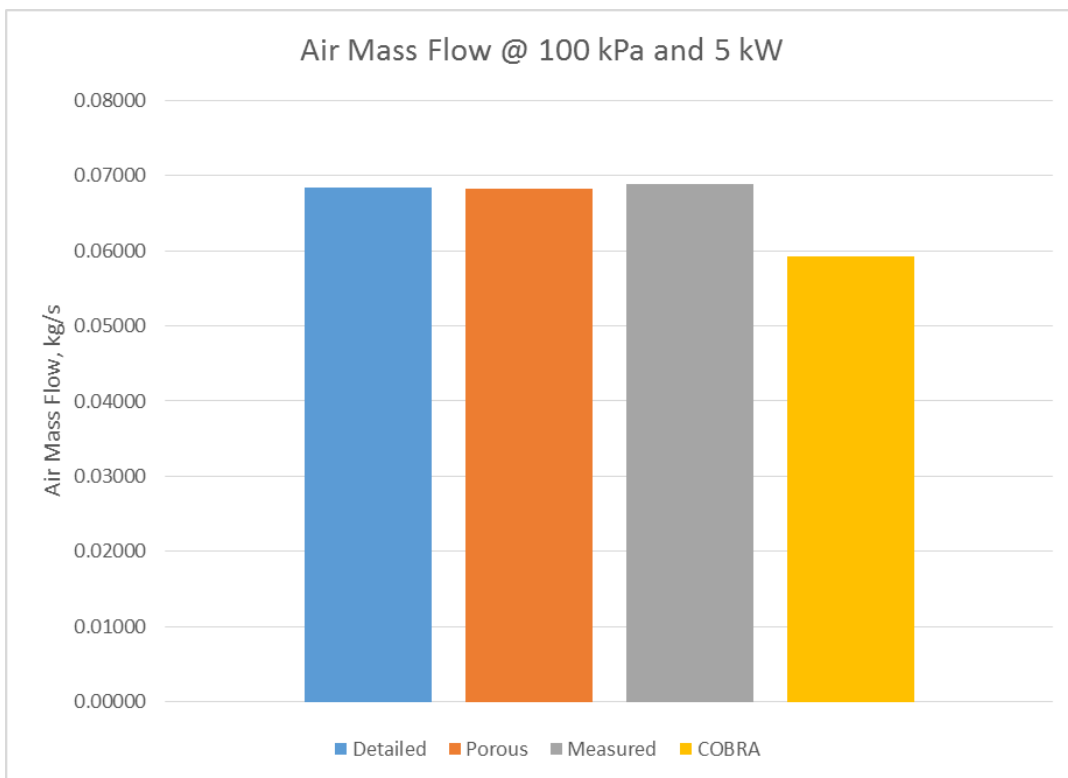


Figure 5-4. Air mass flow comparison plot for 100 kPa and 5 kW.

### 5.1.3 800 kPa, 0.5 kW

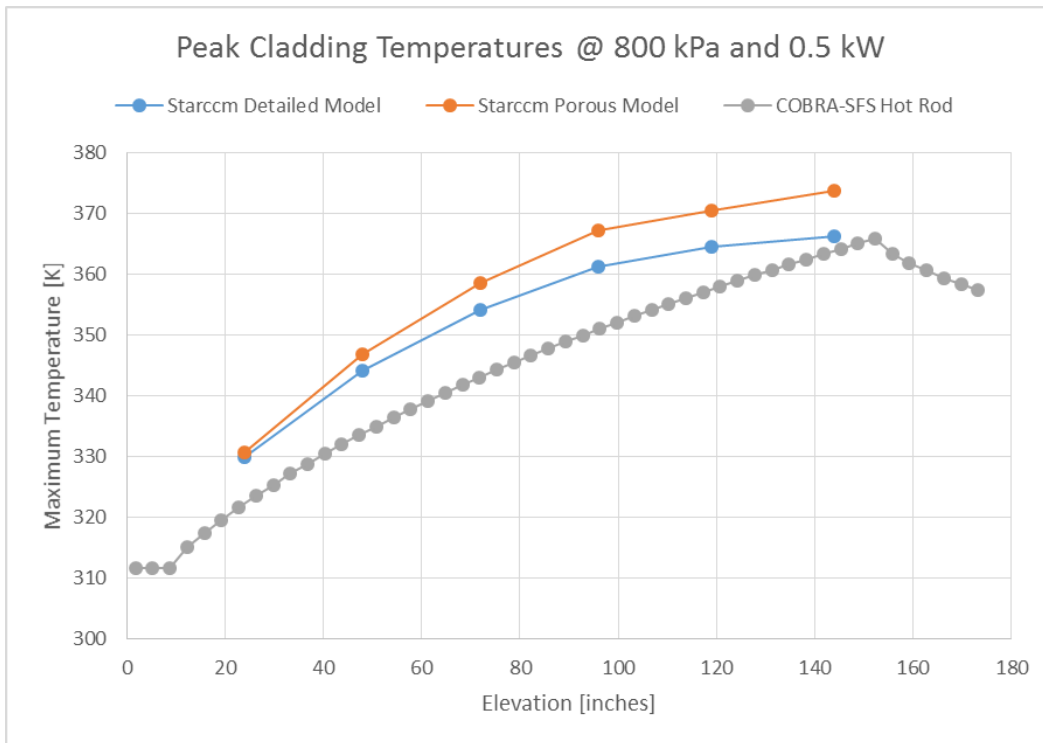


Figure 5-5. PCT comparison plot for 800 kPa and 0.5 kW.

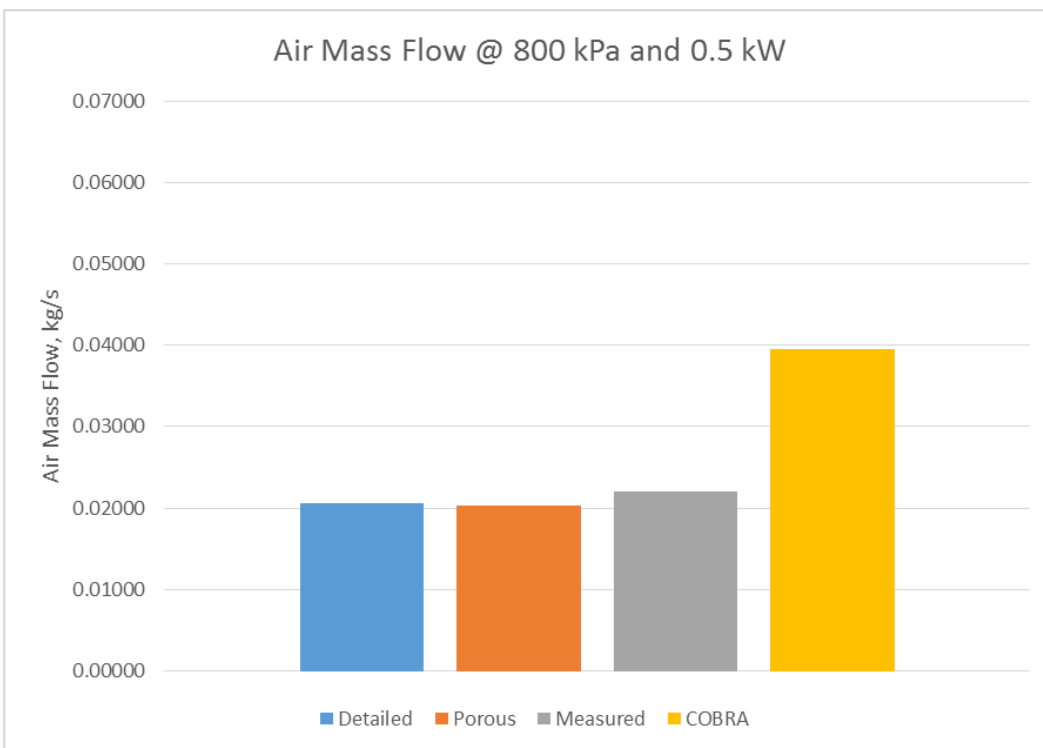


Figure 5-6. Air mass flow comparison plot for 800 kPa and 0.5 kW.

## 5.1.4 800 kPa, 5 kW

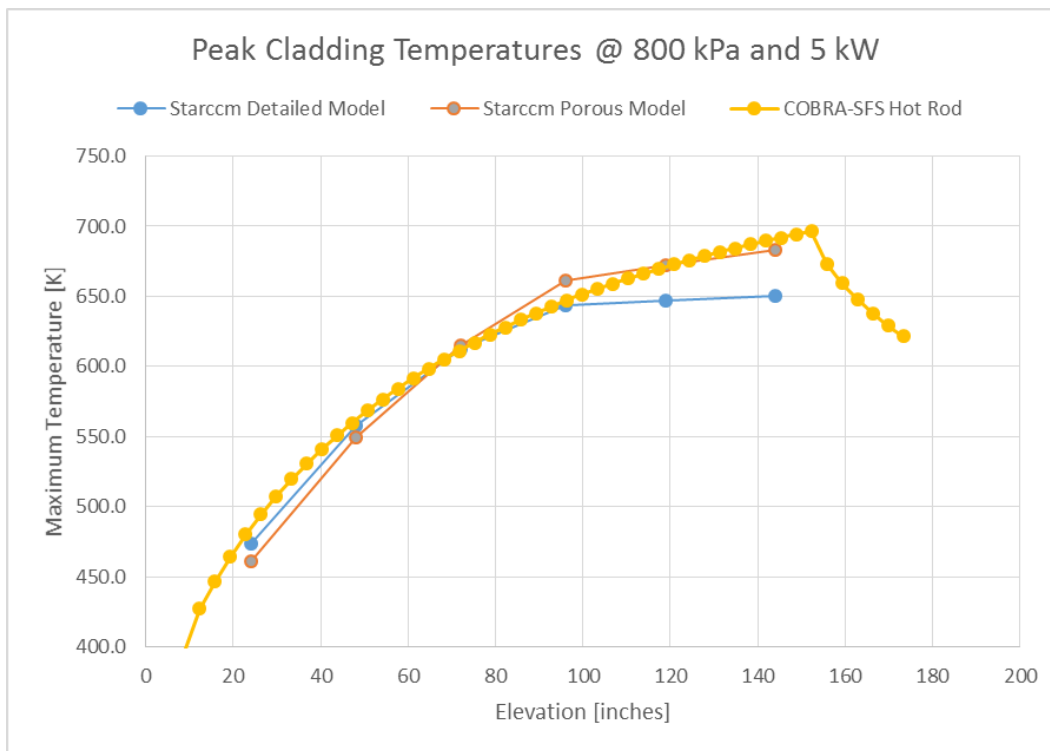


Figure 5-7. PCT comparison plot for 800 kPa and 5 kW.

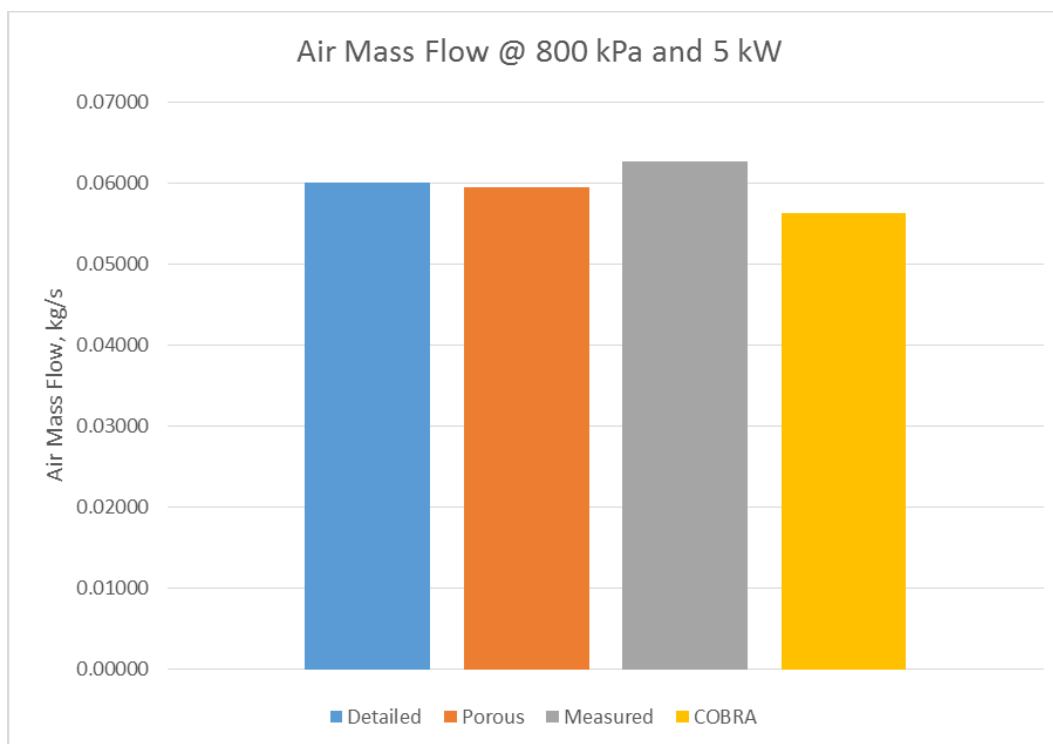


Figure 5-8. Air mass flow comparison Plot for 800 kPa and 5 kW.

## 6. CONCLUSIONS AND RECOMMENDATIONS

Overall the measured PCT is in good agreement between the three models, with the STAR-CCM+ detailed and COBRA-SFS models providing the best comparison with the measured data. The STAR-CCM+ porous model predicted higher PCT values than the measured data for all four pressure heat load combinations, indicating that  $k_{\text{eff}}$  fuel assembly approach provides conservative PCTs. Using a split  $k_{\text{eff}}$  approach for the BWR fuel assembly was also shown to produce the best PCT agreement with the measured data for the porous model. The split  $k_{\text{eff}}$  approach calculated two different  $k_{\text{eff}}$  correlations for the full and partial array sections.

The PCT is in good agreement between the detailed STAR-CCM+ and the COBRA-SFS models, except for the high pressure and high heat load case (800 kPa and 5 kW). The COBRA-SFS cladding temperature profile is flat in comparison with STAR-CCM+ models. This is most likely due to differences in how the partial length rods are handled in COBRA-SFS and that an average emissivity was applied axially over the channel box for the COBRA-SFS model. At the time of this report no profile data was available for the measured DCS data, only the PCT and the elevation that the PCT occurred at. Comparing the elevation at which the PCT occurred shows that the STAR-CCM+ model elevations occur at similar locations to the measured data, especially the detailed model. The COBRA-SFS model with the flatter profile varied significantly from the measured data for the low-pressure cases (100 kPa).

The COBRA-SFS model had a higher predicted air mass flow rate in comparison with the STAR-CCM+ models for the low heat load cases (0.5 kW) and predicted a slightly lower air mass flow rate for the high heat load cases (5 kW).

All three models were able to produce reasonable PCT estimates, with the porous media model with the  $k_{\text{eff}}$  fuel assembly providing the most conservative PCT estimates. The meshing study with STAR-CCM+ porous media model showed that even the coarsest mesh provided reasonable PCT temperatures. This indicates that a larger model with a full cask/fuel assembly (instead of the single fuel assembly represented in the DCS) could be constructed at a computationally efficient element size with the porous media model.

The authors recommend making code changes to COBRA-SFS to better suit BWR modeling. Historically the code was developed before BWR assemblies routinely included part-length rods and applied primarily to PWR assemblies because they are the most thermally limiting in safety analysis. To provide an easily applicable toolset for high fidelity BWR modeling the code should be changed to include better part-length rod and fuel channel modeling tools.

This page is intentionally left blank.

## 7. REFERENCES

- Dassault Systemes SolidWorks Corp. 2017. SolidWorks Premium 2017 x64 Edition (computer software). Waltham, Massachusetts: Dassault Systemes.
- Durbin, S.G. and E.R. Lindgren. 2017. *Thermal-Hydraulic Results for the Boiling Water Reactor Dry Cask Simulator*. SAND2017-10551: Sandia National Laboratories, Albuquerque, New Mexico.
- Guyer, E.C. and D.L. Brownell. 1999. Handbook of Applied Thermal Design. Castleton, New York: Hamilton Printing Co.
- Holman, J. 1997. Heat Transfer. New York: McGraw-Hill.
- Incropera FP, DP Dewitt, TL Bergman, and AS Lavine. 2007. *Fundamentals of Heat and Mass Transfer*. 6th ed. John Wiley & Sons, Hoboken, New Jersey.
- Lindgren, E.R. and S.G. Durbin. 2007. *Characterization of Thermal-Hydraulic and Ignition Phenomena in Prototypic, Full-Length Boiling Water Reactor Spent Fuel Pool Assemblies after a Complete Loss-of-Coolant Accident*. SAND2007-2270, Sandia National Laboratories, Albuquerque, New Mexico.
- Lindgren, E.R. and S.G. Durbin 2017. *Materials and Dimensional Reference Handbook for the Boiling Water Reactor Dry Cask Simulator*. SAND2017-13058: Sandia National Laboratories, Albuquerque, New Mexico.
- Michener, T.E. D.R. Rector, J.M. Cuta, and H.E. Adkins Jr. 2017. *COBRA-SFS: A Thermal Hydraulic Analysis Code for Spent Fuel Storage and Transportation Casks, Cycle 4a*. PNNL-24841: Pacific Northwest National Laboratory, Richland, Washington.
- National Institute of Standards and Technology. 2019. Chemistry Webbook. Accessed January 2019. <http://webbook.nist.gov/chemistry/fluid/>
- National Technical Information Service. 1960. *Handbook of Hydraulic Resistance – Coefficients of Local Resistance and of Friction*. U.S. Department of Commerce, National Technical Information Service.
- Roache, P.J. 2009. Fundamentals of Verification and Validation, Hermosa Publishing: Socorro, New Mexico.
- Siemens PLM Software. 2018. STAR-CCM+ 13.02 (computer software). Plano, Texas: Siemens PLM Software.
- TRW. 1996. *Spent Nuclear Fuel Effective Thermal Conductivity Report*. BBAA000000-01717-5705-00010, Rev. 00, TRW Environmental Safety Systems, Inc., for the U.S. Department of Energy, Yucca Mountain Site Characterization Project Office.
- White, F.M. 1974. Viscous Fluid Flow, Third Edition. New York: McGraw-Hill.